ABSTRACT

Title of dissertation: Particle Dispersal of Granular Materials in High-Speed Compressible Flow

Shuyue Lai, Doctor of Philosophy, 2019

Dissertation directed by: Professor Elaine Oran
Glenn L. Martin Institute Professor of Engineering
Department of Aerospace Engineering

This dissertation describes efforts to investigate particle dispersal of granular materials under high-speed flows using a recently proposed continuum model for dense granular materials [1, 2]. The model, based upon the kinetic theory of granular flows (KTGF), is known to perform well for high-speed, compressible flows over a wide range from dense to dilute particle volume fractions. The simulations solve the Euler equations of fluid dynamics and granular flow, and account for multiple particle types using a binning approach, where particles in each bin have their own uniform particle size and density. This model is then applied to two configurations (a) dust-lifting induced by shock waves, and (b) subsurface explosions in granular materials. These two examples are used to underpin a thorough discussion of particle motions under high-speed flow.

The first study discusses the phenomenon of dust lifting behind a moving shock wave in which the conditions are characteristic of what is found in a coal mine. Specifically, we are interested in the factors influencing the level of dust dispersion, and the particle segregation phenomenon between different types of particles within the dust

layer. First, we investigated the case of a shock wave passing over a single dust layer containing two uniformly mixed particle types. Effects of particle size and density were studied in terms of the governing forces acting on each particle type. The results indicate that larger particles are lifted higher than smaller particles, and lighter particles are lifted higher than heavier particles due to the differences in lift and drag forces. Then, simulations of a shock passing over stratified dust layers containing different types of particles were performed. We find that the larger particles placed in the lower layer can be lifted higher than the smaller particles placed in the upper layer when the two types of particles have large size differences. These results provide important information that can be used to determine how to prevent and mitigate a dust explosion in underground coal mines.

The second study discusses particle ejections from a subsurface explosion in the conditions similar to that of a comet. A preliminary one-dimensional computation describes the structure of a granular shock formed from a spherical explosion. The two-dimensional axisymmetric calculations show that the explosion creates a cavity in the granular phase, and this cavity expands radially until it breaks through the surface. The blast wave created during the explosion initiates particle motions and forms a granular shock. The particles are initially entrained by the gas flow and then move by the granular shock. We demonstrate that there is a power-law relation between the explosion radius and time, and that this result is consistent with the blast-wave theory. At lower background temperatures, the velocities of both phases decrease, and this leads to more compact structures in the granular phase.

PARTICLE DISPERSAL OF DENSE GRANULAR MATERIALS IN HIGH-SPEED COMPRESSIBLE FLOW

by

Shuyue Lai

Dissertation submitted to the Faculty of the Graduate School of the
University of Maryland, College Park in partial fulfillment
of the requirements for the degree of
Doctor of Philosophy
2019

Advisory Committee:
Professor Elaine Oran, Chair/Advisor
Professor James Baeder
Professor Christine Hartzell
Professor Carolyn Kaplan
Professor Johan Larsson, Dean's Representative

Acknowledgments

First, I would like to thank Prof. Elaine S. Oran for her guidance and encouragement through my graduate career and acting as dissertation advisor and committee chair for this work, and Profs. Johan Larsson, James Baeder, Christine Hartzell, and Carolyn Kaplan for their efforts serving as doctoral committee members. I would also like to thank Prof. Ryan W. Houim for his comments and support throughout the course of this research.

The first project presented in this dissertation was supported in part by NIOSH Grant No. 200-2015-64091 and in part by the University of Maryland through Minta Martin Endowment Funds in the Department of Aerospace Engineering, and through the Glenn L. Martin Institute Chaired Professorship and the A. James Clark Distinguished Professorship at the A. James Clark School of Engineering. I would like to thank Mike Spako and Marcia Harris for their valuable comments and suggestions.

The second project was a proposal suggested by Prof. Jessica Sunshine. It was supported in part by the University of Maryland through Minta Martin Endowment Funds in the Department of Aerospace Engineering, and through the Glenn L. Martin Institute Chaired Professorship at the A. James Clark School of Engineering.

I would like to acknowledge the high-performance computing support from the University of Maryland supercomputing resources (http://www.glue.umd.edu/hpcc) for all simulations reported in this thesis.

Last, but not least, I would like to thank my parents for their love and support throughout my life.

TABLE OF CONTENTS

List of Tables

List of Figures

Chapter 1

INTRODUCTION

1.1 Motivation

Dust explosions have been a serious hazard for centuries in many industrial processes, such as coal mining, food processing, and grain storage. These explosions result from the ignition of the dispersed combustible dust that accumulates in the air. Moreover, secondary dust explosions can be much more destructive than a primary one [7, 8]. For example, in an underground coal mine, an initial explosion of natural gas generates shock waves that propagate through the mine channels. These shock waves interact with and disperse layers of coal dust, which can then ignite the hot, compressed environment. Ignition of dispersed coal particles may then lead to a secondary explosion. Fig. 1.1 shows some of the notable dust explosions in recent years.

To prevent dust explosions in coal mines, inert rock dust is usually applied for the inerting and suppressing of coal-dust dispersion and ignition. In fact, it is required by MSHA (Mine Safety and Health Administration) that the total incombustible content (TIC) is at least 80% when mixed with coal to prevent dust explosions [9]. Ideally, the rock dust, which is applied regularly to the dust surfaces during the mining operation, would suppress the dispersion of the coal dust underneath. In addition, a coal-rock

Figure 1.1: Examples of notable dust explosion incidents in recent years [3, 4, 5, 6].

mixture would be formed in the dispersed gas due to disturbances. The rock dust, then would act as a thermal inhibitor and prevent flame propagation [10]. In actual situations, a propagating shock wave could separate the rock and coal particles according to their different sizes and densities, and destroy the well-mixed rock-coal mixture. The ignition of the separated coal dust could still lead to a secondary explosion. Therefore, understanding how the dust cloud forms due to the propagating shock wave, and identifying the factors (such as particle size and density) influencing the level of particle dispersion is important to ensure safety in coal mines.

Inspired by the dust-lifting problem, we seek to design a granular model capable of accurately predicting the granular motion behind a moving shock wave. Using this model, we would like to answer the following questions: (1) What are the fundamental mechanisms of particle dispersal behind a propagating shock wave; (2) what are the factors influencing dust lifting and particle segregation; and (3) how much and how frequently inert dust needs to be applied for inerting an explosion. Moreover, applications of the proposed granular model are not limited to underground coal mine scenarios. We are also interested in applying the model to conditions that are very different from the coal mines, such as studying the cratering events on asteroids, comets, or terrestrial

planets, which are typically covered with loose granular materials.

1.2 Methodology of Study

The main objective of this research is to develop a granular model that can accurately represent the granular motion under high-speed compressible flow. This granular model needs to cover the range from dilute to densely packed regimes. In addition, it should be able to capture shock waves and shock-particle interactions, and account for different particle types to study the granular segregation phenomenon.

With the proposed model, the research aimed to gain an understanding of the mechanism of particle dispersal under high-speed flow through two problems: (1) dust lifting behind a moving shock wave, and (2) subsurface explosion in granular media. The methodology and the specific tasks to be achieved in this research are summarized in Fig. 1.2.

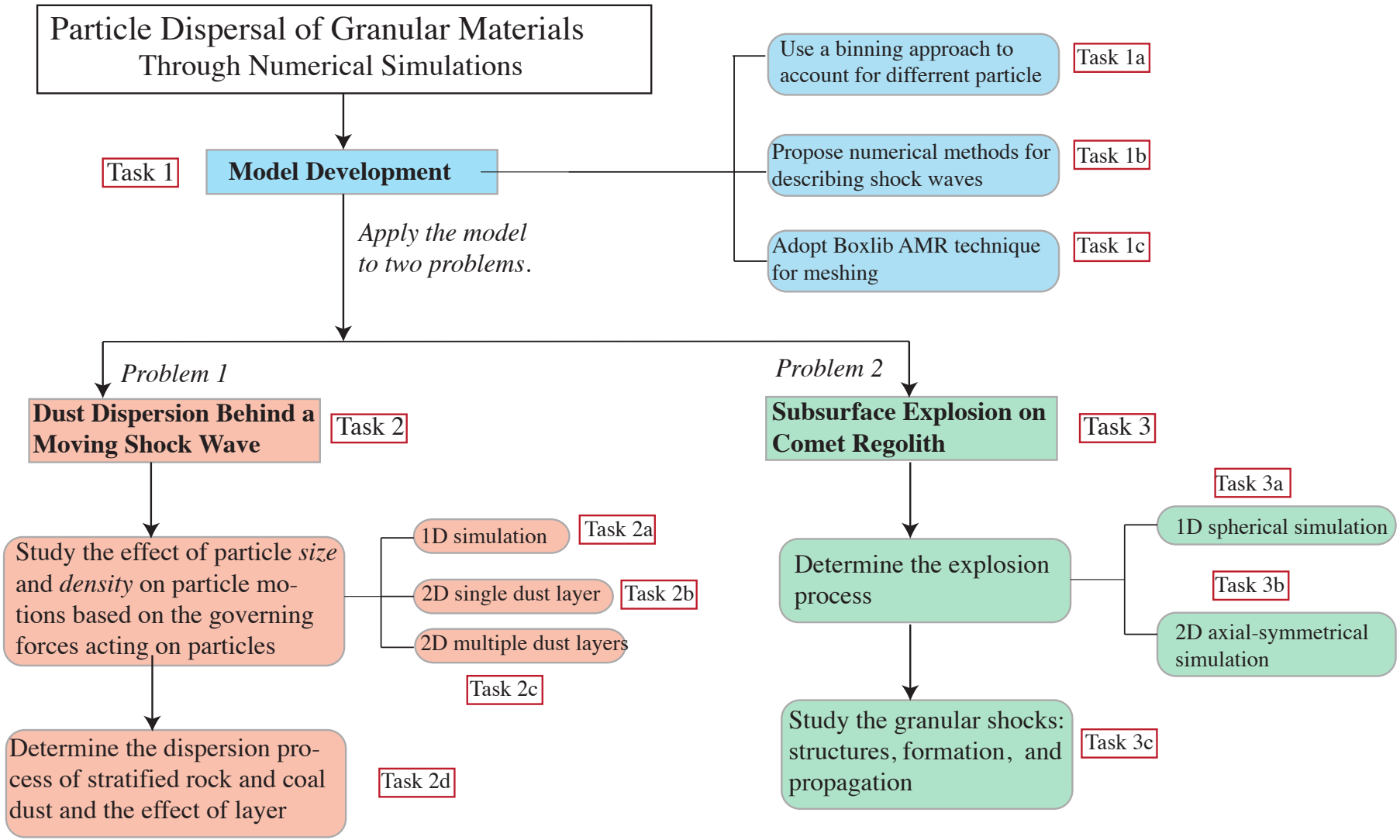

Figure 1.2: Methodology of the study on particle dispersal of granular materials.

1.3 Outline of the Dissertation

(1) Chapter I provides the motivation, the methodology, and the specific tasks for this research work.

(2) Chapter II presents the background information related to this study. This includes an introduction to granular materials, and a discussion of the general modelling methods of granular flows.

(3) Chapter III describes the numerical formulation of the proposed KTGF model. The model for the gas phase, each particle phase, and the intercoupling terms are presented.

(4) Chapter IV summarizes the numerical procedures and the multi-scale mesh refinement technique.

(5) Chapter V presents the study on dust dispersion behind a moving shock. The dispersion mechanism is analyzed in terms of the controlling forces acting on each type of particles. The particle segregation phenomenon due to different particle sizes and densities is examined. The dispersion of multiple dust layers and the effect of dust layer thickness are also discussed.

(6) Chapter VI studies the subsurface explosions in granular media corresponding to a comet regolith using the proposed model. This chapter focuses on understanding the particles ejection process, the effect of initial packing and background temperature on the explosion, and the formation and propagation of granular shocks.

(7) Chapter VII summarizes the conclusions and major technical contributions from this research. Possible modifications and extensions to the current model are proposed as future work.

Chapter 2

BACKGROUND AND LITERATURE REVIEW

2.1 Overview of Granular Materials

Granular materials are a large collection of discrete, macroscopic particles with an interstitial fluid such as air or water. They are everywhere in our universe and largely involved in many natural phenomena, such as avalanches, volcanic eruption, and formation of sand dunes, as well as in industries such as mining, agriculture, and construction [11]. It has been estimated that granular materials are second only to water as the most handled industrial material [12].

Despite the vast application of granular materials, the theoretical framework of granular flow is still poorly understood due to its dynamic, transitional behavior. Depending on the packing and the kinetic energy of the particles, the granular materials can behave as solids, liquids and gases. For example, sand on a beach can sustain stresses and behave like a solid, but sand in an hourglass flows like a liquid. If strongly agitated, sand can even behave like gas. Figure 2.1 shows the coexistence of three phases that have been observed in a simple sandpile flow.

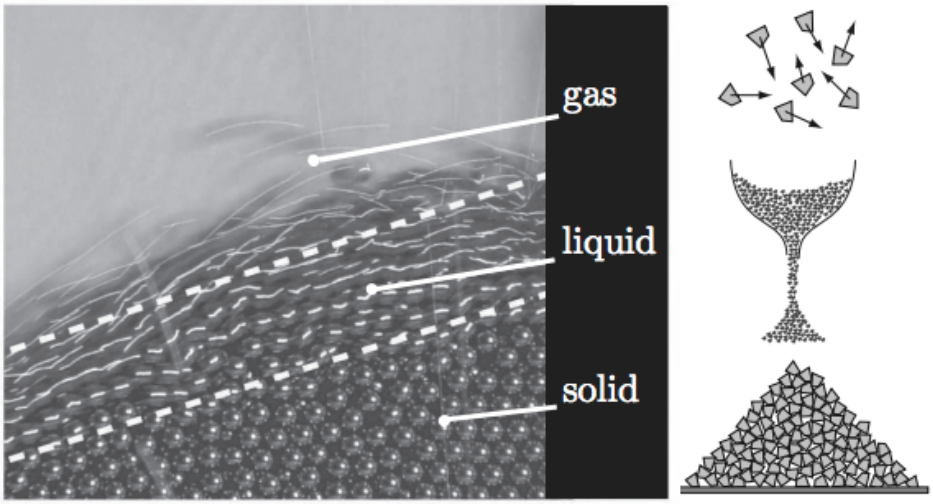

Figure 2.1: Granular flow can behave like solid, liquid, and gas, from Andreatti *et al.* [13]

Another interesting and puzzling phenomenon in granular flows is segregation. Unlike fluids, which usually mix by themselves, granular materials tend to unmix under external agitations. The most famous example is the "Brazil-nut effect" [14], named for the fact that larger nuts will move to the top of a shaken jar of nuts while the smaller ones will stay at the bottom. Here, nuts interact with each other by friction, which is largely dependent on their size and shape. Granular segregation can be used as a practical means to separate materials in industry, such as removing chaff from grain in a combine, and sorting materials in mineral processing industries [15]. In many other situations, however, granular segregation can be a persistent challenge. For example, in a fluidized bed coal gasifier, the separation between coal and hot circulating solid leads to low gasification efficiency [16]. In addition, separation between inert rock dust and reactive coal dust in underground coal mines may lead to a secondary dust explosion. Despite its importance to industries, the physics behind granular segregation is very complex and is still the subject of active research. Previous researchers have found that particle size, density, shape, surface material roughness, etc. are primary factors

influencing granular segregation.

2.2 Modeling of Granular Flow

2.2.1 Overview

Having the properties of granular flow in mind, we would like to develop a multi-fluid model that can recognize the complex nature of granular flows. The modelling of granular materials requires a combination of solid mechanics and fluid mechanics. Generally speaking, there are two most frequently used approaches for simulating granular flows depending on the choice of the two length scales: microscopic and macroscopic. At the microscopic scale, the particle phase is treated as discrete particles and each particle is tracked individually (Eulerian-Lagrangian approach). At the macroscopic scale, the particle phase is modeled as a continuum and the governing equations for a continuous, compressible media is solved (Eulerian-Eulerian approach). A brief summary of the discussed approaches and models are shown in Fig. 2.2.

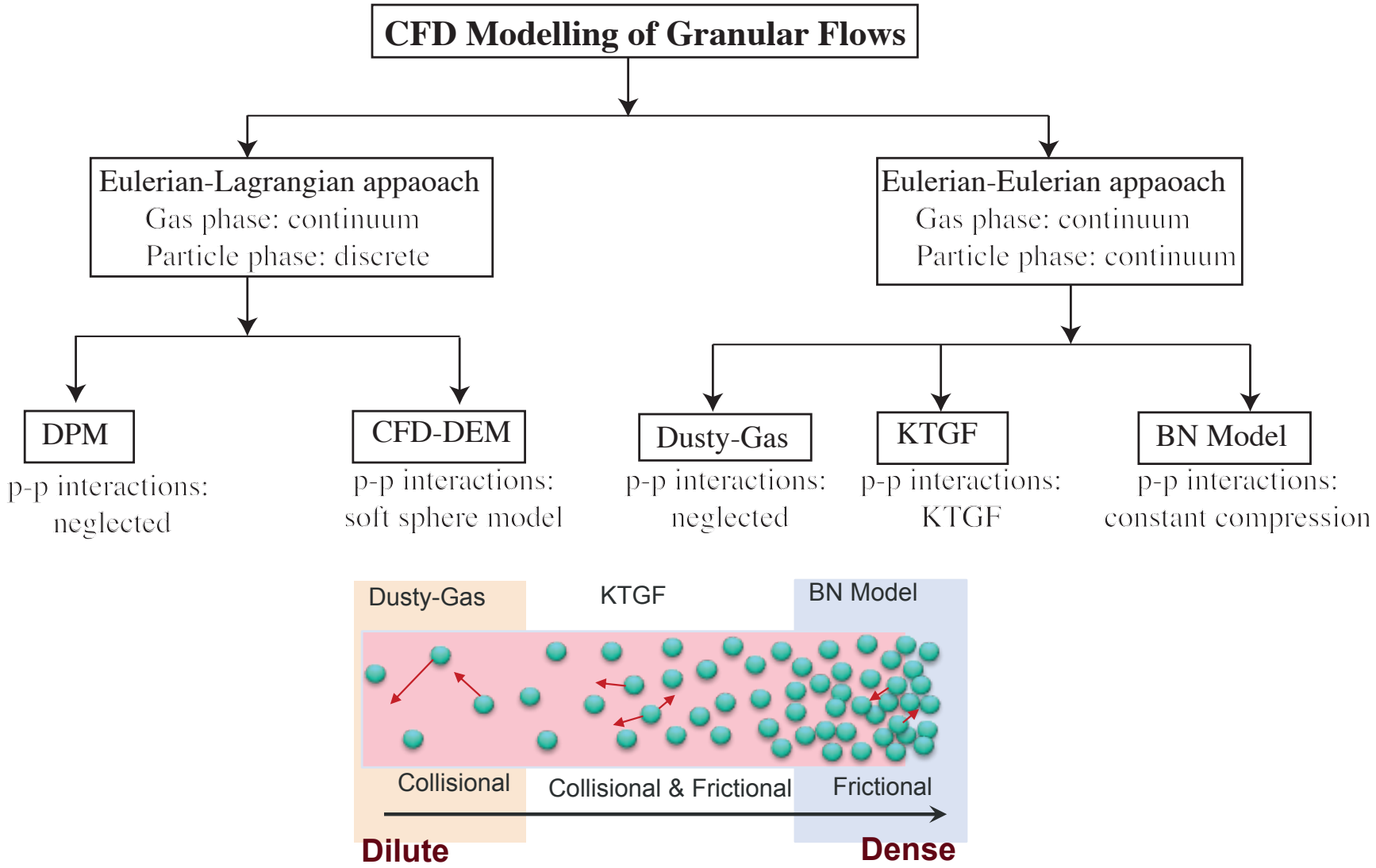

Figure 2.2: Summary of model approaches for gas-solid granular flow modelling.

2.2.2 Eulerian-Lagrangian Approach

In the Eulerian-Lagrangian approach, the gas phase is treated as a continuum while the dynamics of particles and particle interactions are described explicitly. The Eulerian-Lagrangian approach can capture physical behaviors of the granular flow more accurately than a continuum description. Nevertheless, the number of Lagrangian particles can grow very large and become computationally expensive for the calculations at dense regimes. Eulerian-Lagrangian models are available in many commercial codes including ANSYS Fluent [17], MFiX-DEM [18], and OpenFOAM [19]. Examples of current Eulerian-Lagrangian models include CFD-Discrete Element Method (DEM), and Discrete Phase Model (DPM).

The Discrete Element Method (DEM) or Distinct Element Method was originally proposed by Cundall and Strack in 1979 [20]. The DEM models were designed to apply in conditions where the particles having spacing comparable to the scale of interest of the problem, and have been used to investigate the motion of granular materials in a wide range of applications such as mill operation, and dragline excavation [21, 22]. In CFD-DEM, collisions and contact processes for each particle are obtained through integration of Newton's equation of motion.

For the Discrete Phase Model (DPM), particle-particle interactions are often neglected. Therefore, DPM is valid only for flows with a relatively low particle volume fraction. This model has either one-way or two-way coupling between gas and the particle phase through drag and turbulence [23] Compared with CFD-DEM, this model has a lower computational cost but provides less accurate results.

2.2.3 Eulerian-Eulerian Approach

Granular systems in the real world are usually made up of a large number of particles, and thus it is sometimes impractical to solve the motion of each individual

particle. The Eulerian-Eulerian approach gives an alternative option and can largely reduce the computation cost when an enormous number of particles are involved. In this approach, both gas and particle phases are treated as separate inter-penetrating and interacting fluids. The interacting forces between the different particle phases are calculated as source terms in the governing equations.

The continuum assumption requires that there exist sufficient number of particles within a computational cell and this can be invalid in the very dilute regimes such as the edge of a particle cloud. Moreover, properties of a particle obtained through this approach are averaged values of a number of particles instead of resolving each individual particle motion. Nevertheless, the continuum approach is generally considered to be accurate and efficient in CFD modeling of gas-solids multiphase flows. Eulerian-Eulerian models are available in many commercial multiphase models including ANSYS Fluent [17], MFiX [24], and OpenFOAM [19].

2.2.3.1 Dusty-Gas Model

One of the simplest Eulerian-Eulerian models is the dusty-gas model, which neglects particle-particle interactions and collisions [25, 1]. There exist two types of dusty-gas models, namely, equilibrium and non-equilibrium dusty-gas models, both assumes that the particle phase is dilute so that the dust does not contribute to the gas-phase pressure. For non-equilibrium models, we solve the conservation of mass, momentum, and energy for both the particle and gas phases. The gas phase and the particle phase are coupled only through the drag and the heat transfer terms.

The equilibrium model assumes that the relative velocities, and temperatures between the two phases are negligible (particle and gas in temperature and velocity equilibrium).

$$v_g = v_s, \quad T_g = T_s \tag{2.1}$$

As a result, the non-equilibrium model is also referred to as the *mixed-fluid model*, and solves only one momentum equation for the gas-particle mixture plus one equation to distinguish the dust from the gas. The equilibrium model has reduced the governing equations to a simpler form. The dusty-gas model allows simulations in dilute regimes, but is not valid in densely packed regimes where particle-particle collisions are important (e.g. shock-layer interaction).

2.2.3.2 Kinetic Theory of Granular Flows (KTGF)

KTGF is described as the most widely used Eulerian-Eulerian model, where the constitutive relations for the solid phase is derived from the kinetic theory of granular flow [26, 27, 28, 29, 30, 31]. KTGFs are typically used in simulations of high-speed granular flows with a relatively wide range of particle packing, such as volcanic eruptions, fluidized beds, and meteorite impacts [30, 32, 33].

KTGF is an analogy to the kinetic theory for gas flow, in which particles interact through collisions in a similar way as the collisions of a molecular gas. Unlike gas-molecule collisions, which are completely elastic, particle collisions are slightly inelastic. There is a coefficient of restitution, e, representing the inelasticity of the particle collisions and resulting in energy losses from inelastic collisions between particles.

One of the most important terms in KTGFs is the granular temperature. Savage and Jeffrey [34], and Jekins and Savage [35] were the first to relate the fluctuation velocity to the shear gradient and introduced the concept of granular temperature (Θ_s). The granular temperature measures the random oscillation of the particles and is defined as one-third the mean square fluctuation velocity.

$$\theta_s = \frac{1}{3}\langle u^2 \rangle, \quad E_s = \frac{3}{2}\theta_s. \tag{2.2}$$

where $\langle u^2 \rangle$ represents the average of the square of the fluctuating velocity. The quantity E_s is the kinetic energy associated with the granular temperature (particle fluctuation),

and is often referred to as, Pseodo-Thermal Energy (PTE).

Most KTGF models assume that all particles have one size and density. In real granular systems, particles generally have a wide range of sizes and densities. The phenomenon of particle segregation due to different sizes and densities occurs both in nature and industrial process [16]. Efforts have been made to extend the KTGF model to incorporate particle mixtures with different properties recently. The first attempt was by Jenkins and Mancini for a planar flow of a dense, binary mixture of smooth, nearly elastic, circular disks [36]. In this work, equipartition of granular energy for each particle type was assumed for simplicity. Based on this work, Mathiesen *et al.* [32] extended the KTGF with one gas and N solid phases. Later, Gidaspow *et al.* [37], Manger [38], and Huilin *et al.* [39] removed the assumption of equal granular energy and solved for the granular temperature explicitly for each particle phase. Based on their study, a generalized multifluid model is proposed by Mathiesen *et al.* [40].

2.2.3.3 Baer-Nunziato Model

In a denser fluidized bed, where particle-particle collisions are primarily frictional, the use of granular kinetic theory is inadequate. The Baer-Nunziato (BN) model is an example to handle particle flows with high volume fractions, and is developed to simulate the deflagration-to-detonation process, where particle compression and distortion is significant [41, 42, 1]. This type of model relaxes the incompressible assumption for the particle phase as described in the KTGF, and solves separate continuum laws and equations of state [1]. The Baer-Nunziato model is a type of the seven-equation model, where we solve the conservation of mass, momentum, and energy for both fluid phases plus one advection equation for the solid volume fraction in a non-conservative form:

$$\frac{\partial \alpha_s}{\partial t} + \boldsymbol{v_s} \cdot \nabla \alpha_s = 0. \tag{2.3}$$

This addition equation for the particle volume fraction accounts for compressibility by recognizing the volume fraction as an independent internal degree of freedom within the mixture. As a result, the volume fraction changes only at solid contact surfaces [1]. The BN model is valid for highly packed granular flows where particles are in constant compressive contact with each other.

Chapter 3

MODEL FORMULATIONS

3.1 Overview

The model used in this research is an extension of the KTGF granular model proposed by Houim and Oran [1]. In this model, the constitutive relations for the particle phases are derived from the Kinetic Theory of Granular Flow (KTGF). Multiple particle types are considered through a binning approach to study the particle segregation phenomenon. Particles in each bin have their own uniform particle size and diameter, and each bin of particles adds an additional set of governing equations and can have different properties. As a result, this model involves solving (M+1) sets of coupled Euler equations, one for the gas phase, and M for the M different particle phases. The sum of the volume fractions occupied by gas and the granular mixtures is equal to unity,

$$\alpha_g + \sum_{m=1}^{M} \alpha_{s,m} = 1, \tag{3.1}$$

where α_g, $\alpha_{s,m}$ are the volume fractions for gas phase and the m^{th} particle phase.

The current model neglects several terms, including the effects of phase changes, granular energy exchange between different particle bins, the dissipation of granular energy due to inelastic collisions between different particle bins, and the granular viscous

stress terms [2]. Justifications for neglecting these terms will be discussed in Section 5.3.4.4.

3.2 Model for Gas Phase

The conservation of mass, momentum, and energy equations for the gas phase are

$$\frac{\partial \alpha_g \rho_g}{\partial t} + \boldsymbol{\nabla}\cdot(\alpha_g \rho_g \boldsymbol{v}_g) = 0, \tag{3.2}$$

$$\frac{\partial \alpha_g \rho_g \boldsymbol{v}_g}{\partial t} + \boldsymbol{\nabla}\cdot(\alpha_g \rho_g \boldsymbol{v}_g \boldsymbol{v}_g) = -\alpha_g \nabla p_g + \alpha_g \rho_g \boldsymbol{g} + \boldsymbol{S}_g^p, \tag{3.3}$$

and

$$\frac{\partial \alpha_g \rho_g E_g}{\partial t} + \boldsymbol{\nabla}\cdot[\alpha_g \boldsymbol{v}_g(\rho_g E_g + p_g)] = -p_g \sum_{m=1}^{M} \boldsymbol{\nabla}\cdot(\alpha_{s,m}\boldsymbol{v}_{s,m}) + \alpha_g \rho_g \boldsymbol{g}\cdot\boldsymbol{v}_g + S_g^E. \tag{3.4}$$

Here α_g, ρ_g, $\boldsymbol{v_g}$, p_g, and E_g represent the volume fraction, density, velocity, pressure, and total energy of the gas phase. The quantities $\alpha_{s,m}$ and $\boldsymbol{v_{s,m}}$ are volume fractions and velocities for the m^{th} type of particle phase. The interphase coupling terms describing transfer of momentum and energy between the gas and particles are denoted by $\boldsymbol{S}_g^p$ and S_g^E.

The ideal-gas equation-of-state is used for the gas phase. The gas-phase total energy, E_g, is defined by

$$E_g = \frac{p_g}{\rho_g(\gamma - 1)} + \frac{1}{2}\boldsymbol{v}_g \cdot \boldsymbol{v}_g. \tag{3.5}$$

where γ is the ratio of specific heats.

3.3 Model for Solid Phase

The conservation of mass, momentum, Pseudo-Thermal Energy (PTE), and kinetic energy for solid phase l are

$$\frac{\partial \alpha_{s,l} \rho_{s,l}}{\partial t} + \boldsymbol{\nabla}\cdot(\alpha_{s,l} \rho_{s,l} \boldsymbol{v}_{s,l}) = 0, \tag{3.6}$$

$$\frac{\partial \alpha_{s,l}\rho_{s,l}\boldsymbol{v}_{s,l}}{\partial t} + \boldsymbol{\nabla}\cdot(\alpha_{s,l}\rho_{s,l}\boldsymbol{v}_{s,l}\boldsymbol{v}_{s,l}) + \boldsymbol{\nabla}p_{sl,\mathrm{tot}} = -\alpha_{s,l}\boldsymbol{\nabla}p_g + \alpha_{s,l}\rho_{s,l}\boldsymbol{g} - \boldsymbol{S}^p_{g,l} - \boldsymbol{S}^p_{s,l}, \quad (3.7)$$

$$\frac{\partial \alpha_{s,l}\rho_s E_{s,l}}{\partial t} + \boldsymbol{\nabla}\cdot(\alpha_{s,l}\rho_{s,l}E_{s,l}\boldsymbol{v}_{s,l}) = -p_{s,l}\boldsymbol{\nabla}\cdot\boldsymbol{v}_{s,l} + S^{PTE}_{s,l}, \quad (3.8)$$

$$\frac{\partial \alpha_{s,l}\rho_{s,l}e_{s,l}}{\partial t} + \boldsymbol{\nabla}\cdot(\alpha_{s,l}\rho_{s,l}e_{s,l}\boldsymbol{v}_{s,l}) = S^{E}_{s,l}. \quad (3.9)$$

Here α_s, ρ_s, $\boldsymbol{v_s}$, p_s, e_s, and E_s represent the volume fraction, density, velocity, pressure, internal energy, and Pseudo-Thermal Energy (PTE, i.e., the energy due to random translational motion of particles [1]) of the particle phase. The interphase coupling terms describing transfer of momentum and energy between the gas and particles are denoted by $\boldsymbol{S}^p_{g,l}$, $\boldsymbol{S}^p_{s,l}$, $S^{PTE}_{s,l}$, and $S^E_{s,l}$.

3.3.1 Granular Temperature

For granular-gas models based on the Kinetic Theory of Granular Flow (KTGF), a granular temperature (Θ_s) is introduced, analogous to the temperature for regular gas. This quantity is proportional to the mean quadratic velocity of the random motion of the particles,

$$\Theta_s = \frac{1}{3}\langle u^2\rangle, \quad (3.10)$$

where Θ_s and u are the granular temperature and the velocity of the particles. The quantity $\langle u^2\rangle$ represents the average of the square of the fluctuating velocity. As a result, Θ_s represents the degree of disorder within a system, and usually have units of $\mathrm{m}^2/\mathrm{s}^2$ instead of K for gas temperature. The granular temperature is equal to 0 when the particles are closely packed and there is no space for oscillation. The granular energy, or Pseudo-Thermal Energy (E_s) is defined as,

$$E_s = \frac{3}{2}\Theta_s. \quad (3.11)$$

3.3.2 Solids Pressure

Solids pressure, analogous to the gas-phase pressure, is a "thermodynamic" pressure for the particles and it represents the collisional effect within the dust mixtures. For a granular system containing monotonic particle types, the solids pressure (p_s) is [31]

$$p_s = \alpha_s \rho_s \theta_s [1 + 2(1+e)\alpha_s g_0]. \tag{3.12}$$

Here the quantities e, and g_0 are the coefficient of restitution, and the radial distribution function for the granular system. The first part of the equation, $\alpha_s \rho_s \theta_s$, represents the pressure due to the particle fluctuation, and the second part of the equation, $\alpha_s \rho_s \theta_s \times 2(1+e)\alpha_s g_0$, corresponds to the collisional effects of the particles. The radial distribution function, g_0, describes the probability of two particle colliding with each other when the granular phase becomes dense. The coefficient of restitution, e, is related to the elasticity of the collisions.

For granular systems containing two or more types of particles, the expression for the solids pressure becomes more complicated. For the l^{th} particle phase in a polydispersed system, we need to consider the collisional effect within particle type l as well as the collisional effects with other types of particles. The expression for the solids pressure is defined as [43]

$$P_{s,l} = \alpha_{s,l} \rho_{s,l} \Theta_{s,l} + \sum_{m=1}^{M} P_{c,lm}. \tag{3.13}$$

Here $P_{c,lm}$ is the collisional pressure between particle type l and m, and $\alpha_{s,l} \rho_{s,l} \Theta_{s,l}$ is the kinetic term. $P_{c,lm}$ is defined as [43],

$$\begin{aligned} P_{c,lm} = & \frac{\pi(1+e) d_{lm}^3 g_{0,lm} n_l n_m m_l m_m m_0 \theta_l \theta_m}{3(m_l^2 \theta_l + m_m^2 \theta_m)} \\ & \times \left[\frac{m_0^2 \theta_l \theta_m}{(m_l^2 \theta_l + m_m^2 \theta_m)(\theta_l + \theta_m)} \right]^{3/2} \\ & \times (1 - 3\Delta + 6\Delta^2 - 10\Delta^3), \end{aligned} \tag{3.14}$$

where e is the coefficient of restitution, and $g_{0,lm}$ is the radial distribution function between particle type l and m. For a mixture of hard spheres, the following expression is used [24]:

$$g_{0,lm} = \frac{1}{\alpha_g} + \frac{3 d_l d_m}{\alpha_g^2 (d_l + d_m)} \sum_{q=1}^{M} \frac{\alpha_q}{d_q}, \tag{3.15}$$

where d_l and d_m are the particle diameters for the l^{th} and m^{th} types of particles.

The quantity m_l is the mass of a particle and n_l is the number of particles. For spherical particles,

$$m_l = \frac{\pi}{6} d_l^3 \rho_l, \tag{3.16}$$

$$n_l = \frac{6 \alpha_l}{\pi d_l^3}, \tag{3.17}$$

$$d_{lm} = \frac{d_l + d_m}{2}, \tag{3.18}$$

$$m_0 = (m_l + m_m), \tag{3.19}$$

and

$$\Delta = \frac{m_l \theta_l - m_m \theta_m}{[(m_l^2 \theta_l^2 + m_m^2 \theta_m^2) + \theta_l \theta_m (m_l^2 + m_m^2)]^{1/2}}. \tag{3.20}$$

The *total intergranular stress* acting on the particles is defined as the sum of the solids and frictional pressure,

$$P_{sl,tot} = P_{s,l} + P_{fric,l}. \tag{3.21}$$

The frictional pressure for particle type l, $P_{fric,l}$, represents the effect of friction between particles, and this is essential for preventing the particle phase in dense region from packing to an unphysically high level [1]. The relation used here is developed by Johnson and Jackson [29] and now modified based on the law of partial pressure from kinetic theory,

$$P_{fric,l} = \begin{cases} 0 & \text{if } \alpha_{s,tot} < \alpha_{s,crit} \\ 0.1 \dfrac{(\alpha_{s,tot} - \alpha_{s,crit})^2}{(\alpha_{s,max} - \alpha_{s,tot})^5} \alpha_{s,l} & \text{if } \alpha_{s,tot} \geqslant \alpha_{s,crit}, \end{cases} \tag{3.22}$$

where $\alpha_{s,crit}$ is set to be a critical value of 0.5.

3.3.3 Maximum Packing Limit

The maximum packing limit (or the random close packing) is an empirical parameter used to characterize the maximum volume fraction can be achieved when they are packed randomly. For monotonic spherical particles, the maximum packing limit ($\alpha_{s,max}$) is 0.65 [31]. For a granular system containing multiple particle types that are mixed with each other, the maximum packing limit is calculated with the correlations developed by Yu and Standish [44][45].

$$\alpha_{s,mix}^{max} = min\{\frac{\alpha_{s,i}^{max}}{1-\sum_{j=1}^{i-1}(1-\frac{\alpha_{s,i}^{max}}{pi,j}\frac{cx_i}{X_{ij}})-\sum_{j=i+1}^{M}\frac{\alpha_{s,i}^{max}}{pi,j}\frac{cx_i}{X_{ij}}}\}, \qquad i=1,2,...,M \tag{3.23}$$

where

$$cx_i = \frac{\alpha_{s,i}}{\sum_{j=1}^{M}\alpha_{s,j}}, \tag{3.24}$$

$$X_{i,j} = \begin{cases} \frac{1-r_{ij}^2}{2-\alpha_{s,i}^{max}} & \text{if } j < i \\ 1-\frac{1-r_{ij}^2}{2-\alpha_{s,i}^{max}} & \text{if } j \geqslant i, \end{cases} \tag{3.25}$$

$$p_{ij} = \begin{cases} \alpha_{s,i}^{max}+\alpha_{s,i}^{max}(1-\alpha_{s,i}^{max})(1-2.35r_{ij}+1.35r_{ij}^2) & \text{if } r_{ij} < 0.741 \\ \alpha_{s,i}^{max} & \text{if } r_{ij} \geqslant 0.741, \end{cases} \tag{3.26}$$

and

$$r_{ij} = \begin{cases} \frac{d_{p,i}}{d_{p,j}} & \text{if } i \geqslant j \\ \frac{d_{p,j}}{d_{p,i}} & \text{if } i < j. \end{cases} \tag{3.27}$$

Here $\alpha_{s,i}^{max}$ is the maximum packing limit of individual solid phase i.

Based on the correlations above, dust mixtures with particle diameters that are closer together have a lower packing limit.

3.3.4 Compaction wave speed

The granular compaction wave speed, analogous to the acoustic wave speed in gas flow, describes the local speed of sound in a granular fluid. Analytical solutions to the

compaction wave speed for a polydispersed system can be derived with averaged particle properties (density, granular temperature, pressure, etc.). The calculated compaction wave speed , $c_{s,mix}$, is a mixed valued and is shared by all solid phases. The equations for the mixed compaction wave speed for a polydispersed granular phase are,

$$c_{s,mix}^2 = \frac{1}{\rho_{mix}}[\frac{\partial(P_{s,mix} + P_{fric,mix})}{\partial\alpha_{mix}}|_{\Theta_{mix}} + \frac{2}{3}\frac{\Theta_{mix}(\frac{\partial P_{mix}}{\Theta_{mix}}|_{\alpha_{mix}})^2}{\rho_{mix}\alpha_{mix}^2}], \tag{3.28}$$

$$c_s^2 = \theta_s(A + \frac{2}{3}A^2 + \alpha_s B) + c_{fric,mix}^2, \tag{3.29}$$

where

$$A = 1 + 2(1+e)\alpha_{mix}g_{0,mix}, \tag{3.30}$$

$$B = 2(1+e)(g_{0,mix} + \alpha_{mix}g'_{0,mix}), \tag{3.31}$$

and

$$g'_{0,mix} = \frac{g_{0,mix}^2}{3\alpha_{s,max}}(\frac{\alpha_{s,max}}{\alpha_{s,mix}})^{2/3}. \tag{3.32}$$

Here averaged properties for the dust mixtures are used,

$$\alpha_{s,mix} = \sum_{m=1}^{M}\alpha_{s,m}, \tag{3.33}$$

$$\rho_{mix} = \frac{\sum_{m=1}^{M}\alpha_{s,m}\rho_{s,m}}{\alpha_{s,mix}}, \tag{3.34}$$

$$\frac{1}{g_{0,mix}} = 1 - (\frac{\alpha_{s,mix}}{\alpha_{s,max}})^{1/3}, \tag{3.35}$$

and

$$\Theta_{s,mix} = \frac{\sum_{m=1}^{M}\alpha_{s,m}\rho_{s,m}\Theta_{s,m}}{\sum_{m=1}^{M}\alpha_{s,m}\rho_{s,m}}. \tag{3.36}$$

These mixed values are only used to calculate the granular compaction wave speed ($c_{s,mix}$), which is shared by all particle phases, and is not intended for describing the state of motion for the granular system.

3.4 Coupling Terms

3.4.1 Gas-Solids Momentum Transfer

The momentum transfer term between the gas phase and the l^{th} particle phase, $\boldsymbol{S}^p_{g,l}$, and the momentum transfer between the gas phase and all the particle phases, $\boldsymbol{S}^p_g$, are

$$\boldsymbol{S}^p_{g,l} = \boldsymbol{f}_{\text{Drag,gl}} + \boldsymbol{f}_{\text{Lift,gl}}, \tag{3.37}$$

and

$$\boldsymbol{S}^p_g = \sum_{m=1}^{M} \{\boldsymbol{f}_{\text{Drag,gm}} + \boldsymbol{f}_{\text{Lift,gm}}\}, \tag{3.38}$$

where the quantities $\boldsymbol{f}_{\text{Lift,gm}}$ and $\boldsymbol{f}_{\text{Drag,gm}}$ are the lift and drag forces acting between gas phase and the m^{th} particle phase. The drag force is caused by the velocity difference between gas and particles. Here, we use the Gidaspow drag correlation [31],

$$\boldsymbol{f}_{Drag,gm} = K_{gm}(\boldsymbol{v}_{s,m} - \boldsymbol{v}_g), \tag{3.39}$$

where K_{gm} is the gas-solid exchange coefficient. The Gidaspow model is used again for K_{gm}, which is a combination of the Wen and Yu model and the Ergun model [31, 46, 47],

$$K_{gm} = \begin{cases} 0.75 C_d \frac{\rho_g \alpha_g \alpha_s |\boldsymbol{v}_{s,m} - \boldsymbol{v}_g|}{d_{s,m} \alpha_g^{2.65}} & \text{if } \alpha_g \geqslant 0.8 \\ 150 \frac{\alpha_{s,m}^2 \mu_g}{\alpha_g d_{s,m}^2} + 1.75 \frac{\rho_g \alpha_{s,m} |\boldsymbol{v}_{s,m} - \boldsymbol{v}_g|}{d_{s,m}} & \text{if } \alpha_g < 0.8, \end{cases} \tag{3.40}$$

where the drag coefficient C_d is defined as

$$C_d = \begin{cases} 24(\alpha_g Re)^{-1}[1 + 0.15(\alpha_g Re)^{0.687}] & \text{if } \alpha_g Re < 1000 \\ 0.44 & \text{if } \alpha_g Re \leqslant 1000, \end{cases} \tag{3.41}$$

and the Reynolds number is

$$Re = \frac{\rho_g |\boldsymbol{v}_{s,m} - \boldsymbol{v}_g| d_{s,m}}{\mu_g}. \tag{3.42}$$

The lift force, $f_{Lift,gm}$, acting on the gas phase is modelled by the Magnus lift force [48] and it accounts for the rotational effect of the particles,

$$\boldsymbol{f}_{Lift,gm} = C_l \alpha_s \rho_g (\boldsymbol{v}_{s,m} - \boldsymbol{v}_g) \times (\boldsymbol{\nabla} \times \boldsymbol{v}_g), \tag{3.43}$$

where C_l is the lift coefficient, which typically takes a value of 0.5.

3.4.2 Solids-Solids Momentum Transfer

The solids-solids momentum transfer term $\boldsymbol{S}^p_{s,l}$ accounts for the particle-hindrance effect (drag-like term) between different particle phases,

$$\boldsymbol{S}^p_{s,l} = \sum_{\substack{m=1 \\ m \neq l}}^{M} \{\boldsymbol{f}_{\text{Hind,lm}}\}, \tag{3.44}$$

where the correlations for the particle-hindrance force is derived by Gidaspow [31],

$$\boldsymbol{f}_{\text{Hind,lm}} = K_{lm}(\boldsymbol{v}_l - \boldsymbol{v}_m). \tag{3.45}$$

The solid-solid exchange coefficient between particle type l and m is [49],

$$K_{lm} = \frac{(\frac{\pi}{2} + C_{fr,lm}\frac{\pi^2}{8})\alpha_l \rho_l \alpha_m \rho_m (d_l + d_m)^2 g_{0,lm}}{2\pi(\rho_l d_l^3 + \rho_m d_m^3)} \times (1 + e_{lm})|\boldsymbol{v}_l - \boldsymbol{v}_m|, \tag{3.46}$$

where e_{lm} is the coefficient of restitution and $C_{fr,lm}$ is the coefficient of friction between particle type l and type m. In this work, the friction between different particle types is neglected ($C_{fr,lm} = 0$).

3.4.3 Summary of Forces Acting on Particles

Figure 3.1 shows the forces (i.e., the terms on the right hand side of the particle momentum equation) acting on a particle in a granular flow. The equations of these governing forces have been discussed in the above sections and are summarized here in Table 3.1. They are Archimedes force, intergranular stress, drag, lift, particle-hindrance

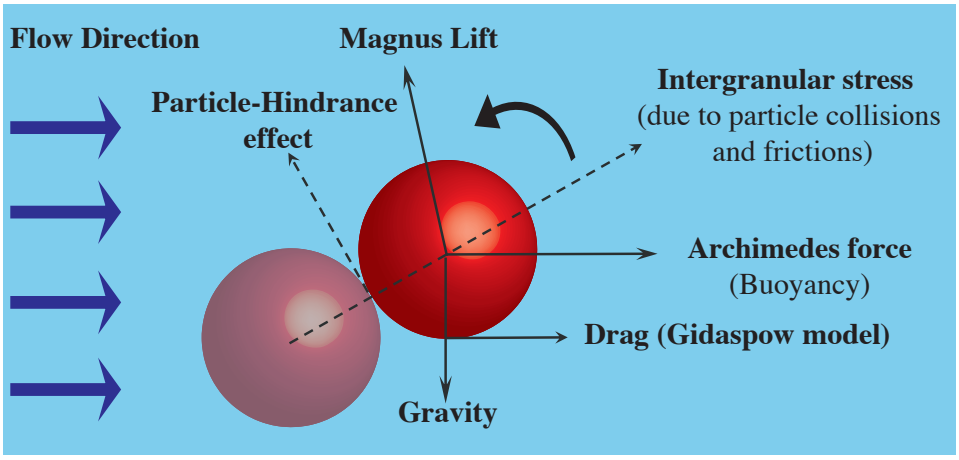

Figure 3.1: Forces acting on a particle in a granular flow containing multiple particle types.

Table 3.1: Forces acting on particle type l

(1) Archimedes Force	$-\alpha_{s,l}\nabla p_g$
(2) Intergranular Stress	$-\nabla p_{s,l} - \nabla p_{fric,l}$
(3) Drag	$K_{lg}(\boldsymbol{v_g} - \boldsymbol{v_{s,l}})$
(4) Lift	$C_l\alpha_{s,l}\rho_g(\boldsymbol{v_g} - \boldsymbol{v_{s,l}}) \times (\nabla \times \boldsymbol{v_g})$
(5) Particle-hindrance force	$\sum_{m=1,m\neq l}^{M} K_{s,lm}(\boldsymbol{v_{s,l}} - \boldsymbol{v_{s,m}})$
(6) Gravitational	$\alpha_{s,l}\rho_{s,l}\boldsymbol{g}$

force, and gravity. The lift and drag forces result from the velocity difference between the l^{th} particle phase and the gas. The Archimedes force is due to the gas-phase pressure pushing on the particles. The intergranular stress corresponds to the collisional and frictional effect within the granular mixture. The particle-hindrance force is a drag-like term between two different types of particles.

3.4.4 Energy Transfer Mechanisms

The source terms in the energy equations are

$$S_g^E = \sum_{m=1}^{M} \{(\boldsymbol{f}_{\text{Drag,gm}} + \boldsymbol{f}_{\text{Lift,gm}}) \cdot \boldsymbol{v}_g - q_{conv,gm} + \phi_{visc,gm} - \phi_{slip,gm}\}, \tag{3.47}$$

$$S_{s,l}^{PTE} = -\dot{\gamma}_l - \phi_{visc_gl} + \phi_{slip_{gl}}, \tag{3.48}$$

$$S_{s,l}^{E} = q_{conv,gl} + \dot{\gamma}_l, \tag{3.49}$$

where $-q_{conv,gl}$, $\phi_{visc,gm}$, $\dot{\gamma}_l$, and $\phi_{slip,gm}$ are convective heat transfer [1], dissipation of PTE due to gas-phase viscosity [31], dissipation of PTE due to inelastic particle collisions [27], and production of PTE due to drag force [50].

The heat exchange between the m^{th} particle phase and gas phase, $q_{\text{conv}_{gm}}$, is defined as a function of temperature difference,

$$q_{\text{conv}_{gm}} = h_{\text{mg}}(T_g - T_{s,m}), \tag{3.50}$$

where the heat exchange coefficient h_{mg} is a correlation proposed by Bird *et al.*, [51]

$$h_{\text{mg}} = 6\frac{\alpha_{s,m}\lambda_g Nu_m}{d_{s,m}^2}. \tag{3.51}$$

The Nusselt number, Nu_m, is estimated using the work by Gunn [52],

$$\begin{aligned} Nu_m = &(7 - 10\alpha_g + 5\alpha_g^2)(1 + 0.7Re_m^{0.2}Pr_g^{1/3}) \\ &+(1.33 - 2.4\alpha_g + 1.2\alpha_g^2)Re_m^{0.7}Pr_g^{1/3}. \end{aligned} \tag{3.52}$$

Here Pr_g is the gas phase Prandtl number, and λ_g is the gas phase thermal conductivity. The Reynolds number related to particle type m is

$$Re_m = \frac{\rho_g |\boldsymbol{v}_{s,m} - \boldsymbol{v}_g| d_{s,m}}{\mu_g}. \tag{3.53}$$

The energy transfer from PTE to kinetic energy due to viscous damping is represented by $\phi_{\text{visc}_{gm}}$ [31],

$$\phi_{\text{visc}_{gm}} = 3K_{\text{mg}}\theta_{s,m}. \tag{3.54}$$

This coefficient h_{mg} is applicable for a porosity range of 0.35-1.0 and a Reynolds number up to 10^5 [16].

The PTE production due to slip between gas and particle type m is [50]

$$\phi_{\text{slip}_{gm}} = \frac{81\alpha_{s,m}\mu_g^2}{g_0 d_{s,m}^3 \rho_{s,m}\sqrt{\pi}} \frac{\rho_s \theta_{s,m}^{3/2}}{d_{s,m}}. \tag{3.55}$$

The dissipation of PTE due to collisions between particles is given by [27],

$$\dot{\gamma}_l = \frac{12(1-e^2) g_{0,ll} \alpha_{s,l}^2}{\sqrt{\pi}} \frac{\rho_{s,l} \theta_{s,l}^{3/2}}{d_{s,l}}. \tag{3.56}$$

The relationship between the energy transfers discussed above is shown in Fig. 3.2 for a system containing one gas phase and one particle phase. Note that the kinetic energy of the granular phase is excluded from the governing equations to avoid small truncation errors, which can lead to unphysical values of PTE [1]. Increasing the number of bins will introduce additional transferring terms between the gas phase and the additional particle phase, and thus create a more complicated transfer mechanism. The energy transfer diagram for a system containing one gas phase and two particle phases are shown in Fig. 3.3.

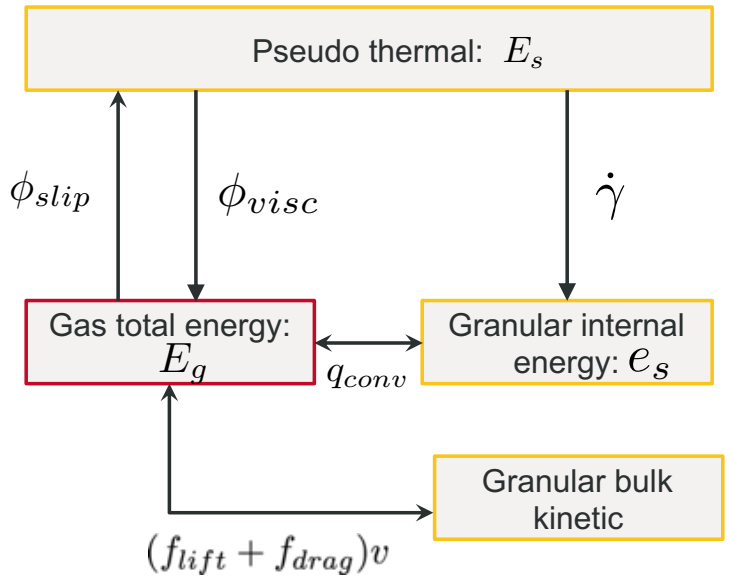

Figure 3.2: Relationship between the energy transfer mechanism modelled in the energy source terms for a system containing one gas phase and one particle phase.

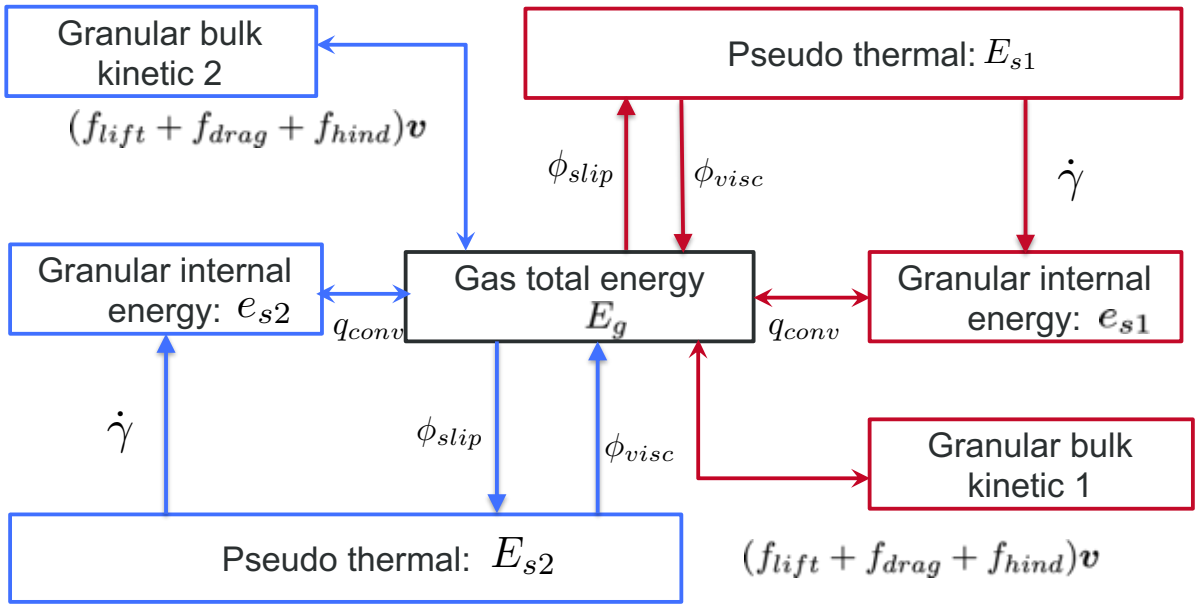

Figure 3.3: Relationship between the energy transfer mechanism modelled in the energy source terms for a system containing one gas phase and two particle phases.

Chapter 4

NUMERICAL METHODS

4.1 Overview

To solve the compressible Euler equations, an operator-splitting algorithm is used to integrate the hyperbolic terms and the source terms. The hyperbolic terms are solved using a high-order Godunov-based scheme [53], where the primitive variables are implemented using a MUSCL method with a third order parabolic reconstruction. A total variation diminishing (TVD) scheme with minmod slope limiter is also adopted to reduce small oscillations near discontinuities. A modified HLLC method, which returns primitive variables directly, is used to solve for the gas-phase flux. The granular flux is computed using a modified AUSM+ -up method, which has an increased dissipation in highly packed regions. The Strang operator [1] further splits the source terms into two parts: (1) drag, particle-hindrance effect, convective heat transfer, and (2) pseudothermal energy production and dissipation. These source terms are integrated analytically into the solutions [54]. The solution algorithm uses a third-order Runge-Kutta scheme [55] for time advancement. Adaptive mesh refinement is implemented through the Boxlib [56] or Paramesh [57] library. This numerical approached is modified based on the prior work of Houim and Oran [1]. The integration of the hyperbolic terms and source terms

are discussed in detail in the following sections.

4.2 Integration of the Hyperbolic Terms

4.2.1 Semi-discrete forms of the hyperbolic terms

The semi-discrete forms of the hyperbolic terms for the gas phase and the l^{th} particle phase with index i and a grid size Δx in one dimension are

$$\frac{\mathrm{d}(\alpha_g \rho_g)_i}{\mathrm{d}t} = -\frac{\alpha_{g,i+1/2}\rho_{g,i+1/2}u_{g,i+1/2} - \alpha_{g,i-1/2}\rho_{g,i-1/2}u_{g,i-1/2}}{\Delta x}, \tag{4.1}$$

$$\begin{aligned}\frac{\mathrm{d}(\alpha_g \rho_g u_g)_i}{\mathrm{d}t} = &-\frac{\alpha_{g,i+1/2}\rho_{g,i+1/2}u_{g,i+1/2}u_{g,i+1/2} - \alpha_{g,i-1/2}\rho_{g,i-1/2}u_{g,i-1/2}u_{g,i-1/2}}{\Delta x} \\ &-\alpha_{g,i}\frac{p_{g,i+1/2} - p_{g,i-1/2}}{\Delta x} + \alpha_{g,i}\rho_{g,i}g_x,\end{aligned} \tag{4.2}$$

$$\begin{aligned}\frac{\mathrm{d}(\alpha_g \rho_g E_g)_i}{\mathrm{d}t} = &-\frac{\alpha_{g,i+1/2}\rho_{g,i+1/2}u_{g,i+1/2}H_{g,i+1/2} - \alpha_{g,i-1/2}\rho_{g,i-1/2}H^{+}_{g,i-1/2}u_{g,i-1/2}}{\Delta x} \\ &-p_{g,i}\sum_{m=1}^{M}\frac{\alpha_{sm,i+1/2}u_{sm,i+1/2} - \alpha_{sm,i-1/2}u_{sm,i-1/2}}{\Delta x} + \alpha_{g,i}\rho_{g,i}u_{g,i}g_x,\end{aligned} \tag{4.3}$$

$$\frac{\mathrm{d}(\alpha_{s,l} \rho_{s,l})_i}{\mathrm{d}t} = -\frac{\dot{m}_{sl,i+1/2} - \dot{m}_{sl,i-1/2}}{\Delta x}, \tag{4.4}$$

$$\begin{aligned}\frac{\mathrm{d}(\alpha_{s,l} \rho_{s,l} u_{s,l})_i}{\mathrm{d}t} = &-\frac{\dot{m}_{sl,i+1/2}u_{sl,i+1/2} + p_{sl,tot,i+1/2} - \dot{m}_{sl,i-1/2}u_{sl,i-1/2} - p_{sl,tot,i-1/2}}{\Delta x} \\ &-\alpha_{s,l}\frac{p_{g,i+1/2} - p_{g,i-1/2}}{\Delta x} + \alpha_{sl,i}\rho_{sl,i}g_x,\end{aligned} \tag{4.5}$$

$$\frac{\mathrm{d}(\alpha_{s,l} \rho_{s,l} E_{s,l})_i}{\mathrm{d}t} = -\frac{\dot{m}_{sl,i+1/2}E_{sl,i+1/2} - \dot{m}_{sl,i-1/2}E_{sl,i-1/2}}{\Delta x} - p_{s,l}\frac{u_{s,i+1/2} - u_{s,i-1/2}}{\Delta x}, \tag{4.6}$$

$$\frac{\mathrm{d}(\alpha_{s,l} \rho_{s,l} e_{s,l})_i}{\mathrm{d}t} = -\frac{\dot{m}_{sl,i+1/2}e_{sl,i+1/2} - \dot{m}_{sl,i-1/2}e_{sl,i-1/2}}{\Delta x}, \tag{4.7}$$

where the primitive variables for the gas phase, ρ_g, u_g, p_g, and H_g at the cell edges are calculated from a HLLC Riemann solver, and the variables, u_{sl}, e_{sl}, E_{sl}, $\dot{m}_{sl}$, α_{sl} and α_g are derived using the AUSM scheme.

4.2.2 HLLC Riemann Solver for the Gas Phase

The solution for the gas phase at computational cell edge $i + 1/2$ is calculated by a modified HLLC Riemann solver, where the primitive variables are defined as,

$$P_{g+\frac{1}{2}} = \begin{cases} P^L_{g,i+\frac{1}{2}} & \text{if } 0 \leq S^L \\ P^{L*}_g & \text{if } S^L \leq 0 \leq S^* \\ P^{R*}_g & \text{if } S^* \leq 0 \leq S^R \\ P^R_{g,i+\frac{1}{2}} & \text{if } S^R \leq 0, \end{cases} \tag{4.8}$$

where

$$P^K_g = \begin{bmatrix} \rho^K_g \\ \boldsymbol{u}^K_g \\ p^K_g \\ E^K_g \end{bmatrix}, P^{K*}_g = \begin{bmatrix} \rho^{K*}_g \\ S^* \\ p_* \\ E^{K*}_g \end{bmatrix}. \tag{4.9}$$

The superscript K refers to either L or R state of the variable. The quantities ρ^{K*}_g and E^{K*}_g are defined as,

$$\rho^{K*}_g = \rho^K_g \frac{S^K - u^K_g}{S^K - S^*}, \tag{4.10}$$

and

$$E^{K*}_g = E^K_g + \frac{p^* S^* - p^K_g u^K_g}{\rho^K_g (S^K - u^K_g)}. \tag{4.11}$$

The velocity of the gas-phase contact surface (S^*) and the pressure at the contact surface (p^*) are

$$S^* = \frac{p^R_g - p^L_g + \rho^L_g u^L_g (S^L - u^L_g) - \rho^R_g u^R_g (S^R - u^R_g)}{\rho^L_g (S^L - u^L_g) - \rho^R_g (S^R - u^R_g)}, \tag{4.12}$$

and

$$p^* = p^L_g + \rho^L_g (S^L - u^L_g)(S^* - u^L_g). \tag{4.13}$$

The quantities S^L and S^R are the left and right wave speeds and are calculated using the Roe-averaged approach [58]. The primitive variable vectors $P^L_{g,i+1/2}$ and $P^R_{g,i+1/2}$

needed for the HLLC are interpolated with a 3rd-order MUSCL scheme with an adaptive total variation diminishing (TVD) slope limiter (minmod) to reduce small oscillations near discontinuities.

4.2.3 Advection Upstream Splitting Method (AUSM) for the Particle Phase

The AUSM$^+$ -up flux by Liou [59] for any particle phase within a polydispersed granular system is,

$$F_{s,i+1/2} = p_{i+1/2} + \dot{m}_{s,i+1/2} \begin{cases} \Psi^L & \text{if } \dot{m}_{s,i+1/2} \geq 0 \\ \Psi^R & \text{if } \dot{m}_{s,i+1/2} < 0 \end{cases} \tag{4.14}$$

where $p_{i+1/2} = (0, p_{s,tot,i+1/2}, 0, 0)^T$, and $\Psi = (1, u_s, E_s, e_s)^T$. The mass flux at the cell interface ($\dot{m}_{s,i+1/2}$) is defined by

$$\dot{m}_{s,i+1/2} = \mathcal{F} + (c_{1/2} + \epsilon) M_{1/2} \begin{cases} \alpha_s^L \rho_s^L & \text{if } M_{1/2} \geq 0 \\ \alpha_s^R \rho_s^R & \text{if } M_{1/2} < 0 \end{cases} \tag{4.15}$$

where ϵ is a small number added to avoid dividing by zero during the calculation. $\mathcal{F}$ is an extra dissipation term developed to stabilize calculations that approach the packing limit, where the compaction wave speed becomes very sensitive to small particle volume fraction fluctuations [1]. $M_{1/2}$ is the Mach number for the particle phase based on the compaction wave speed at the cell edge [1]. The compaction wave speed at the cell edge is

$$c_{1/2} = \sqrt{\frac{\alpha_s^L \rho_s^L (c_s^L)^2 + \alpha_s^R \rho_s^R (c_s^R)^2}{\alpha_s^L \rho_S^L + \alpha_s^R \rho_s^R}} + \epsilon \tag{4.16}$$

Note that the compaction wave speed (c_s) used here is a value shared by all solid phases ($c_{s,mix}$).

The split Mach number, $M_{1/2}$, for the granular phase is computed by

$$M_{1/2} = \mathcal{M}_4^+(M^L) + \mathcal{M}_4^-(M^R) - 2\frac{K_p}{f_a}\max(1 - \sigma \bar{M}^2, 0)\frac{p_{s,tot}^R - p_{s,tot}^L}{(\alpha_s^L \rho_s^L + \alpha_s^R \rho_s^R + \epsilon) c_{1/2}^2}, \tag{4.17}$$

and the split pressure is

$$p_{s,tot,i+1/2} = -K_u f_a (c_{1/2} - \epsilon)\mathcal{P}_5^+(M^L)\mathcal{P}_5^-(M^R)(\alpha_s^L \rho_s^L + \alpha_s^R \rho_s^r)(u_s^R - u_s^L) + \mathcal{P}_5^+(M^L)p_{s,tot}^L + \mathcal{P}_5^-(M^R)p_{s,tot}^R, \tag{4.18}$$

where

$$f_a = 1, \quad M^L = \frac{u_s^L}{c_{1/2}}, \quad M^R = \frac{u_s^R}{c_{1/2}}, \quad \bar{M}^2 = \frac{(u_s^L)^2 + (u_s^R)^2}{2c_{1/2}^2}. \tag{4.19}$$

The pressure and Mach number splitting polynomials are

$$\mathcal{M}_1^{\pm}(M) = \frac{1}{2}(M \pm |M|), \tag{4.20}$$

$$\mathcal{M}_2^{\pm}(M) = \pm\frac{1}{4}(M \pm 1)^2, \tag{4.21}$$

$$\mathcal{M}_4^{\pm}(M) = \begin{cases} \mathcal{M}_1^{\pm}(M) & \text{if } |M| \geq 1 \\ \mathcal{M}_2^{\pm}[1 \mp 16\beta\mathcal{M}_2^{\mp}(M)] & \text{if } |M| < 1, \end{cases} \tag{4.22}$$

$$\mathcal{P}_5^{\pm}(M) = \begin{cases} \frac{\mathcal{M}_1^{\pm}(M)}{M} & \text{if } |M| \geq 1 \\ \mathcal{M}_2^{\pm}(M)[(\pm 2 - M) \mp 16\xi M\mathcal{M}_2^{\mp}(M)] & \text{if } |M| < 1, \end{cases} \tag{4.23}$$

where $\beta = 0.125$ and $\xi = \frac{3}{16}(-4 + 5f_a^2)$.

The full description for the modified AUSM scheme is presented in Houim et. al [1]. Similar to the HLLC flux for the gas phase, the primitive variables for the granular phases are interpolated with a 3rd-order MUSCL scheme with a TVD slope limiter. The above equations are valid for any particle type within a polydispersed system. Including an additional particle bin will introduce a new set of the AUSM fluxes for the additional type of particles. Fluxes and primitive variables for different particle bins are solved individually.

4.3 Integration of the Source Terms

Removing all the hyperbolic terms from the governing equations (3.2)∼(3.4), and (3.6)∼(3.9), the equations containing the remaining source terms are

$$\frac{\partial \alpha_g \rho_g \boldsymbol{v}_g}{\partial t} = \sum_{m=1}^{M} \boldsymbol{f}_{\text{Drag,gm}}, \tag{4.24}$$

$$\frac{\partial \alpha_g \rho_g E_g}{\partial t} = \sum_{m=1}^{M} \{(\boldsymbol{f}_{\text{Drag,gm}} + \boldsymbol{f}_{\text{Lift,gm}}) \cdot \boldsymbol{v}_g - q_{conv,gm} + \phi_{visc,gm} - \phi_{slip,gm}\}. \tag{4.25}$$

$$\frac{\partial \alpha_{s,l} \rho_{s,l} \boldsymbol{v}_{s,l}}{\partial t} = -\boldsymbol{f}_{\text{Drag,gl}} - \sum_{\substack{m=1 \\ m \neq l}}^{M} \{\boldsymbol{f}_{\text{Drag,lm}}\}, \tag{4.26}$$

$$\frac{\partial \alpha_{s,l} \rho_s E_{s,l}}{\partial t} = -\dot{\gamma}_l - \phi_{visc_g l} + \phi_{slip_g l}, \tag{4.27}$$

$$\frac{\partial \alpha_{s,l} \rho_{s,l} e_{s,l}}{\partial t} = q_{conv,gl} + \dot{\gamma}_l. \tag{4.28}$$

Here, we divide the source terms to two categories: (1) drag and convective heat transfer ($\mathcal{S}_{qD}^{\Delta t}$), and (2) energy transfer due to viscous effect ($\phi_{visc_g l}$), velocity slip ($\phi_{slip_g l}$), and inelastic particle collisions ($\dot{\gamma}$) ($\mathcal{S}_{\Theta}^{\Delta t}$). The two types of source terms are then integrated using a Strang-splitting method [1]

$$\mathcal{S}^{2\Delta t} = \mathcal{S}_{qD}^{\Delta t}(\mathcal{S}_{\Theta}^{\Delta t}(\mathcal{S}_{qD}(\mathcal{S}_{\Theta}^{\Delta t}(U^H)))). \tag{4.29}$$

Again, the integration procedures discussed in the following sections are similar to what was shown in Houim and Oran [1], but now extended from a two-fluid system to a multifluid system.

4.3.1 Integration of $\mathcal{S}_{qD}^{\Delta t}$

Recall that the correlations for the drag between gas and the m^{th} particle phase, the drag between the m^{th} and l^{th} particle phase, and the heat transfer between gas and

the m^{th} particle phase are:

$$\boldsymbol{f}_{\text{Drag},mg} = K_{sg}(\boldsymbol{v}_{s,m} - \boldsymbol{v}_g), \tag{4.30}$$

$$\boldsymbol{f}_{\text{Drag,lm}} = K_{lm}(\boldsymbol{v}_{s,l} - \boldsymbol{v}_{s,m}), \tag{4.31}$$

and

$$q_{\text{conv}_{gm}} = h_{mg}(T_g - T_{s,m}). \tag{4.32}$$

Assuming all the coefficients in the above equations to be frozen (state 0) during one integration step, analytical solutions of the drag and heat transfer terms can be found by integrating the differential equations (Eqn. (4.24) $\sim$ (4.26) and (4.28)) from state 0 with a time step Δt [54].

The change in momentum from drag between gas phase and particle phase m, ΔM_{gm} is,

$$\Delta M_{gm} = \frac{\boldsymbol{v}_g^0 - \boldsymbol{v}_{s,m}^0}{\xi D}[\frac{1}{K_{mg}\xi D\Delta t} - 1], \tag{4.33}$$

where

$$\xi D = \frac{1}{\alpha_g \rho_g} + \frac{1}{\alpha_{s,m}\rho_{s,m}}. \tag{4.34}$$

The change in momentum from drag between particle phase l and particle phase m, ΔM_{lm}, is

$$\Delta M_{lm} = \frac{\boldsymbol{v}_l^0 - \boldsymbol{v}_m^0}{\xi D}[\frac{1}{K_{lm}\xi D\Delta t} - 1], \tag{4.35}$$

where

$$\xi D = \frac{1}{\alpha_l \rho_l} + \frac{1}{\alpha_m \rho_m}. \tag{4.36}$$

The change in internal energy from convection between gas and particle phase m is

$$\Delta e_{gm} = \frac{T_g^0 - T_{s,m}^0}{\xi e}[e^{-h_{mg}\xi e\Delta t} - 1], \tag{4.37}$$

where

$$\xi e = \frac{1}{\alpha_g \rho_g C_{v,g}^0} + \frac{1}{\alpha_m \rho_m C_{v,m}^0} \tag{4.38}$$

As a result, the momentum and energy state for the gas and particle phases at the new time step Δt is

$$(\alpha_g \rho_g \boldsymbol{v}_g)^{\Delta t} = (\alpha_g \rho_g \boldsymbol{v}_g)^0 + \sum_{m=1}^{M} \Delta M_{gm} \tag{4.39}$$

$$(\alpha_{s,m} \rho_{s,m} \boldsymbol{v}_{s,m})^{\Delta t} = (\alpha_{s,m} \rho_{s,m} \boldsymbol{v}_{s,m})^0 - \Delta M_{gm} + \sum_{l=1, l\neq m}^{M} \Delta M_{lm} \tag{4.40}$$

$$(\alpha_g \rho_g E_g)^{\Delta t} = (\alpha_g \rho_g E_g)^0 + \sum_{m=1}^{M} \left(\Delta e_{gm} - \frac{(\alpha_{s,m}\rho_{s,m})^0}{2} [\boldsymbol{v}_{s,m}^{\Delta t} \cdot v_{s,m}^{\Delta t} - \boldsymbol{v}_{s,m}^0 \cdot \boldsymbol{v}_{s,m}^0] \right) \tag{4.41}$$

$$(\alpha_{s,m} \rho_{s,m} e_{s,m})^{\Delta t} = (\alpha_{s,m} \rho_{s,m} e_{s,m})^0 - \Delta e_{gm} \tag{4.42}$$

4.3.2 Integration of $\mathcal{S}_\Theta^{\Delta t}$

Similarly, the energy transfer terms including ϕ_{visc_gl}, ϕ_{slip_gl} and $\dot{\gamma}$, can also be integrated analytically. In order to get the final PTE level accounting for all these effects at the new time step, the PTE is calculated with three steps.

First the dissipation of PTE due to viscous damping for particle phase m is

$$\Theta_{s,m}^* = \Theta_{s,m}^0 \exp\left[\frac{-sK_{mg}\Delta t}{\alpha_{s,m}\rho s, m} \right] \tag{4.43}$$

Second, the production of PTE from velocity slip is integrated,

$$\Theta_{s,m}^{**} = \left[\frac{\xi_{slip}}{\alpha_{s,m}\rho_{s,m}\Delta t + (\Theta_{s,m}^*)^{3/2}} \right]^{2/3}, \tag{4.44}$$

where

$$\xi_{slip} = \frac{81\alpha_{s,m}\mu_g^2}{g_{0,mm} d_{s,m}^3 \rho_{s,m}\sqrt{\pi}} \frac{|\boldsymbol{v}_g^0 - \boldsymbol{v}_{s,m}^0|^2}{K_{mg}\xi D\Delta t + 1}. \tag{4.45}$$

Note the radial distribution used here $g_{0,mm}$ describes the probability of particle interactions within particle phase m.

Finally, the dissipation of PTE due to inelastic granular collision is

$$\Theta_{s,m}^{\Delta t} = \Theta_{s,m}^{**} \frac{9(\alpha_{s,m}\rho_{s,m})^2}{[3\alpha_{s,m}\rho_{s,m} + \Delta t \xi_\gamma \sqrt{\Theta_{s,m}^{**}}]^2} \tag{4.46}$$

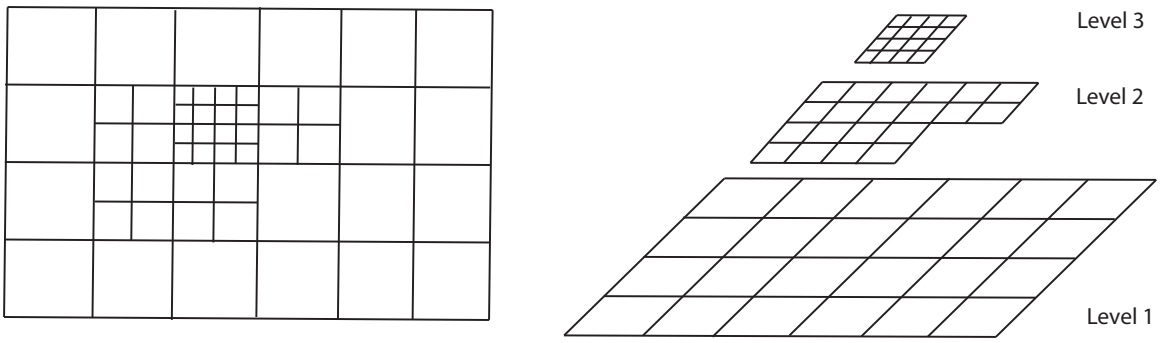

Figure 4.1: A sample three-level AMR grid structure.

where

$$\xi_\gamma = 12(1-e^2)g_{0,mm}\alpha_{s,m}^2\frac{\rho_{s,m}}{d_{s,m}\sqrt{\pi}} \tag{4.47}$$

As a result, the energy for the gas and particle phases at the new time step Δt is

$$(\alpha_{s,m}\rho_{s,m}E_{s,m})^{\Delta t} = \frac{3}{2}(\alpha_{s,m}\rho_{s,m})^0\Theta_{s,m}^{\Delta t} \tag{4.48}$$

$$(\alpha_{s,m}\rho_{s,m}e_{s,m})^{\Delta t} = (\alpha_{s,m}\rho_{s,m}e_{s,m})^0 - \frac{3}{2}(\alpha_{s,m}\rho_{s,m})^0(\Theta_{s,m}^{\Delta t} - \Theta_{s,m}^{**}) \tag{4.49}$$

$$(\alpha_g\rho_gE_g)^{\Delta t} = (\alpha_g\rho_gE_g)^0 - \sum_{m=1}^{M}\left(\frac{3}{2}(\alpha_{s,m}\rho_{s,m})^0(\Theta_{s,m}^{**} - \Theta_{s,m}^0)\right). \tag{4.50}$$

4.4 Adaptive Mesh Refinement

The uniform mesh places fine grid spacing in the entire domain, even in places where nothing is happening. Adaptive mesh refinement, on the other hand, places computational grid points only where they are needed. Codes that employ adaptive mesh refinement (AMR) technique can be around 10 to 100 times faster than codes that use uniform grids.

The concept of AMR was first introduced by Berger and Colella [60] and Berger and Oliger [61]. For simulations with AMR, we start with a base coarse grid, and identify

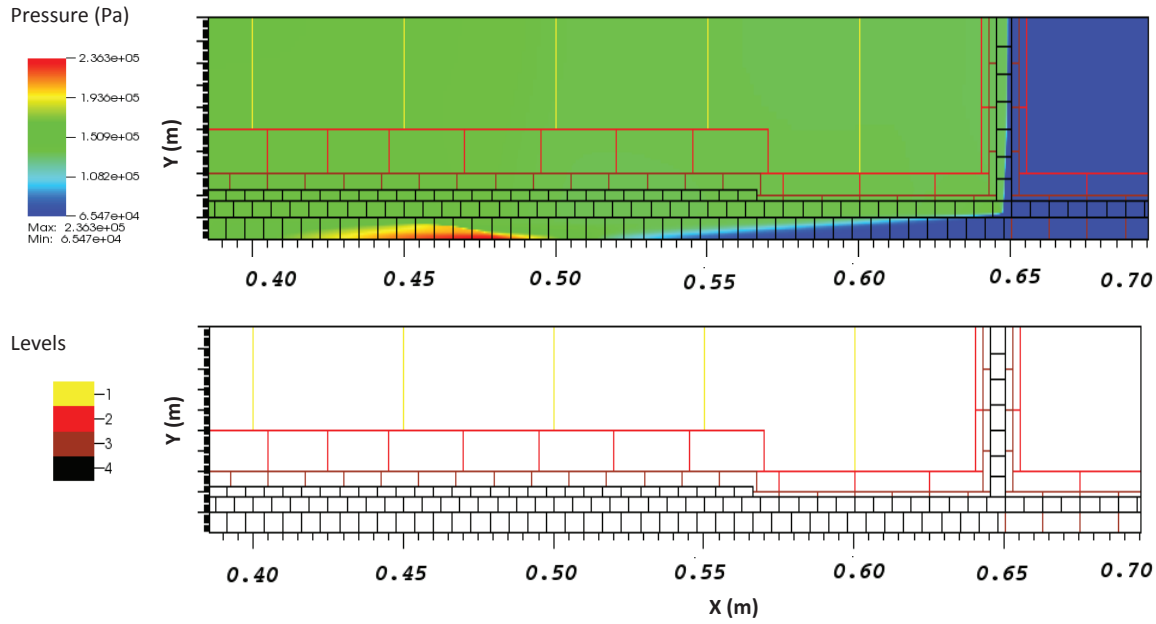

Figure 4.2: AMR structures for a sample case of a shock passing over a dust layer using Boxlib with four levels of refinement.

regions requiring more resolution (finer grid). Then we superimpose the finer grid in these regions, where variables and solutions are calculated for a second time. This process is repeated until the given maximum level of refinement is reached. Fig. 4.1 shows a sample three-level AMR grid structure.

There are a number of available libraries that provides structured AMR, such as PARAMESH [57], BoxLib (or AMReX) [57], AMRClaw [62], and SAMRAI [63]. In this work, Boxlib and PARAMESH will be used. Both of the two libraries handle parallel communications. Paramesh uses a pure-MPI parallelization strategy while Boxlib supports a hybrid MPI/OpenMP approach, which allows us to compute with lower memory requirement and better scaling behavior. Fig. 4.2 shows the AMR structures for a simulation where a shock passes over a dust layer using Boxlib with four levels of refinement. Here, each box represents a small, local, uniform grid with its own grid resolution

determined by

$$\Delta x_{\mathrm{lref}} = \Delta x_{\mathrm{coarse}}/2^{\mathrm{lref}-1}, \tag{4.51}$$

where lref is the local refinement level and $\Delta x_{\mathrm{coarse}}$ is the grid spacing at the coarsest level of refinement. Finer grids are placed close to the moving shock wave and the edge of the dust layer, while the background domain is calculated on coarser grids.

Chapter 5

DUST DISPERSION INDUCED BY SHOCK WAVES

5.1 Introduction and Background

Dust dispersion induced by gas flow is encountered in many aspects of science and engineering. In certain cases, the dispersed dust particles can be a threat to the environment and to human lives. For example, the entrainment of coal particles during a coal mine explosion can result in a more dangerous secondary explosion [7, 8]; the airborne dust particles during a helicopter brownout landing can obscure the pilot's vision [64]; and the migration of the sand dunes in desert regions by the action of wind can accelerate the process of desertification [65].

Dust entrainment in a coal mine explosion is a mode of dust dispersion that involves the interaction of a granular bed and a shock wave generated from an explosion. In this chapter, we focus on the problem of dispersing a layer of dust particles by a moving shock wave, in which the conditions are characteristic of what is found in a coal mine. In this situation, shock waves initiated by an initial explosion produce forces that can lift coal dust as the shock propagates over the dust layer. The dispersed coal dust, if

ignited by the explosion, may lead to a more devastating secondary explosion.

Specifically, we studied the effects of particle size and density in a polydispersed dust layer (i.e., a dust layer containing nonuniform particle sizes and densities) with the proposed Eulerian-Eulerian multifluid granular model [2]. We performed simulations where a shock passes over a single dust layer containing different particle types that were uniformly mixed with each other. In addition, we are interested in the problems where the shock wave passes over multiple dust layers containing either coal or rock particles (stratified layer). These investigations were done to provide a qualitative understanding of the dispersion process of dust layers and the effect of particle size, particle density, and dust-layer thickness on the results. Identifying these controlling parameters of the flow will provide important information that can be used to determine how to prevent and mitigate a dust explosion in underground coal mines. To the best of our knowledge, this is the first numerical work discussing the dispersion of a polydispersed dust layer behind a propagating shock wave.

5.1.1 Shock Interaction With Dust Layers

In the past, laboratory experiments and computations have been carried out to quantify and explain the lifting mechanism of a dust layer by a shock wave. Gerrard [66] performed the first experimental work on dust lifting behind a moving shock. He concluded that particles were lifted due to the reflection of pressure waves and shock waves from the bottom of the channel. It was also found that there was a delay between the shock front and the beginning of the dust lifting. Borisov *et al.* [67] concluded through similar experiments that dust was lifted by surface instabilities that developed due to the compression and reflected compression waves, which bounced back and forth between the chamber wall and the dust surface. These conclusions were later criticized by Fletcher [7] based on both experimental and numerical investigations. Fletcher believed

that dust was lifted due to instabilities induced by the rapid flow behind the shock wave instead of the reflecting compression wave.

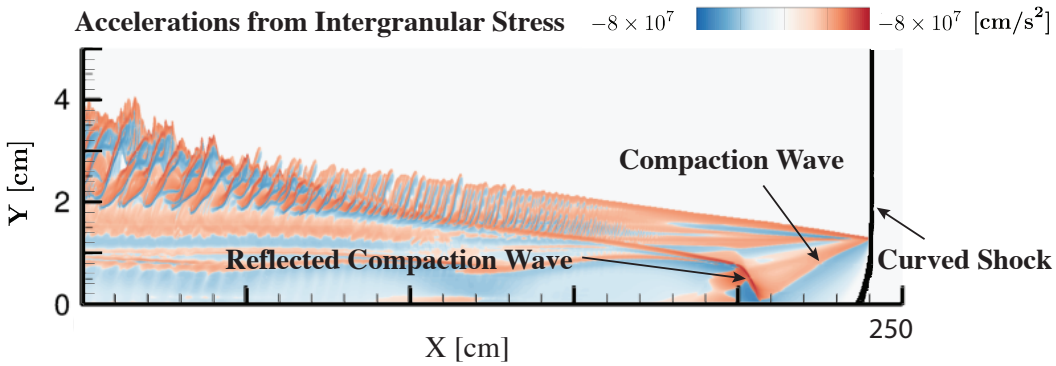

Figure 5.1: Structures behind a moving shock wave during the dispersing process.

More recently, Houim *et al.* [68] and Ugarte *et al.* [69] explained the mechanism of dust lifting with numerical simulations. According to their results, the gas shock curved and degenerated into a compression wave as it entered the dust layer. The gas compression wave compacted the particles in the layer and evolved into a granular compaction wave through particle collisional and frictional effects. The granular compaction wave reflected between the chamber walls and the surface of the dust layer back and forth and formed a periodic structure. The reflected wave propagated upwards and interacted with the surface dust layer, producing acoustic waves, which could enhance the flow oscillation. The structures behind the shock wave are illustrated in Fig. 5.1. Ugarte *et al.* [69] further identified the governing forces responsible for dust dispersion. They found that the dust dispersion was initiated by intergranular forces between the particles. Later, the dispersion was produced by lift and intergranular forces, and opposed by drag.

5.1.2 Effect of Particle Size and Density

The most important parameters in the dispersion process is the size and density of the dispersing particles. Both experimental and numerical analyses have shown that

particles with different sizes and densities can be dispersed into different heights. These studies, however, lead to contradictory conclusions, some of which have been pointed out by Ugarte et al. [69].

For example, experiments performed by Suzuki and Adachi [70] and Chowdhury *et al.* [71] showed that the dust-lifting height increases as the particle size decreases. In addition, they showed a delay between the passage of the shock and dust lifting. Similarly, the numerical studies by Zhu et al. [72] showed that particle density had little effect on the lifting, but particle size has a significant effect. Finer dust is lifted more efficiently by a shock wave [72].

As an apparent contradiction, the experimental results done by Hwang [8] showed that particles with a diameter of 200 μm were lifted twice as high as particles with a 5 μm diameter, which indicates that larger particles are lifted higher than smaller particles. The delay in particle lifting increased as the particle size increased. Similarly, the simulations by Boyi et al. [73] suggested that, due to the effect of the lift force, the height of dispersed dust increased with the particle size. The same conclusion was also make by Ugarte et al. [69] with numerical simulations.

These apparently contradictory observations could result from the inconsistency in time and length scales or controlled variables among different studies. For example, Ugarte et al. [69] explained that their simulations differ from Suzuki's experiments because the results were evaluated at different distances (length) and times after the shock passed. In Suzuki's experiments, the observations were made within the 40-cm range of shock propagation, and delay in particle lifting was observed directly behind the shock. The simulations done by Ugarte et al. [69] were performed after the shock passed 300 cm down the channel, and the lifting delay process played a much less significant role in dust lifting. In addition, Chowdhury [74] noted that the particles of different sizes used in Suzuki and Adachi [70]'s experiments were different materials with approximate

the same density but different morphology [74]. The interactions among particles with different physical properties could bring uncertainties to the results obtained by Suzuki and Adachi [70].

5.1.3 Particle Segregation

All of the studies summarized above assumed a single particle type within the dust layer. In actual underground coal mines, however, rock dust is usually applied for inerting and suppressing of coal-dust dispersion and ignition. In fact, it is required by MSHA (Mine Safety and Health Administration) that the total incombustible content (TIC) is at least 80% when mixed with coal to prevent dust explosions [9]. Therefore, the dust layer in coal mines consists of both rock and coal particles, which are usually different in size and density, and thus form a polydispersed granular system. Ideally, the rock dust, which is applied regularly to the dust surfaces during the mining operation, would suppress the dispersion of the coal dust underneath. In addition, a coal-rock mixture would be formed in the dispersed gas due to disturbances. The rock dust, then would act as a thermal inhibitor and prevent flame propagation [10]. In actual situations, a propagating shock wave could separate the rock and coal particles according to their different sizes and densities, and destroy the well-mixed rock-coal mixture. The ignition of the separated coal dust could still lead to a secondary explosion. Therefore, studying the dispersion of a dust layer containing different particle types and their segregation phenomenon is important to ensure safety in coal mines. Specifically, we would like to answer the following question: *How do particle size and density affect dust dispersion and particle segregation?*

Very limited experimental or numerical studies have focused on dust lifting in a polydispersed system. Chowdhury *et al.* [71] made the first attempt to measure the effect of size polydispersity in a dust layer behind a moving shock wave. Their experimental

Table 5.1: Forces acting on particle type l

(1) Archimedes Force	$-\alpha_{s,l}\nabla p_g$
(2) Intergranular Stress	$-\nabla p_{s,l} - \nabla p_{fric,l}$
(3) Drag	$K_{lg}(\boldsymbol{v_g} - \boldsymbol{v_{s,l}})$
(4) Lift	$C_l\alpha_{s,l}\rho_g(\boldsymbol{v_g} - \boldsymbol{v_{s,l}}) \times (\nabla \times \boldsymbol{v_g})$
(5) Particle-hindrance force	$\sum_{m=1,m\neq l}^{M} K_{s,lm}(\boldsymbol{v_{s,l}} - \boldsymbol{v_{s,m}})$
(6) Gravitational	$\alpha_{s,l}\rho_{s,l}\boldsymbol{g}$

findings concluded that dust entrainment decreases as the particle size increases, and a sample containing a wider range of size distribution (i.e., high polydipsersity) lifts higher than a sample with the same mean size, but lower polydipsersity [71]. To the best of our knowledge, no numerical work has been reported to study the effect of particle size in a polydispersed dust layer.

5.1.4 Evaluation of forces

Now recall Table 3.1 from Section 3.4.3, where the six forces acting on each type of particles are listed. Evaluating these forces helps to explain how the particle size and density affect dust dispersion. The lift and drag forces result from the velocity difference between the particles and the gas. The Archimedes force is due to the gas-phase pressure pushing on the particles. The intergranular stress corresponds to the collisional and frictional effect of the particles. The particle-hindrance force is a drag-like force between the two particle types. Gravity is not important in the time scale of the simulations, so it is exempted from the discussion. Now, we only focus on the equations of forces that are related to particle size (d_s) and density (ρ_s).

The collisional part of the intergranular stress (p_s) used in expression (2) in Table 5.1 depends on the particle density. A greater particle density results in a larger

intergranular stress ($\nabla p_s \propto \rho_s$, see Eq. (3.22)).

The momentum exchange coefficient between gas the l^{th} particle phase (K_{lg}) used in expression (3) in Table 5.1 for the drag force is inversely proportional to the particle diameter. In addition, it is also proportional to the the drag coefficient (C_d, see Eq. (3.41)), which is inversely related to the relative velocity and the particle diameter. In other words, a larger particle diameter results in a smaller drag force.

The solid-solid exchange coefficient ($K_{s,lm}$) between the l^{th} and m^{th} particle phases used in expression (5) in Table 5.1 for the particle-hindrance force depends on the particle size and density for both both particle phases. Similar to the gas-phase drag force, it accelerates slower particles while decelerating faster particles.

The expressions for the lift force, Archimedes force, and gravity are independent of the particle size and density. Nevertheless, all governing forces are coupled with each other, and so they may also be affected by particle size and density. For example, the lift force (expression (4) in Table 5.1), which produces positive acceleration for most of the dispersed dust [69], is modelled by the Magnus force. In a two-dimensional simulation, the lifting force along vertical direction is proportional to the velocity difference between the particle phase and gas phase along horizontal direction,

$$f_{Lift,y} = C_l \alpha_s \rho_g (u_s - u_g)(\frac{\partial v_g}{\partial x} - \frac{\partial u_g}{\partial y}). \tag{5.1}$$

Later, we will show that a greater particle size leads to a larger $|u_s - u_g|$ value, and according to Eq. (5.1), this will results in a greater lifting force.

5.2 RESULTS: One-Dimensional

Here, one-dimensional tests of a shock wave interacting with a cloud of particle mixture containing two or more types of particles are presented to show how different types of particles behave with the interaction to a shock wave.

5.2.1 Physical Model

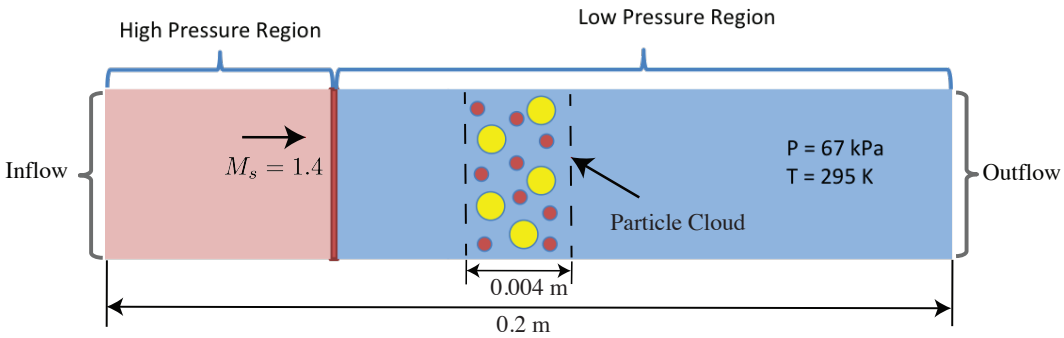

Figure 5.2: Initial conditions for a one-dimensional test of a shock moving through a particle cloud containing two uniformly mixed particle types.

The initial setup for the base case is illustrated in Fig. 5.2. A Mach-1.4 shock driven by the high-pressure gas is moving to the right and passes through a particle mixture. The right section (blue) is the low-pressure region and is 67 kPa and 295 K. (The value of 67 kPa was chosen for consistency with the work of Ugarte et al. [69].) The left section (red) represents the post-shock condition. The particle cloud consists of two different types of particles. This test models a scenario in which a shock wave from an explosion interacts with a dilute dispersed dust clouds containing coal and inert rock particles. The initial volume fraction of each type of particle is 0.026% (based on an explosive coal-air burning condition).

Table 5.2: Input conditions of particle size and density

		Diameter (d_s) [μm]	Density (ρ_s) [kg/m^3]
Case I	Particle I	80	1300
	Particle II	10	1300
Case II	Particle I	10	1300
	Particle II	10	2700

5.2.2 Two Particle Bins

Here, two particle types are considered (same setup as in Fig. 5.2). Separate simulations were used to study the effects of varying particle size and density. The input parameters for the particle types are summarized in table 5.2. The sizes and densities selected are within the range for coal- and rock-dust particles.

5.2.2.1 Effect of Particle Size

The profiles in Fig. 5.3 show how the system evolves when the two particle densities are the same, but their sizes are different (Case I). The vertical dashed lines in Fig. 5.3(a) indicate the location of the gas shock. As the shock wave moves through the particle cloud, there is a small peak in the concentration of the smaller particles (See Fig. 5.3 at 17 μs), indicating that the smaller particles react faster to the propagating shock wave. In time, the different particle types are separated.

The velocity profile in Fig. 5.3(b) shows that the particles inside each of the separated clouds stays roughly the same, and this velocity increases with time. Smaller particles propagate with a higher velocity than larger particles through drag and other aerodynamic effects. The velocity differences cause the uniformly mixed particle cloud to segregate into two different clouds according to the particle size. At 100 μs, a separation between the two particle types is already apparent. At 200 μs, the two particle

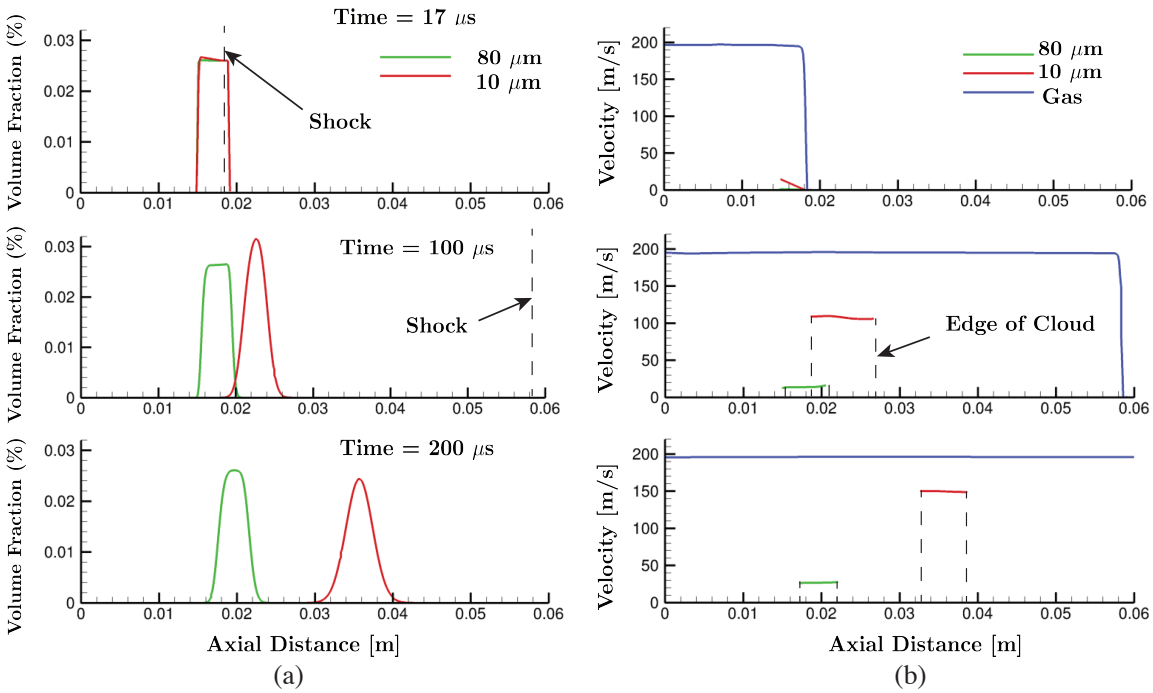

Figure 5.3: Computed (a) volume fractions for the two particle types (d_{s1}=80 μm, d_{s2} =10 μm) and (b) gas and particle velocities at 17 μs, 100 μs, and 200 μs. The edge of the particle cloud is defined by a volume fraction of 5×10^{-5}.

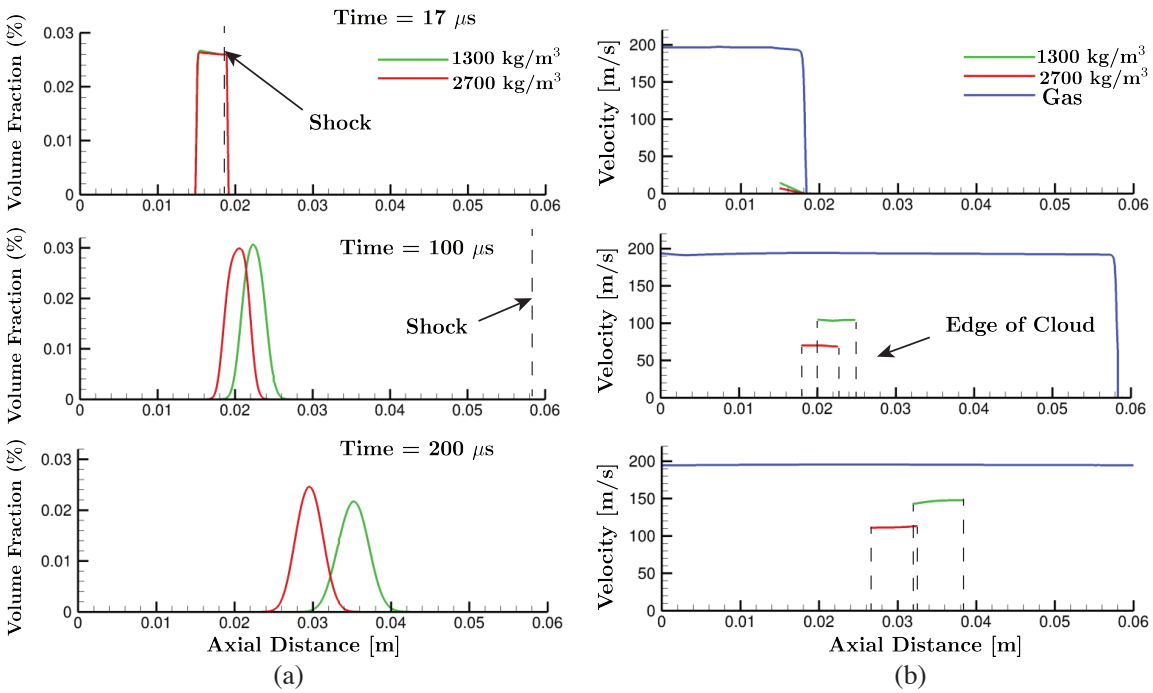

Figure 5.4: Computed (a) volume fractions for the two particle types (ρ_{s1}=1300 kg/m^3, ρ_{s2} =2700 kg/m^3) and (b) gas and particle velocities at 17 μs, 100 μs, and 200 μs. The edge of the particle cloud is defined by a volume fraction of 5×10^{-5}. Dashed lines indicate the locations of the gas shock and the edge of the dust clouds.

types are completely separated.

5.2.2.2 Effect of Particle Density

Figure 5.4 shows how the system evolves when the two particle sizes are the same, but their densities are different (Case II). Similarly, the two particle clouds separate into different regions according to different densities. The velocity profiles show that heavier particles are accelerated more slowly than the lighter particles. The two types of particles propagate with different velocities and the separation process increases with time. This separation is slower than that for the previous case (same density but different sizes). At 200 μs, the two types of particles are not completely separated.

With the two simulations shown above, we find that particles with different size or density can separate from each other even when they were initially uniformed mixed with each other. Modeling the dust particles with only one particle bin (i.e., uniform size and density) fails to capture the separation process. The reason why the separation process occurs between different particle types will be discussed later.

5.2.3 Six Particle Bins

Table 5.3: Rock-dust Size Distribution.

Size Range [μm]	Averaged Diameter ($d_{s,i}$)[μm]	Volume Fraction ($\alpha_{s,i}$)[%]
0-5.61	1.685	0.00511
5.61-15.65	8.931	0.00546
15.65-52.62	26.201	0.00510
52.62-121.83	81.633	0.00555
121.83-339.90	171.239	0.00478

In a coal mine, both coal and rock particles are present in a range of sizes. Here, however, we assume a uniform diameter for the coal particles while dividing the rock dust into five particle bins, where each bin is characterized by a different particle size, but they all have the same density. The division is based on the OMSHR's reference size distribution chart [75]. The five types of rock-dust particles have approximately the same volume fraction and the overall volume fraction for the rock particles is 0.026%. The diameters and volume fractions for the five types of rock-dust particles are listed in Table 5.3. The coal dust has a density of 1300 kg/m^3 and a diameter of 10 μm. All rock-dust particles have a density of 2700 kg/m^3. The initial volume fraction for the coal-dust particles is set to be 0.026%.

The computed results are shown in Fig. 5.5. Similar to the results with two particle bins, the uniformly mixed cloud separates into different dust clouds. The particles with

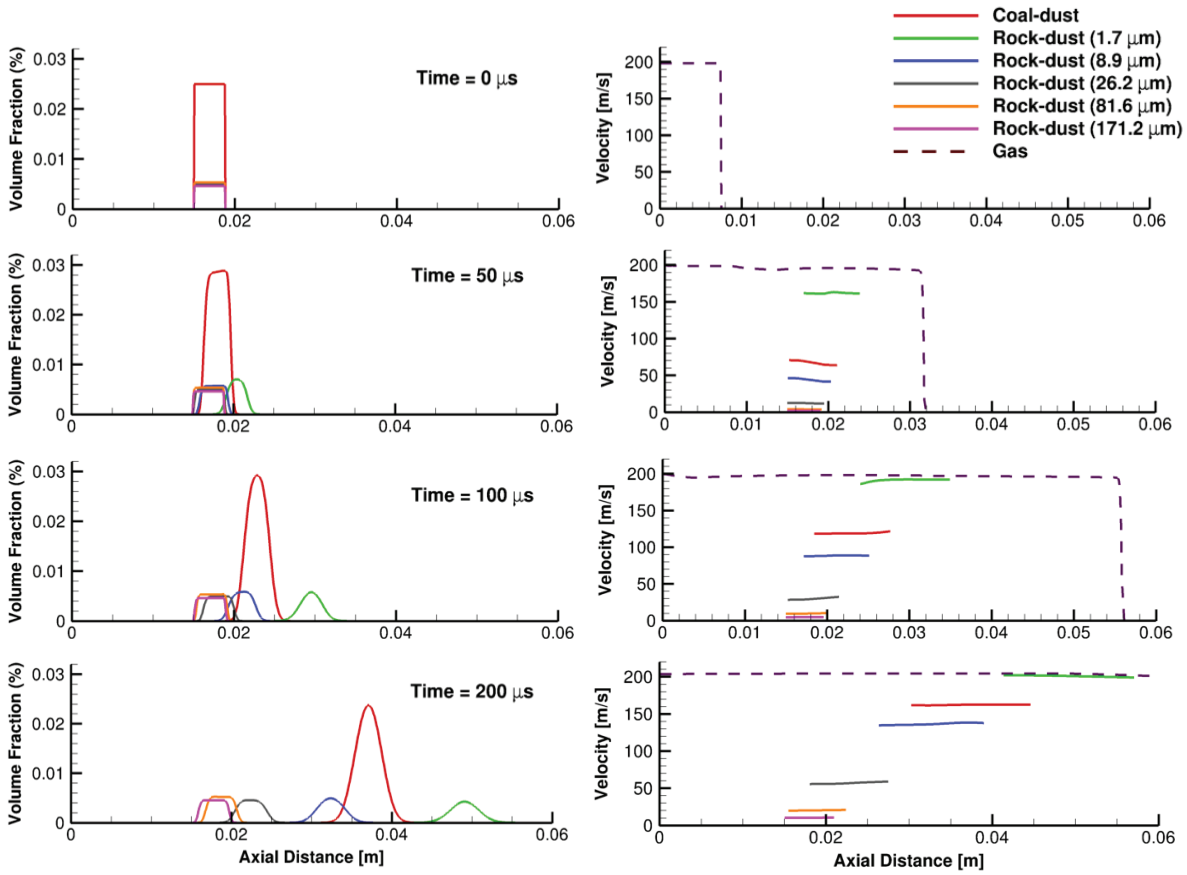

(a) Particle Volume Fraction

(b) Velocity

Figure 5.5: Computed (a) coal- and rock-dust volume fraction and (b) gas and particle velocities at 0 μs, 50 μs, 100 μs, and 200 μs. The edge of the cloud in (b) is defined by a volume fraction of 10^{-9}.

a smaller size and density are accelerated faster by the post-shock gas condition than particles with a larger size and density. The 1.7-μm rock-dust (green) has the highest velocity (approaching the gas-phase velocity) and is completely separated from all the other particle bins by 200 μs. The 171.2-μm rock-dust travels with the slowest velocity and lags behind all other particle types. The velocity of the coal particles (red) is lower than the 1.7-μm rock particles, but larger than the other rock-dust particles.

5.2.4 Dense Particle Curtain

Here we consider an extreme numerical test problem with a dense particle curtain ($\alpha_{s,tot} = 0.4$) containing multiple particle types to study the segregation phenomenon. The particles are approximated as a mixture of 10 μm coal particles, and 50 and 120 μm-diameter rock-dust particles. The density of coal and rock dust is 1300 kg/m^3 and 2700 kg/m^3, respectively. High-pressure gas at 100 atm is placed on the left side of the particle curtain. This is an extreme condition that is designed to stress the model and numerical solution algorithm.

At t = 0 the high-pressure gas is released, which, in turn, pushes on the left side of the particle curtain. This compacts and drives the particle curtain to the right. This process is similar to how high-pressure gas behind a propagating shock wave initially compacts the dust layer.

The computed particle volume fractions at 0, 200, and 400 μs are shown in Fig. 5.6. Here, unlike the dilute particle cloud shown in Section 5.2.2 and 5.2.3, the particle mixture does not segregate into different particle clouds. The volume fraction profiles of each particle type are, for the most part, similar. Nevertheless, there are some slight differences. The compaction of the coal particles is slightly greater than the rock dust particles at 200 μs. There also is some separation of the particles at the tail of the curtain where the volume becomes dilute. (See Fig. 5.6 at $x < 0.06$ m.)

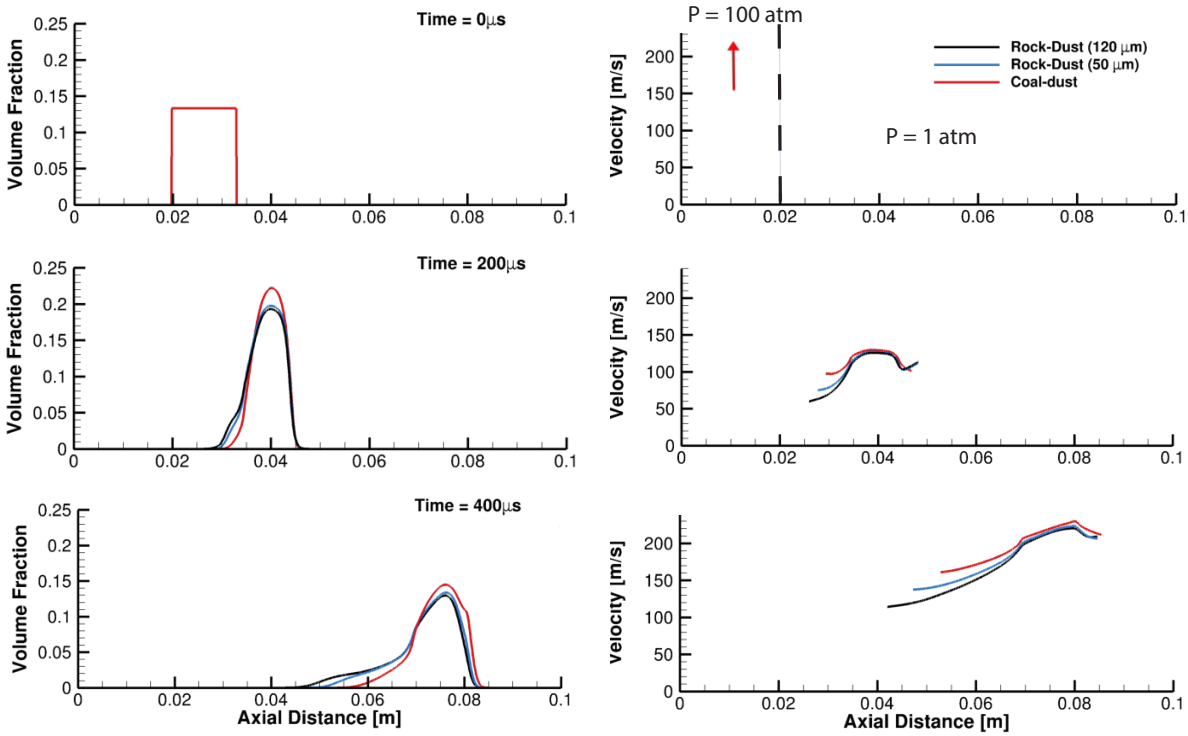

(a) Particle Volume Fraction

(b) Particle Velocity

Figure 5.6: Computed (a) coal- and rock-dust volume fraction and (b) particle velocity at 0 μs, 200 μs, and 400 μs. The edge of the cloud in (b) is defined by a volume fraction of 10^{-9}. The initial volume fraction of the dust is 40%. The particles are accelerated by high-pressure gas at 100 atm.

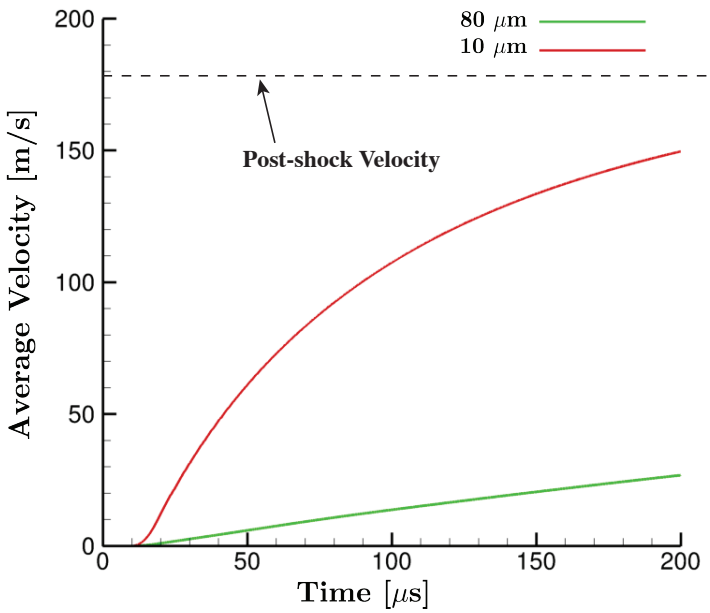

Figure 5.7: Average velocities for both types of particles in Case I (d_s= 10 μm, 80 μm; $\rho_{s1} = \rho_{s2}$=1300 kg/m^3) as a function of time in the post-shock flow.

Figure 5.6(b) shows the velocity of the particles at 0, 200, and 400 μs. The velocity of coal-dust is slightly greater the rock-dust. Nevertheless, the particles generally propagate together at the same velocity. The velocity of the particles differs on the tail of the particle curtain and the particles in this region do not travel in a group.

5.2.5 Discussions

5.2.5.1 Effect of Particle Size and Density

In Case I, where the two types of particles have the same density but different sizes, larger particles are accelerated more slowly than smaller particles. Fig. 5.7 shows the average velocity of the two types of particles and the post-shock gas velocity as a function of time. At 200 μs, the smaller particles have a velocity of 150 m/s, while the larger particles have a velocity of only 30 m/s. From an evaluation of the forces in Table 5.1, the dominant force acting on the particles is the drag force, which is inversely

proportional to the particle size and proportional to the velocity difference between gas and the particles($\propto (\boldsymbol{v_g} - \boldsymbol{v_{s,l}})$). For each particle type, the acceleration due to drag decreases with time due to a reduction in the velocity difference between the gas and particle velocity. Smaller particles experience a larger acceleration due to drag force, and so accelerate much faster than the larger particles. The larger particles, on the other hand, have greater inertia and relax slowly to the post-shock condition. Drag forces in the post-shock flow accelerate different particles at different rates. This, in turn, causes the uniformly fixed particle cloud to segregate into two different clouds. Here, the particle-hindrance effect is too small to reduce the velocity difference between the larger and the smaller particles.

For the simulation where the two particle bins have the same size but different densities, the drag forces acting on the two types of particles are similar, since the drag force is independent of particle density. The accelerations due to the drag force, however, are different for the two types of particles. Heavier particles have smaller accelerations due to drag than lighter particles since they have a greater inertia. Therefore, heavier particles propagate with a lower velocity than lighter particles, and this velocity difference causes the separation to occur.

For the case with higher particle volume fractions shown in Section 5.2.4, the particle hindrance effect and intergranular stress become important. Both of these effects tend to cause densely compacted particles to move together as a group. Particle hindrance and intergranular stress, however, become less influential at dilute particle volume fractions. The particles in each bin act independently in dilute regimes, where gas-phase drag and other aerodynamic effects dominate the motion of the particles. This is why particles only segregate at the dilute tail of the dense particle curtain.

5.2.5.2 Modeling Multiple Particle Types

The separation process in the simulations shown above indicates the necessity of modeling multiple particle types, since this effect cannot be captured using a single-sized particle model. Dividing the particles into different particle types leads to more accurate results when the particle size or density in the dust varies greatly.

This is especially important in 2D simulations of the dust-lifting process in an underground coal mine, where the particle size and density is crucial for applying inert rock-dust to reduce the coal-dust dispersion behind a moving shock wave. Similar to the 1D separation process, the rock and coal particles are expected to be lifted to different heights according to their sizes and densities. Therefore, dividing the particles into different types is essential in studying how the inert particles affect the motion of coal particles.

Increasing the number of particle types increases the realism of the computations, but it also increases the computational expense. The total number of equations in a one-dimensional, single gas-phase, non-reactive calculation involving N particle types is:

$$N_{eq} = 3 + 4N_{bin} \tag{5.2}$$

where N_{eq} is the number of equations involved and N_{bin} is the number of particle bins. For a calculation involving 6 particle bins, 27 equations are needed, and this can be even more computationally expensive for a two-dimensional calculation. There is, therefore, a tradeoff between the level of realism and accuracy of the simulation and the computational cost.

5.3 RESULTS: Two-Dimensional, Single Layer

5.3.1 Physical Model

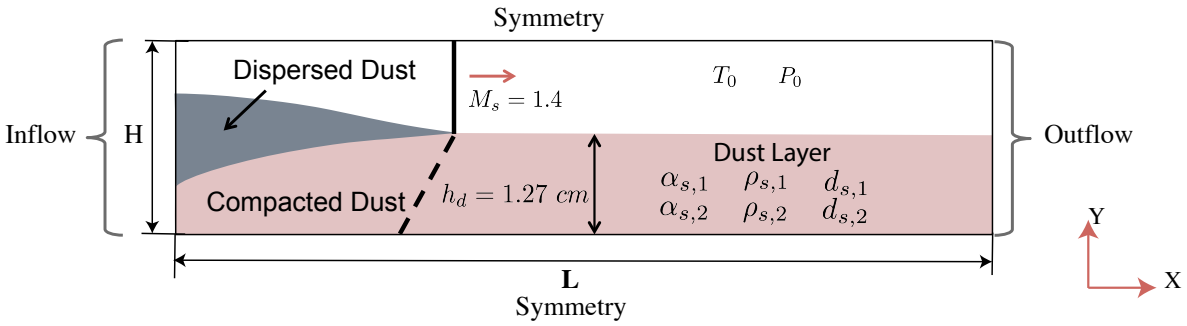

Figure 5.8: Initial setups for two-dimensional simulations. The layer contains two particle types that are uniformly mixed with each other.

This section presents two-dimensional simulations of a shock passing over a dust layer. The setup for the simulations is shown in Fig. 5.8. Initially, a layer of dust containing two uniformly mixed particle types is placed on the bottom of a channel. A shock wave of Mach 1.4 is moving from the left to the right. The dust-layer thickness (h_d) is 1.27 cm and the initial particle volume fractions for both particle types are set to be identical ($\alpha_{s1} = \alpha_{s2} = 0.235$). The background pressure (P_0) and temperature (T_0) are 67 kPa and 295 K, respectively. The left and right side of the channel are nonreflecting, inflow-outflow boundary conditions and the top and bottom side of the domain are symmetry planes. (These initial conditions are based on the experiments performed by Chowdhury et al. [76].) The input parameters are shown in Table 5.4.

Table 5.4: Initial parameters and geometrical condition for 2D simulations

Channel height	H	20 cm	
Channel length	L	300 cm	
Background temperature	T_0	295 K	
Background pressure	P_0	67 kPa	
Shock Mach number	M_s	1.4	
		Particle I	**Particle II**
Initial dust-layer height	h_d	1.27 cm	1.27 cm
particle volume fraction	α_s	0.235	0.235

Table 5.5: Input conditions of particle size and density

		Diameter (d_s) [μm]	Density (ρ_s) [kg/m^3]
Case I	Particle I	80	1300
	Particle II	10	1300
Case II	Particle I	120	1300
	Particle II	10	1300

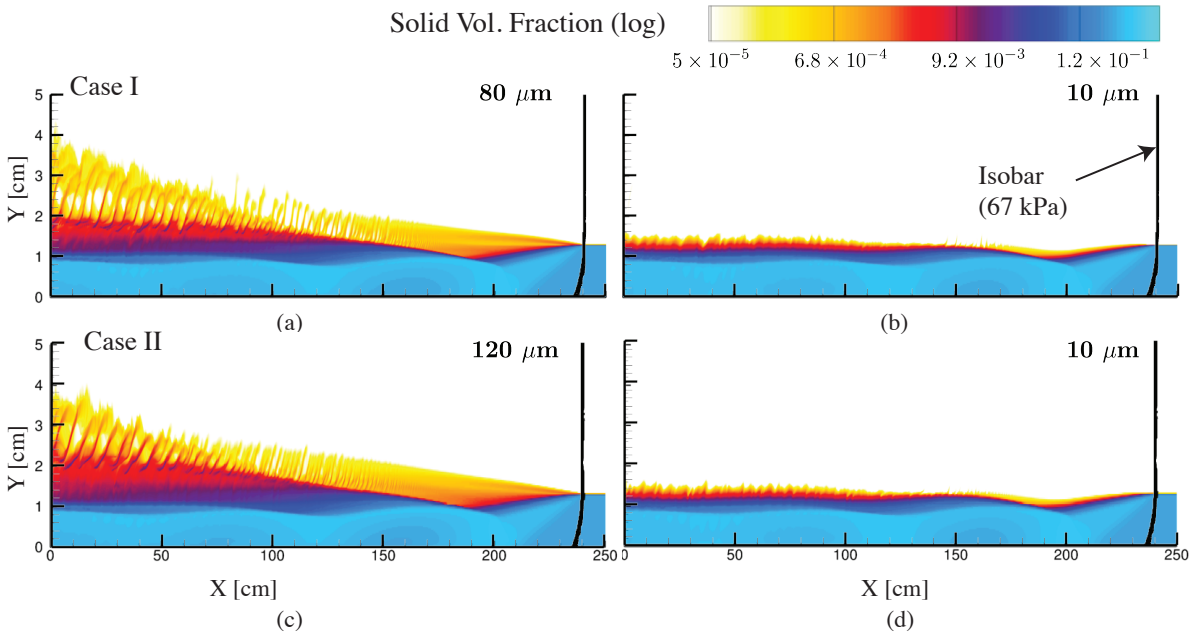

Figure 5.9: Computed particle volume fractions for both particle types in Case I and Case II. (a) Particle I in Case I ($d_s = 80$ μm); (b) Particle II in Case I ($d_s = 10$ μm); (c) Particle I in Case II ($d_s = 120$ μm); (d) Particle II in Case II ($d_s = 10$ μm).

5.3.2 Effect of Particle Size

Two test cases are performed to study the effect of particle size on dust dispersion. The size and density of the two types of particles are shown in Table 5.5. The particle density is assumed to be 1300 kg/m^3 and remain fixed. Particle type I is assumed to be the larger particles in both cases.

Figure 5.9 shows the particle volume fraction for both particle types in the two test cases. The isobar of $P = 67$ kPa indicates the location of the gas shock. Fig. 5.10 shows the edge of the dispersed dust (defined as $\alpha_s = 5 \times 10^{-5}$) with respect to the initial dust-layer height as a function of distance behind the shock wave. For each case, the larger-diameter particles (Fig. 5.9 (a) and (c)) are lifted significantly higher than the particles with smaller diameters (Fig. 5.9 (b) and (d)). The smaller particles are lifted

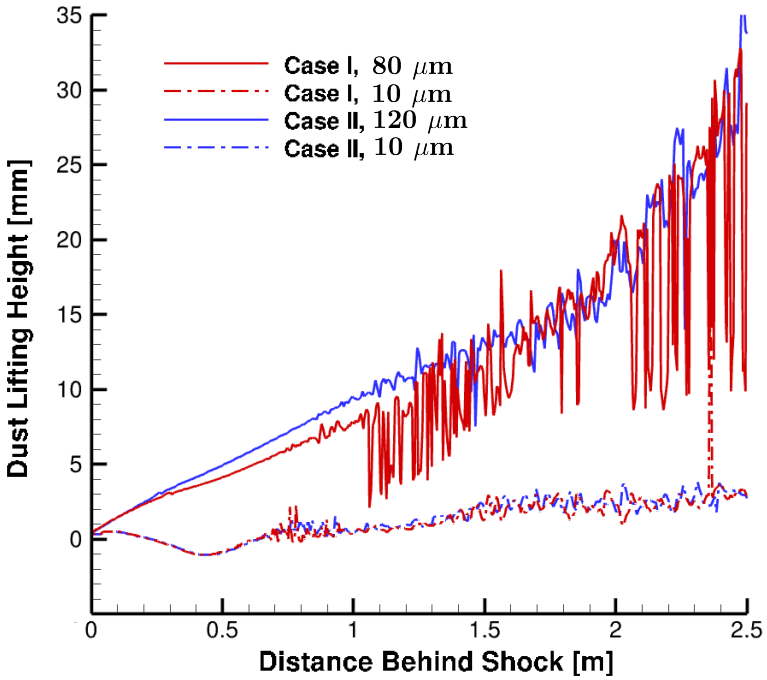

Figure 5.10: Computed dust lifting height for different particle diameters in both test cases. The edge of the dust layer is defined as $\alpha_s = 5 \times 10^{-5}$.

only a small amount. As we increase the size of type I particles from 80 μm (Case I) to 120 μm (Case II), the heavier 120 μm particles are lifted even higher, and more particles are dispersed than the 80 μm particles. In general, the dust lifting height depends strongly on the particle size. The reason for this and the related governing forces acting on different particle types will be addressed in the discussion section below.

5.3.3 Effect of Particle Density

Now consider simulations containing two particle types with identical particle size but different densities. Table 5.6 summarizes the input parameters for the two particle types. Figure 5.11 shows the particle volume fraction for both particle types in the two test cases with the location of the gas shock indicated. Figure 5.12 shows the dust lifting height as a function of distance behind the shock. These results indicate that the particle density has a minor effect on the dust-lifting height. In Case I, the dust

Table 5.6: Input conditions of particle size and density

		Diameter (d_s) [μm]	Density (ρ_s) [kg/m^3]
Case I	Particle I	80	1000
	Particle II	80	1500
Case II	Particle I	80	1000
	Particle II	80	3000

dispersion is very similar for the two types of particles. As the density of type II particles is increased from 1500 to 3000 kg/m^3 in Case II, the difference becomes more obvious. Heavier particles (3000 kg/m^3) are lifted lower than the lighter particles (1000 kg/m^3). Comparing the dust-lifting height in both cases, type I particles (1000 kg/m^3) are lifted higher in Case I than in Case II, even though their size and density remain unchanged.

5.3.4 Discussions

5.3.4.1 Effect of Particle Size

In the 2D calculations, larger particles are lifted higher than smaller particles. To understand why this occurs, the forces acting on both particle types are analyzed (Table 5.1). Figure 5.13 shows the net accelerations as well as the accelerations due to drag, lift, Archimedes force, intergranular stress, and particle-hindrance force for both particle types ($d_{s,1}$ =120 μm, $d_{s,2}$ =10 μm, $\rho_{s,1} = \rho_{s,2}$ = 1300 kg/m^3) along the vertical direction.

According to Ugarte et al. [69], the gas shock curves and degenerates into a compression wave as it enters the dust layer. The compression wave compacts the particles in the layer and evolves into a granular compaction wave through particle collisional and frictional effects. The compaction wave reflects from the bottom of the channel and forms a reflected compaction wave. This reflected wave propagates upwards and inter-

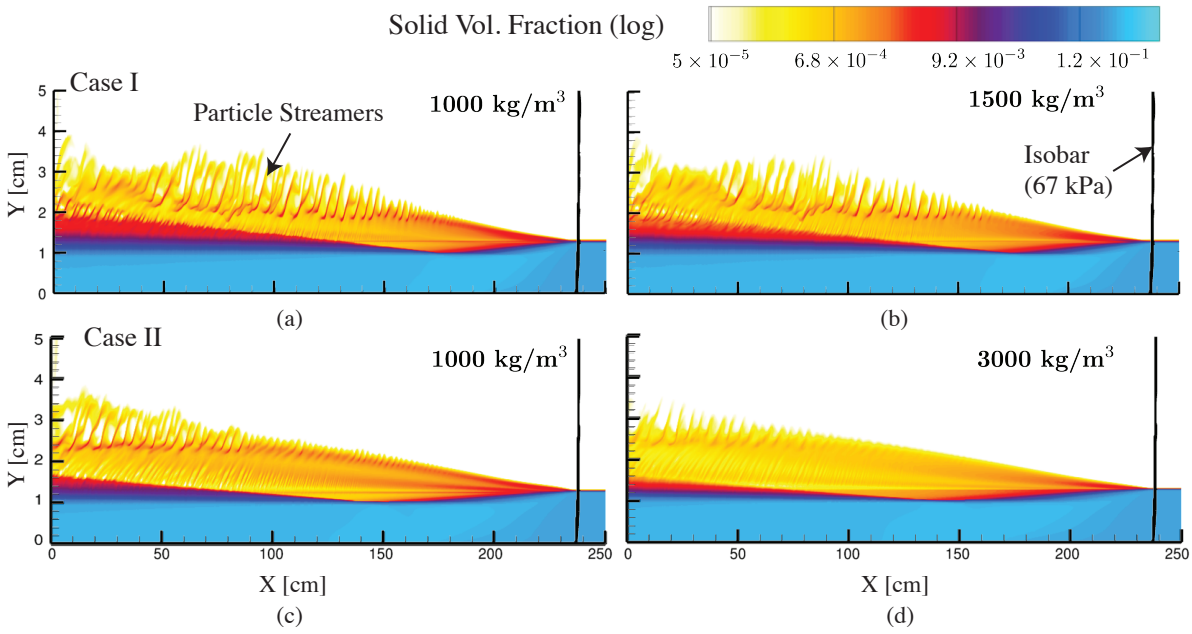

Figure 5.11: Computed particle volume fractions for both particle types in Case I and Case II. (a) Particle I in Case I ($\rho_s = 1000$ kg/m^3); (b) Particle II in Case I ($\rho_s = 1500$ kg/m^3); (c) Particle I in Case II ($\rho_s = 1000$ kg/m^3); (d) Particle II in Case II ($\rho_s = 3000$ kg/m^3).

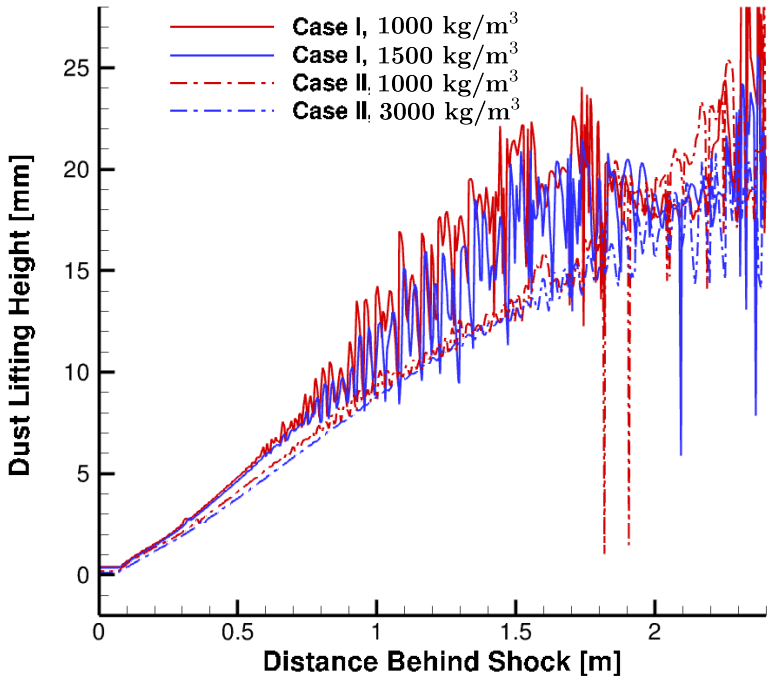

Figure 5.12: Computed dust lifting height for different particle densities. The edge of the dust layer is defined as $\alpha_s = 5 \times 10^{-5}$.

acts with the surface of the dust layer, producing acoustic waves, which can enhance the flow oscillation [69]. The compaction wave and reflected compaction wave are marked in the Intergranular Stress contour in Fig. 5.13.

The Archimedes force and intergranular stress for the two types are close, since they are not directly dependent on particle size. The particle-hindrance forces acting the two types of particles are equal in magnitude but opposite in sign, and they reduce the velocity differences between the two particle types. Similar to the 1D results, the drag forces for the two particle types are quite different. Smaller particles experience a larger drag. In the 2D simulations, the lifting force also plays a role since it is proportional to the velocity difference along horizontal direction (see Eq. (5.1)). Larger particles that are accelerated more slowly along the gas flow direction will result in a larger velocity difference between the particle and gas phase along horizontal direction. This in turn will result in a larger lift force normal to a boundary layer.

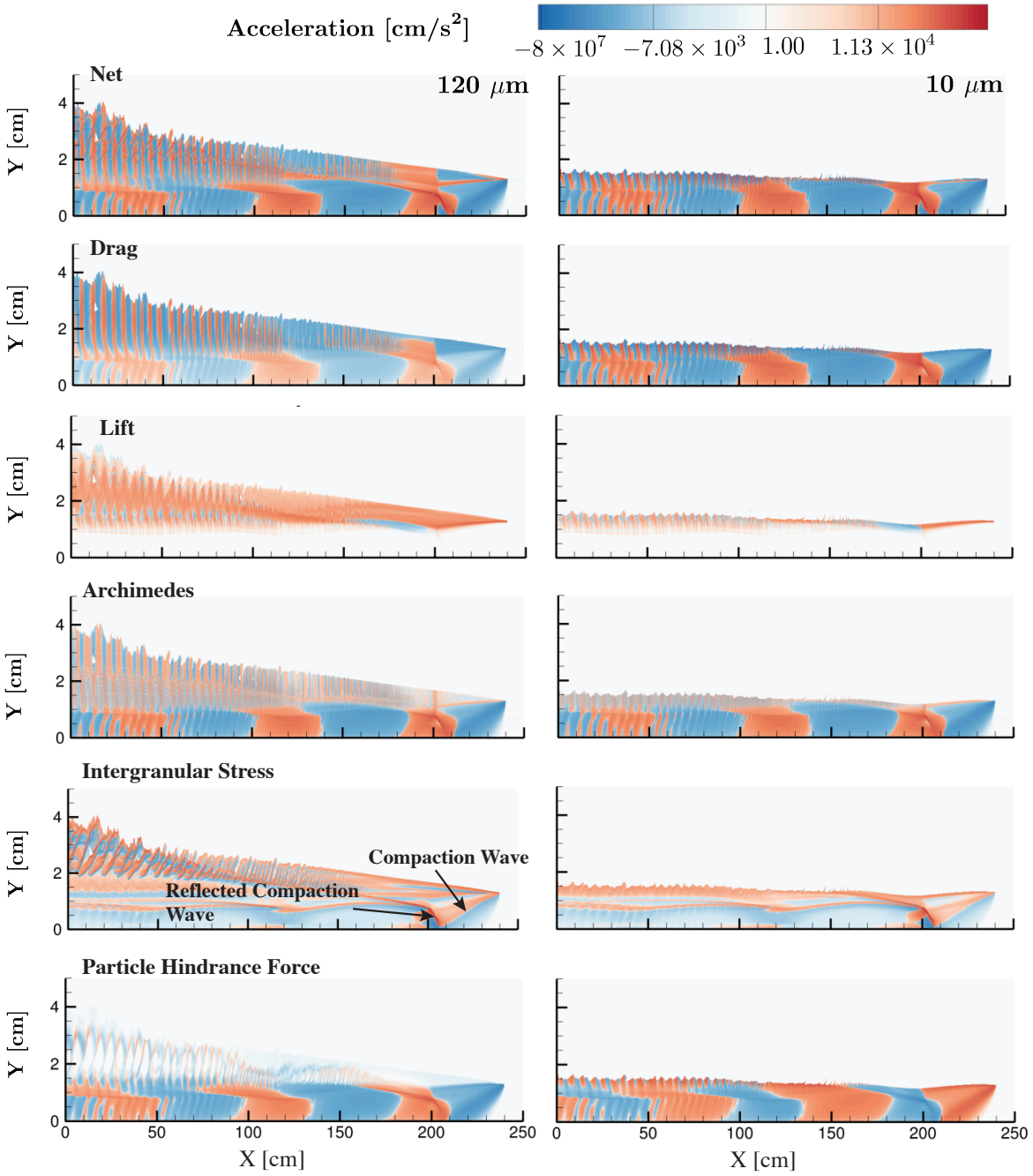

Figure 5.13: Net accelerations and accelerations due to drag, lift, Archimedes force, intergranular stress, and particle-hindrance force for both particle types (d_{s1} =120 μm, d_{s2} =10 μm, $\rho_{s1} = \rho_{s2} = 1300$ kg/m^3) along vertical direction. Forces have been normalized by $\alpha_s \rho_s$.

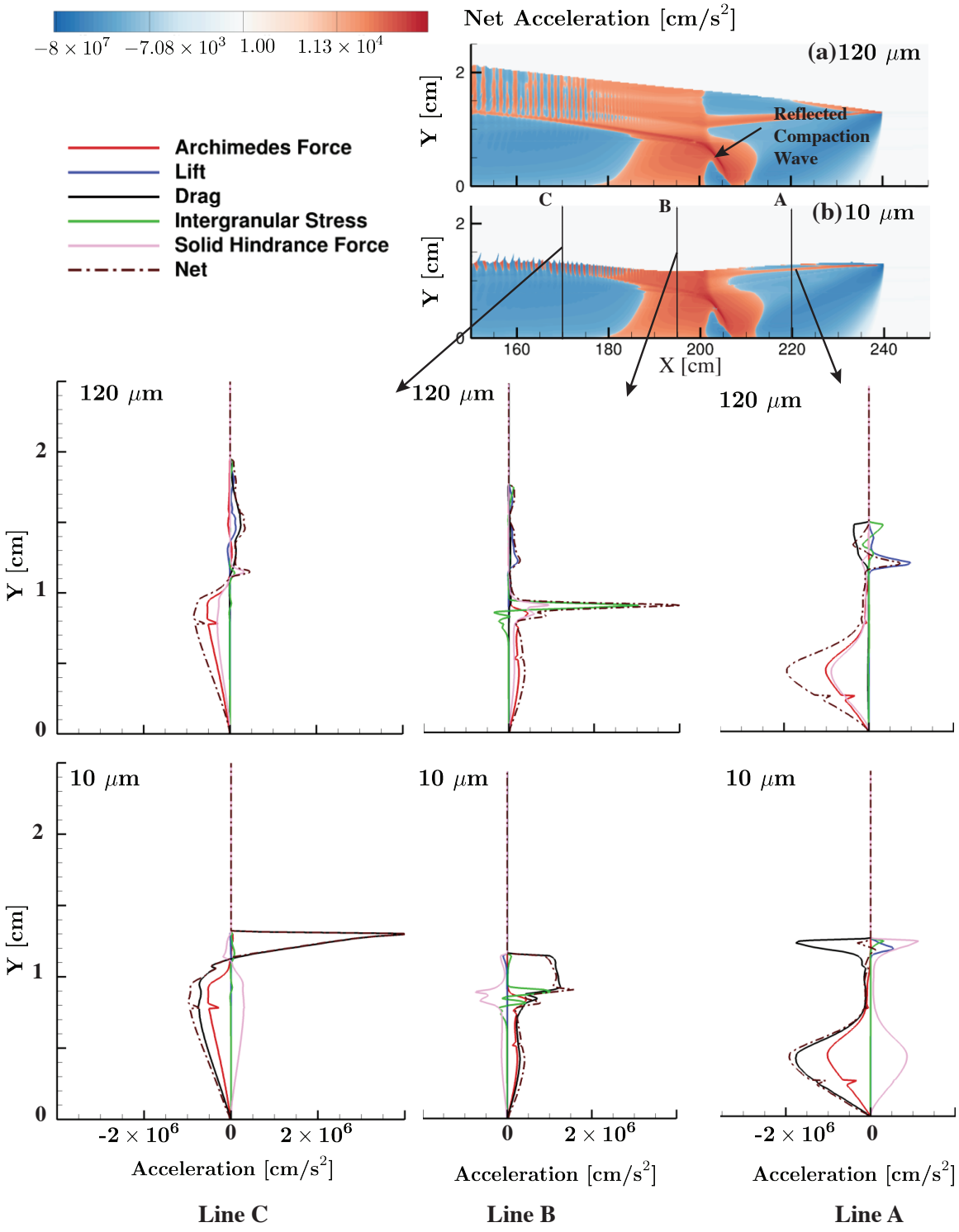

Figure 5.14: Vertical accelerations produced by drag, lift, Archimedes force, intergranular stress, and particle-hindrance force along three vertical lines indicated in the net acceleration color map for (a) $d_{s,1}$= 120μm, and (b) $d_{s,2}$= 10 μm. Forces have been normalized by $\alpha_s \rho_s$.

According to Ugarte et al. [69], the physical processes occurring near the shock front are the most important for dust lifting. The top left portion of Fig. 5.14 shows particle-acceleration contours in the region between 150 and 250 cm. The bottom portion of Figure 5.14 shows the vertical profiles of particle accelerations due to drag, lift, Archimedes force, intergranular stress, and particle-hindrance force. These profiles are shown for the locations indicated by the three arrows on the contours.

Along line A, which is close to the shock front, the drag and Archimedes forces accelerate particles downwards (negative y-direction), while the lift force and intergranular stress pull the particles upwards (positive y-direction). As discussed previously in the one-dimensional simulations, smaller particles experience a larger drag force. Therefore, greater acceleration due to the drag force is pushing the smaller particles (d_s = 10 μm) downwards. In addition, greater lift force is pulling the larger (d_s=120 μm) particles upwards in the dispersed region.

Line B is located behind the reflected compaction wave, where a positive net acceleration is produced for both particle types in the dust layer (between 180 cm and 210 cm). The type II particles are slightly lifted in regions downstream of 190 cm due to this positive acceleration. However, the lifting process is soon overcome through the compaction process (negative acceleration) that dominates in regions to the left of 180 cm.

Line C is located even further behind the shock wave, where there is a negative acceleration in the dust layer and an alternating positive and negative acceleration in the dispersed region. In this region, lift becomes less important and drag dominates. Larger acceleration due to drag is pushing the particles downwards in the dust layer for particle type II (d_s = 10μm). Although there is a large positive drag force above 1.2 cm along line C for particle type II, the net acceleration (see lower colormap) is highly oscillatory and the average value is low.

5.3.4.2 Effect of Density

Density is another important aspect affecting dust dispersion. Similar to the 1D result, the 2D simulations shown in Fig. 5.11 and Fig. 5.12 suggest that heavier particles are slightly lifted lower than lighter particles. Larger particles have a greater inertia and will experience a smaller acceleration given the same net force. In general, heavier particles require a longer responding time to the gas-phase condition.

In addition, the dust layer in the 2D simulations have a relatively high particle volume fraction ($\alpha_{s,1} = \alpha_{s,2} = 0.235$), and the particle-hindrance effect plays an important role in reducing the velocity difference between the two types of particles. Comparing the particle densities in both cases, the heavier particles in Case I have a density of 1500 kg/m^3, and the heavier particles in Case II have a even greater density (3000 kg/m^3). Therefore, the 3000-kg/m^3 particles are lifted lower than the 1500-kg/m^3 particles since they have a greater inertia. Meanwhile, the heavier particles in both cases exert a particle-hindrance force on the lighter particles (1000 kg/m^3) that is pulling the lighter particles downwards. The 3000-kg/m^3 particles, which has the greatest inertia and are lifted to the lowest height, produces a higher particle-hindrance force than the 1500-kg/m^3 particles. This particle-hindrance effect explains why type I particles (1000 kg/m^3) are lifted higher in Case I than in Case II, even though the size and density of particle type I remain unchanged.

5.3.4.3 Effect of Grid Refinement

Numerical resolution tests have been performed with 3, 4, and 5 levels of refinement, corresponding to the minimum computational cell sizes of 625, 312.5, and 156.3 μm. The computed particle volume fraction contours and dust lifting heights for the case where a shock passes over a dust layer containing 80 μm particles are shown in Fig. 5.15 and Fig. 5.16. The gas shock is located at 1.3 m and is moving from the left

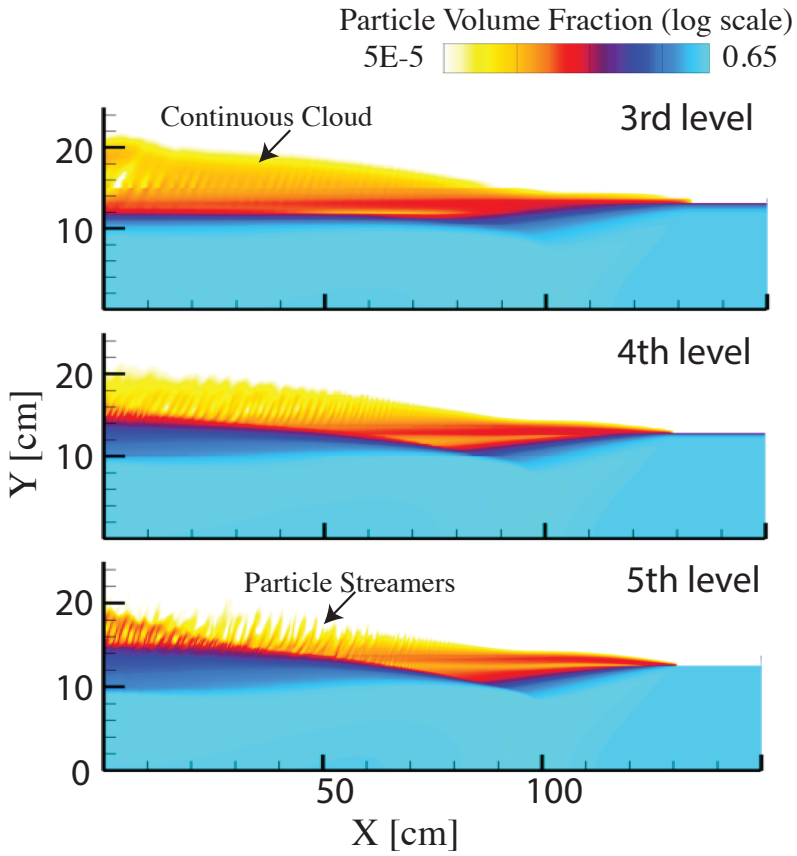

Figure 5.15: Computed particle volume fractions of a shock passing over a layer of dust containing 80 μm particles (ρ_s=1300 kg/m^3) with 3, 4, and 5 levels of refinement.

to the right.

The particle volume fraction contours shown in Fig. 5.15 suggest that particles are more dispersed for simulations using a coarser mesh. For the result with 3 levels of refinement, a continuous particle cloud is formed in the dispersed region. For the case with 5 levels of refinement, however, "particle streamers" (i.e. string-like clusters of high-concentration particles) are observed. The formation of "particle streamers" results in the huge fluctuations shown in Fig. 5.16. The mean value of the dust lifting height with 5 levels of refinement (green curve in Fig. 5.16) is, in general, lower that that using a coarser mech. Nevertheless, the peak of the dust lifting curve with 5 levels of refinement can have the highest value among the three test cases due to its huge fluctuations. We

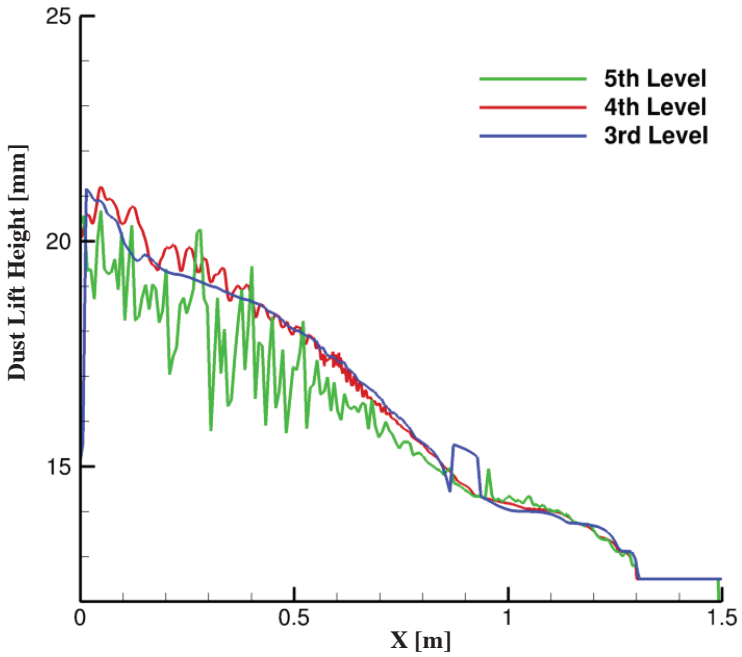

Figure 5.16: Computed dust lifting heights of a shock passing over a layer of dust containing 80 μm particles (ρ_s=1300 kg/m^3) with 3, 4, and 5 levels of refinement.

also find that although the particle streamers are not clearly observed in the simulations with 3 and 4 levels of refinement, we do notice some discontinuities in particle volume fractions (i.e. fluctuations) in the dispersed region. These fluctuations have similar wavelengths as the particle streamers found with 5 levels of refinement. This suggests that the formation of particle streamers are physical phenomenon observed during the dust lifting process. Simulations with a coarser mesh (3 and 4 levels of refinement) fails to capture these structures and 5 levels of refinement is recommended.

Similar grid resolution tests have been performed for the case of a shock passing over a dust layer containing 10 μm and 80 μm particles. The computed particle volume fractions and dust lifting heights are shown in Fig. 5.17 and Fig. 5.18. The gas shock is located at 2.2 m and is moving from the left to the right. In these tests, the initial dust-layer height was decreased from 1.27 cm to 1.25 cm so that all three test cases can have an identical layer thickness.

These tests show reasonable convergence for the small 10-μm particles. For the larger particles, the results show reasonable convergence in the region starting at the shock wave extending back about 1 m. In the region beyond 1 m, the mean values are roughly converged, but the fluctuations in the solution increase with increasing resolution. Similarly, the increasing fluctuation is related to the formation of "particle streamers" in the dilute dispersed region shown in Fig. 5.17. These particle streamers are known to not converge under grid refinement using Eulerian-Eulerian methods [77]. In general, we do not expect such a fluid model of a granular flow to be very accurate when there are so few (less than 2) particles per cell. Nonetheless, this is encouraging because we see that we do get better solution with less fluid resolution. Resolving this convergence issue will likely require extending methods to include more advanced models of particle interactions, such as a quadrature-based moment technique [78], which allows particle trajectories to cross. This type of model development is beyond the scope of this work.

5.3.4.4 Sensitivity of Results to Model Assumptions

There are a number of important assumptions that have been made to arrive at the Eulerian model used in this work. First, the model neglects several terms, such as viscous stresses, granular energy exchange between different bins, and dissipation of PTE due to collisions between different bins, that are in the complete theory. We recognize that for very dilute flow in one dimension, these terms are negligible because of the low solids volume fraction. This may not be true for the two-dimensional cases where the particle volume fraction is high. In general, viscous stresses and dissipation of PTE due to collisions between bins are neglected because tests we have done have shown that including these terms does not produce any significant effects on the dust dispersion height, which is our major concern in this study. In addition, we would like

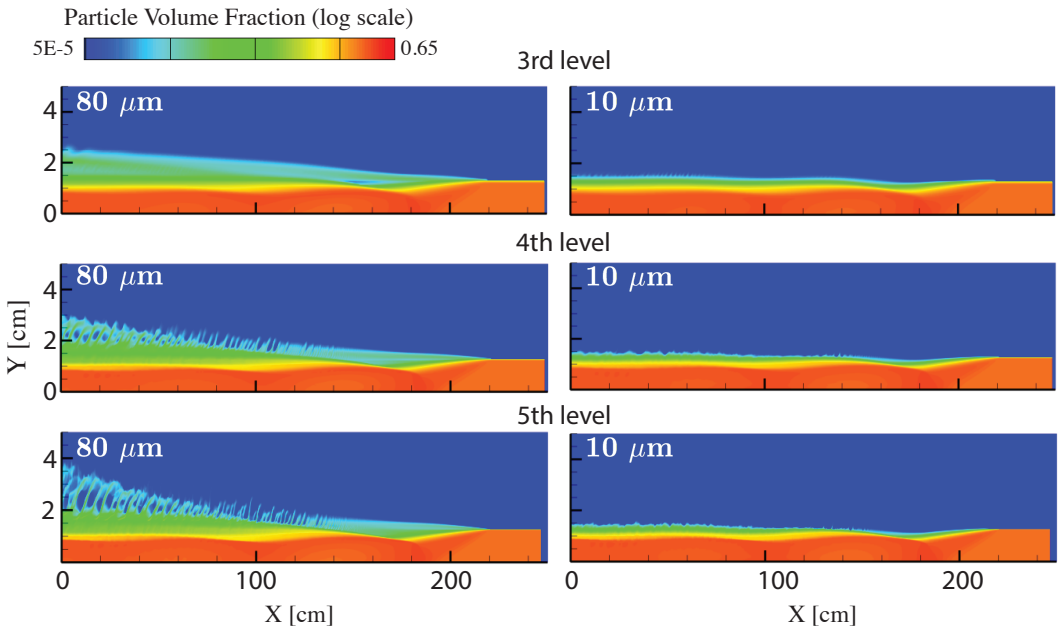

Figure 5.17: Computed particle volume fractions of a shock passing over a layer of dust containing two uniformly mixed particle types with 3, 4, and 5 levels of refinement ($\rho_{s1} = \rho_{s2}$=1300 kg/m^3; d_{s1}=10 μm; d_{s2}=80 μm). The edge of the dust layer is defined as $\alpha_s = 5 \times 10^{-5}$.

to validate the choice of several models used for g_0, p_s, p_{fric}, etc., as well as the use of some empirical coefficients (e.g., e, C_l, $\alpha_{s,crit}$, and S_{coef}). Here we will discussion some of the most important tests that illustrate the validity of these.

1. **PTE Exchange Terms**

   To valid our assumption of neglecting the granular energy exchange and the dissipation of PTE due to inelastic collisions between different particle bins, simulations with the granular temperatures turned off ($\theta_l = \theta_m = 0$) were performed and the results are compared to the cases shown in Section 5.3.2. By doing this, we are comparing the limiting case, where there is no granular energy for the system, to our current results where the granular energy is slightly higher than the expected value (since we neglected the dissipations due to inelastic collisions between different bins). Figure 5.19 compares the edge of the dust layer ($\alpha_s = 5 \times 10^{-5}$)

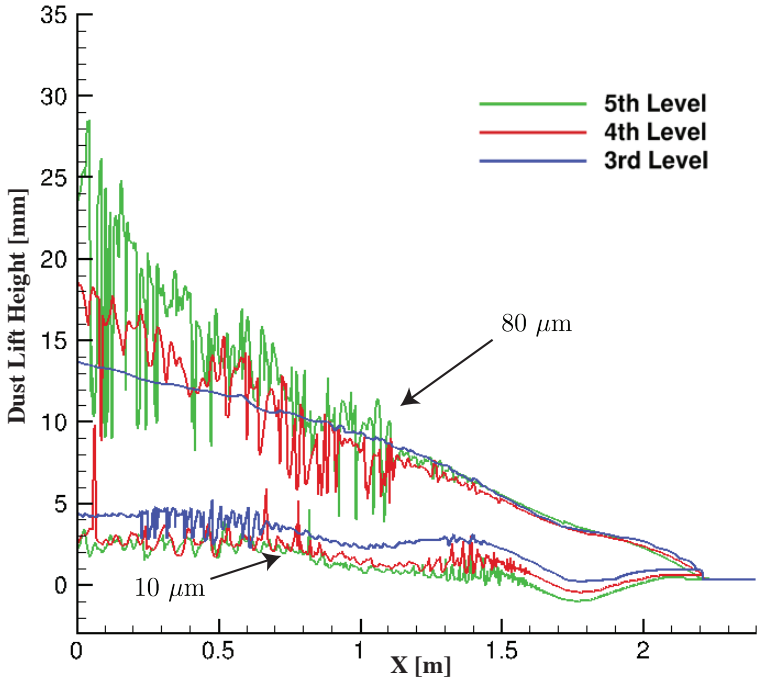

Figure 5.18: Computed dust lifting heights of a shock passing over a layer of dust containing two uniformly mixed particle types with 3, 4, and 5 levels of refinement ($\rho_{s1} = \rho_{s2}$=1300 kg/m^3; d_{s1}=10 μm; d_{s2}=80 μm). The edge of the dust layer is defined as $\alpha_s = 5 \times 10^{-5}$.

assuming zero granular temperature with the results using our current model.

This result indicates that dust is lifted lower for the case with zero granular temperatures, since the solids pressure is eliminated. The difference is more obvious for the case shown on the left ($d_{s1} = 120\ \mu m$, $d_{s2} = 10\ \mu m$) and in regions close to the gas shock. In general, the difference between our current results and the zero-temperature results is insignificant, and the overall trend of the dust dispersion remains unchanged. Including the dissipation terms between different bins result in dust-lifting heights that fall between the cuttent results and the zero-temperature results. Nevertheless, obtaining the correct amount of energy dissipation and PTE exchange between different bins can be important to our future study, and including these terms is part of our future work.

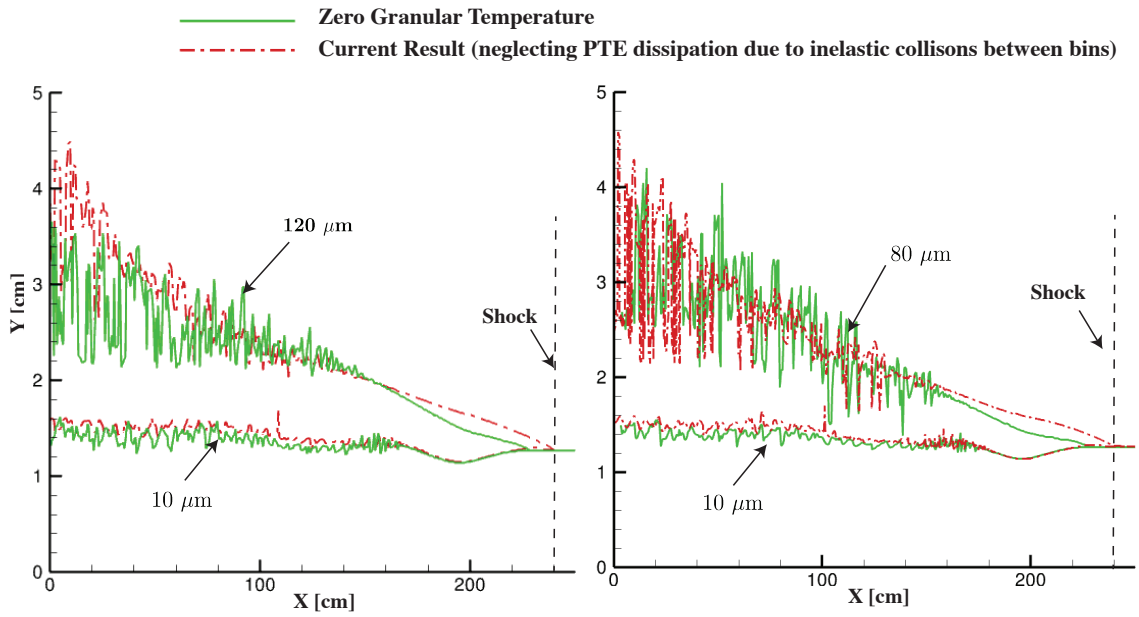

Figure 5.19: Comparison of dust lifting height for the case with zero granular temperatures (solid line) and the case using current model (dased line). Left: case I ($d_{s1} = 120\ \mu m$, $d_{s2} = 10\ \mu m$); Right: Case II ($d_{s1} = 80\ \mu m$, $d_{s2} = 10\ \mu m$).

2. **Viscous Stresses**

   In addition, the granular viscous stress terms are neglected in our model. In our research, the major problem of interest is the dispersion height of the dust layer. The densely packed region, where the collisional and friction viscosity plays a more important role, is less important to us here than the dispersed region. In a similar simulation, Ugarte *et al.* showed that the height of the dispersed dust is in close agreement with the experimental data when granular viscosity terms was ignored [69]. Based on these arguments and for simplicity, the viscosity terms are currently neglected in our simulations. The effect of including the viscosity on dust dispersion is a topic worthy of future study.

3. **Collisional Pressure Coefficient, S_{coef}**

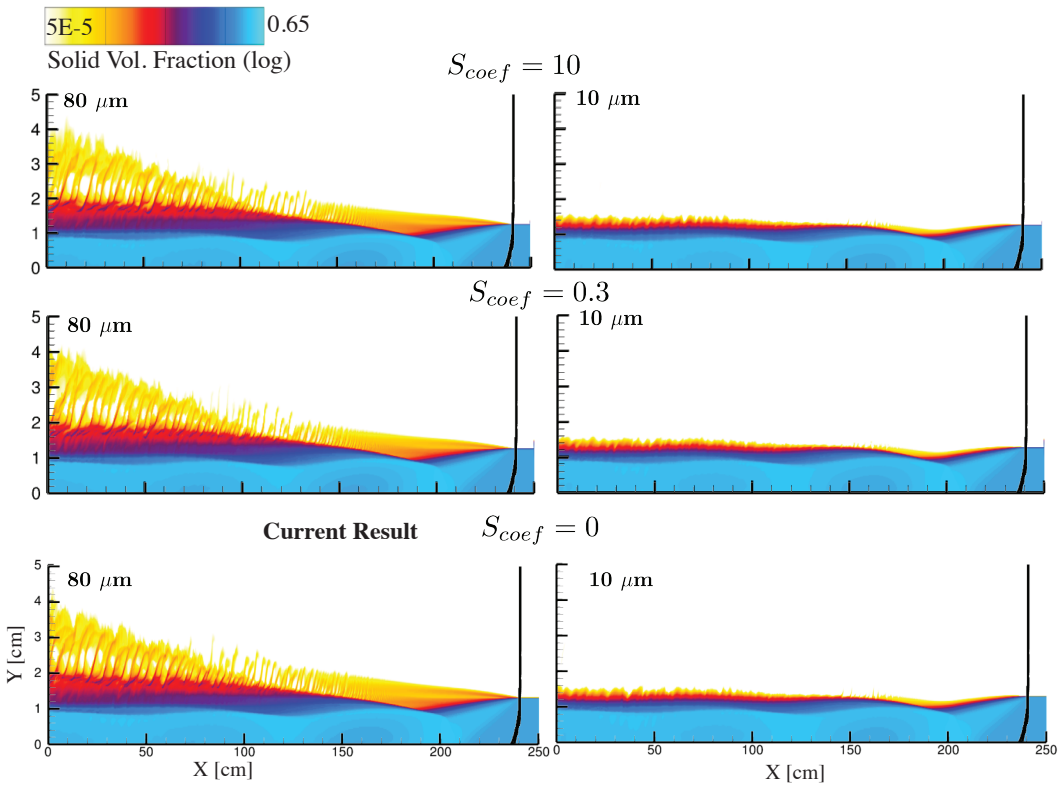

Figure 5.20: Particle volume fraction of a shock passing over a dust layer containing two types of particles ($d_{s1} = 80\ \mu m$, $d_{s2} = 10\ \mu m$) with $S_{coef} = 10$, 0.3, and 0.

The solid-solid momentum exchange is calculated using the Syamlal-O'Brien symmetric model [49] and has been used in a number of works to study the motion of dense gas-solid-fluidized beds [85, 86, 24].

$$K_{lm} = \frac{3(1+e_{lm})(\frac{\pi}{2} + C_{fr,lm}\frac{\pi^2}{8})\alpha_l\rho_l\alpha_m\rho_m(d_l+d_m)^2 g_{0,lm}}{2\pi(\rho_l d_l^3 + \rho_m d_m^3)}|\boldsymbol{v}_l - \boldsymbol{v}_m|. \tag{5.3}$$

This expression neglects the dependece on θ_l and θ_m. In fact, K_{lm} should be nonzero when the velocity difference, $|\boldsymbol{v}_l - \boldsymbol{v}_m|$, is null but $\theta_l > 0$ or $\theta_m > 0$.

Therefore, Gera *et al.* [87] extended this solid-solid exchange model by adding a second term $S_{coef}P_c$ on the right side of Eqn (5.3).

$$K_{lm} = \frac{3(1+e_{lm})(\frac{\pi}{2} + C_{fr,lm}\frac{\pi^2}{8})\alpha_l\rho_l\alpha_m\rho_m(d_l+d_m)^2 g_{0,lm}}{2\pi(\rho_l d_l^3 + \rho_m d_m^3)}|\boldsymbol{v}_l - \boldsymbol{v}_m| + S_{coef}P_c \tag{5.4}$$

This extra term is related to the granular pressure and works to prevent particle segregation in packed regions (allows nonzero K_{lm} when velocity difference is null but $\theta_l > 0$ or $\theta_m > 0$). The coefficient S_{coef} in the second term is an empirical value, and is difficult to calibrate for our simulations due to a lack of experimental data. A universal value of this coefficient is not available and a default value of zero has been used to the simulations presented in this paper.

To test the sensitivity of our model to the term S_{coef}, simulations are performed with $S_{coef} = 0.3$, and 10. The results are shown in Fig. 5.20 and is compared with the results using our current model ($S_{coef} = 0$). We find that the dust dispersion behavior for both types of particles are very similar in all the three cases. Thus, the additional $S_{coef} P_c$ term produce negligible effcts for our simulations.

4. **Lift Coefficient,** C_l

Lift coefficient, C_l, typically takes a value of 0.5 for invicid flow [17, 48]. A parametric study has been conducted to study the effect of different lift coefficients on dust dispersion. Figure 5.21 shows the dust lifting heights with $C_l = 0$, 0.1, 0.5, 1, and 10. We find that dust lifting heights are largely affected by the value of lift coefficients. In the future, we would like to compare our simulations results with experimental data to determine the appropriate C_l value.

5. **Radial Distribution Function,** g_0

The radial distribution function (RDF) in Eq. (3.15) was derived by Lebowitz in 1964 [79] for polydispersed systems.

$$g_{0,lm} = \frac{1}{\alpha_g} + \frac{3 d_l d_m}{\alpha_g^2 (d_l + d_m)} \sum_{q=1}^{M} \frac{\alpha_q}{d_q}, \tag{5.5}$$

For a system containing only one type of particles ($d_l = d_m$), the expression reduces to

$$g_0 = \frac{1}{1 - \alpha_s} + \frac{3\alpha_s}{2(1 - \alpha_s)^2}. \tag{5.6}$$

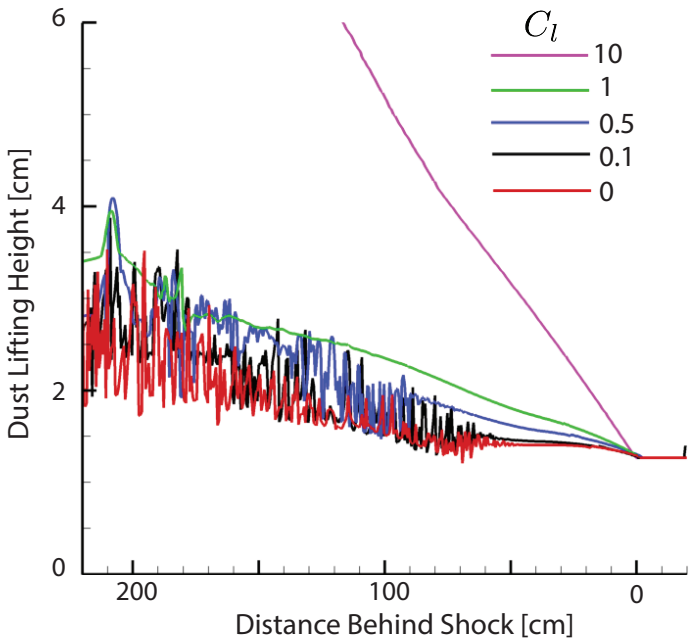

Figure 5.21: Dust-lifting heights of a shock passing over a dust layer containing two types of particles ($d_{s1} = 80\ \mu m$, $d_{s2} = 10\ \mu m$) with differrent lift coefficents. Here, only the dust-lifting heights for the 80 μm particles are shown.

We notice that this relation is slightly different from the well known Carnahan-Starling equation of state [80], which is usually considered to be quite accurate for single-sized particles. The Carnahan-Starling relation gives

$$g_0 = \frac{1}{1-\alpha_s} + \frac{3\alpha_s}{2(1-\alpha_s)^2} + \frac{\alpha_s^2}{2(1-\alpha_s)^3}. \tag{5.7}$$

Fig. 5.22 shows that the Lebowitz relation results in a smaller RDF value than the Carnahan-Starling model (especially in regions near the compaction limit). Similarly, Iddir & Arastoopour compared the RDF proposed by Lebowitz with the results from a MD simulation [81]. They concluded that the Lebowitz RDF was accurate for solid volume fractions ranging from 0 to 0.5, and became lower than the MD results near the packing limit. In principle, the Lebowitz RDF will result in a slightly lower granular pressure in regions near the packing limit. This effect is less important to our simulations since we are more interested in the dispersed

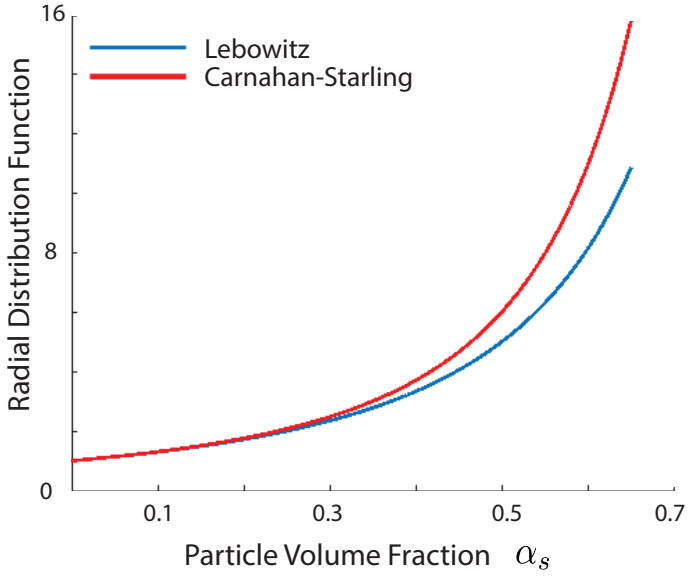

Figure 5.22: Comparison between Lebowitz relation and Carnahan-Starling relation.

region, where the Lebowitz RDF agrees well with the MD simulation as well as the Carnahan-Starling relation.

6. **Frictional Pressure, P_{fric}**

The frictional pressure model in Eq. (3.22) is developed by Johnson & Jackson [29]. There are a number of other expressions for the friction-collisional pressure available (Koo & Kuo [82], Markatos & Kirkcaldy[83], Nussbaum *et al.* [84], etc.). The expression in Eq. (3.22) is chosen because it only depends on the particle volume fractions (α_s) and is simple to implement. Houim and Oran showed that the computed results using this expression match closely with the experimental measurements in dense regions [1]. To test the sensitivity of our model to the frictional pressure model used, a simulation with $2 \times P_{fric,l}$ is performed. The results with double P_{fric} and the results using the current model are compared in Fig. 5.23. The results suggest that particles with double frictional pressure become slightly less compacted and are lifted to a higher level. The difference is, however,

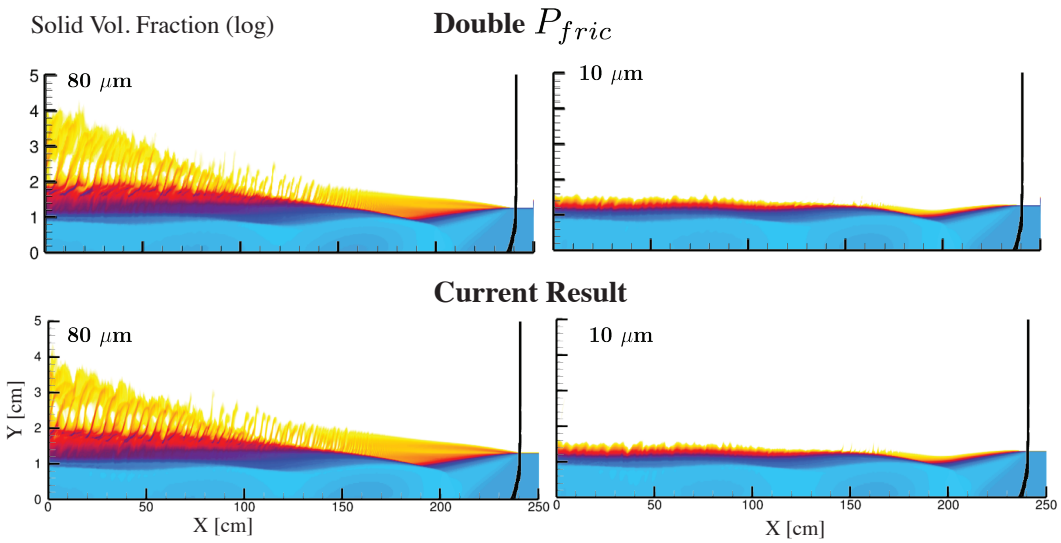

Figure 5.23: Particle volume fraction of a shock passing over a dust layer containing two types of particles ($d_{s1} = 80\ \mu m$, $d_{s2} = 10\ \mu m$). Top: simulation results with $2 \times P_{fric,l}$; Bottom: results with current model ($1 \times P_{fric,l}$).

very small. Exploring alternative frictional pressure models is part of future work.

5.4 RESULTS: Two-Dimensional, Multiple Layers

From previous sections, we know that when a shock passes over a single dust layer containing different particle types, the different types of particles in the mixture separate into different regions. Larger particles are lifted higher than smaller particles. This result leads to the questions: *What is the consequence of placing a layer of smaller particles on top of a layer of larger particles? How would particle size affect the particle dispersion in stratified dust layers?* Furthermore, we would like to investigate the dispersion of stratified coal- and rock-dust layer in real coal mine scenarios, where the properties of coal and rock dust are applied. The answers to these questions will be discussed in the following sections.

5.4.1 Physical Model

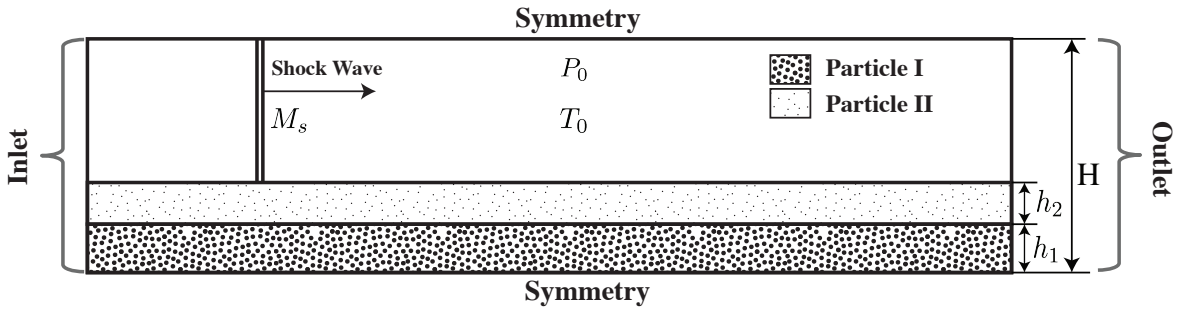

Figure 5.24: Schematic diagram of the initial conditions for the two-dimensional simulations where a shock of strength M_s travels over two dust layers. A dust layer containing particle type I of thickness and h_1 lies underneath a dust layer containing particle type II of thickness h_2.

Figure 5.24 shows the initial and boundary conditions for the simulations. The two-dimensional channel is 10.2 cm high and 7 m in length. A Mach 1.4 shock placed at $x_{\text{shock}} = 5$ cm is propagating over two dust layers that consist of either particle type I or

II. The background temperature (T_0) and pressure (P_0) is 295 K and 67 kPa, respectively. The post-shock condition is determined by the Rankine-Hugoniot relations. The left and right side of the channel are non-reflecting, inflow-outflow boundary conditions and the top and bottom side of the domain are symmetry planes. The gas is assumed to be air. Both types of particles have an initial volume fraction (α_s) of 0.47, and a coefficient of restitution, e, of 0.9.

5.4.2 Effect of Particle Size

5.4.2.1 Dispersion of 10-μm Particles on 80-μm Particles

The computed results of a shock passing over two layers of dust, where the top layer contains 10-μm particles and the bottom layer contains 80-μm particles are shown in Fig. 5.25. Here, both particle types have the same density, 1300 kg/m^3. The bottom and top layers have thicknesses of $h_1 = 10$ mm and $h_2 = 2.7$ mm, respectively. The top two images in Fig. 5.25 show the particle volume fractions for the top and the bottom dust layers (10 μm and 80 μm). The third image demonstrates the location of each type of particles in the dust mixture. Particle volume fractions below 0.005% are not shown. The bottom image shows the gas pressure contour with the gas-phase streamlines (shock-attached frame). Note that a very small region of mixed particle types sits between the two layers in the region to the right of the vertical line marked "Gas Shock" in Fig. 5.25. Besides being a more realistic representation of the physics, this also eliminates a sharp discontinuity in the initial conditions.

The top three figures show that far enough behind the leading shock, the larger particles (80 μm) placed in the lower layer are lifted much higher than the smaller particles that comprise the upper layer. Starting at the leading shock and moving upstream, the dust-lifting process can be divided into two stages: I) Compressing and Mixing stage, and II) Dispersing stage. In stage I, the top layer is pushed into the bottom

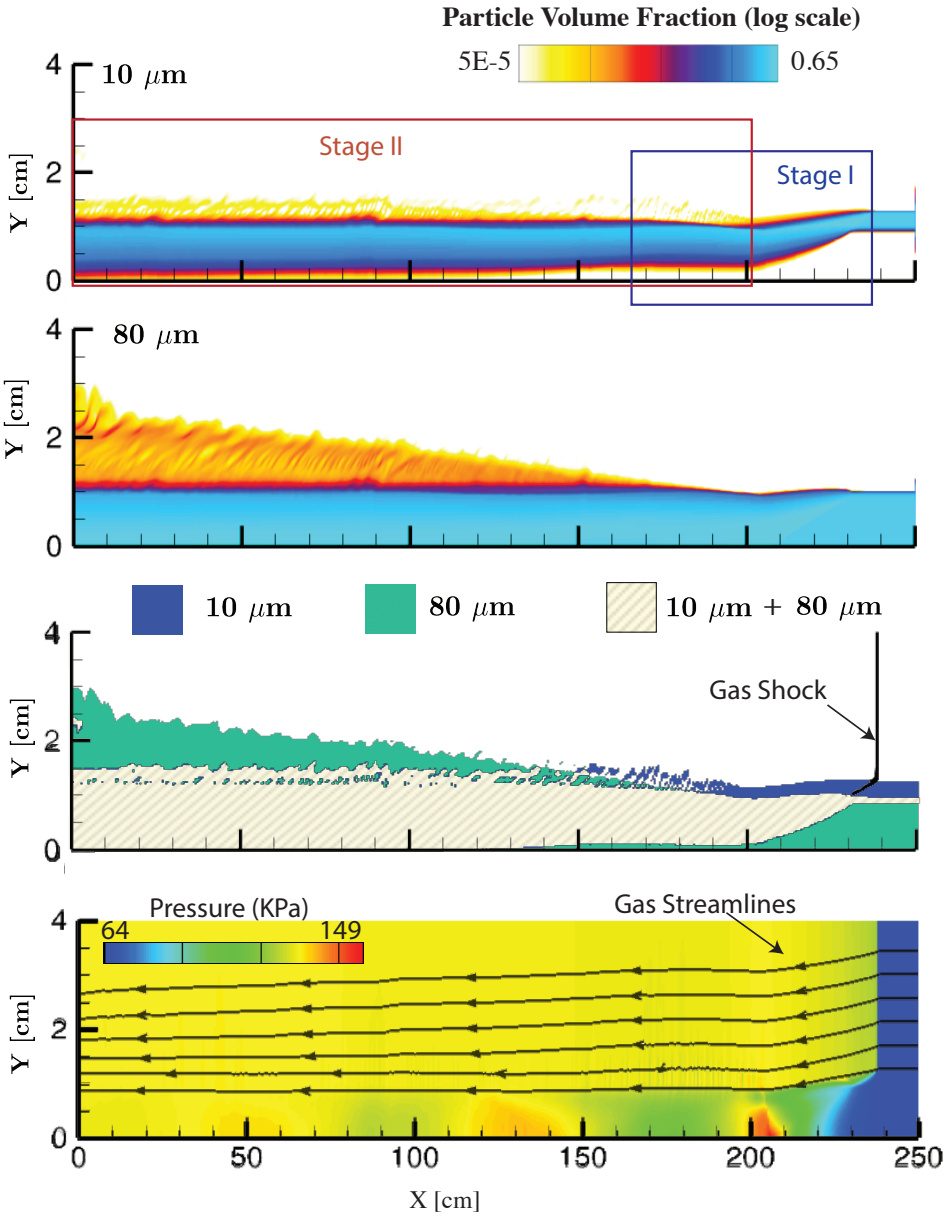

Figure 5.25: Simulation results of a Mach 1.4 shock passing over two layers of dust, where the top layer contains 10 μm particles and the bottom layer contains 80 μm particles. The top two images show the particle volume fraction contours of the 10 μm and 80 μm particles. The third image shows the location of each type of particle. The bottom image shows the gas pressure contour with the gas phase streamlines (shock-attached frame) indicated.

layer through gas-phase pressure and drag forces, so that the gas flow streamlines (lowest frame in Fig. 5.25) turn downwards to follow the compressing dust layer. During this stage, the two layers are mixing with each other, forming a region where both types of particles coexist.

Then, in stage II, the particles in the mixed region begin to be lifted. The dispersing mechanism is similar to what we found in our earlier studies of two types of particles mixed in a single dust layer. The larger particles are lifted to a higher level than smaller particles due to the differences in the Magnus lifting force and drag force [2]. Note that during this dispersion process, both "mixing" and "unmixing" of the two types of particles are observed, and particle segregation phenomenon plays a huge role in the overall lifting process.

5.4.2.2 Increased Particle Size in the Top Layer (d_s=10, 20, and 40 μm)

Here, the effect of the particle size in the top layer is explored. Three test cases with particle sizes of d_s = 10, 20, and 40 μm in the top layer are considered, and the particle size in the bottom layer remains at 80 μm. All of the other input parameters are the same as described in Section 5.4.2.1. The particle volume fractions and the edge of the dispersed dust ($\alpha_{s,edge} = 0.005\%$) for both layers in the three test cases are shown in Fig. 5.26 and Fig. 5.27.

Figure 5.26 and 5.27 indicate that the top layer with smaller particles is lifted higher as the size of the small particles increases. The edge of the bottom layer (80 μm) shown in Fig. 5.27 is lifted to a similar height in all three cases, with Case III slightly lower than Case I. The particle volume fractions of the bottom layer shown in Fig. 5.26, however, indicate that the bottom layer becomes much less dispersed as the particle size in the top layer increases. We find that the larger particles from the lower layer are lifted higher than the smaller particles from the upper layer in Cases I and II. This

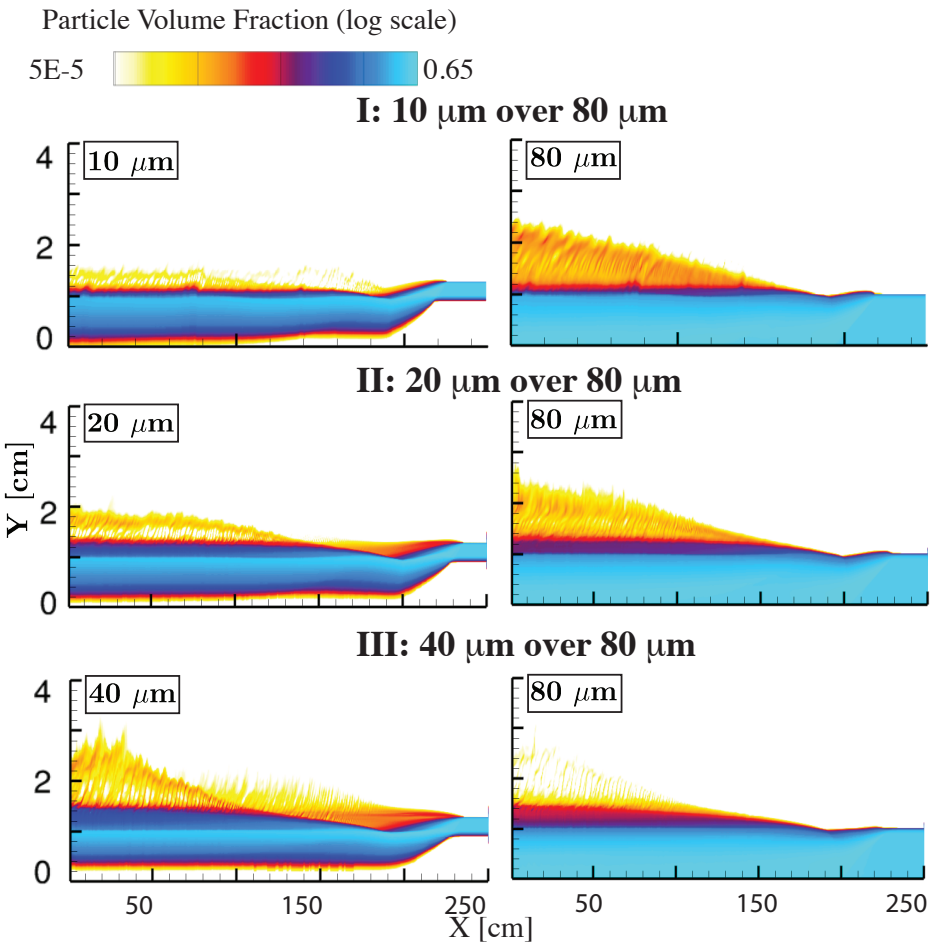

Figure 5.26: Computed particle volume fractions of the top and bottom layer for the three test cases. The top layer contains particles of 10, 20, and 40 μm, respectively. The bottom layer contains particles of 80 μm.

conclusion is then challenged in Case III as we further increase the particle size in the top layer, and the larger particles in the lower layer (80 μm) are now less dispersed than the smaller particles (40 μm) in the top layer.

These results show that the dispersion of the stratified dust layer is largely dependent on the size difference between the two types of particles. Larger particles from the bottom layer are lifted higher than smaller particles from the top layer only when the two types of particle have a relatively large size difference.

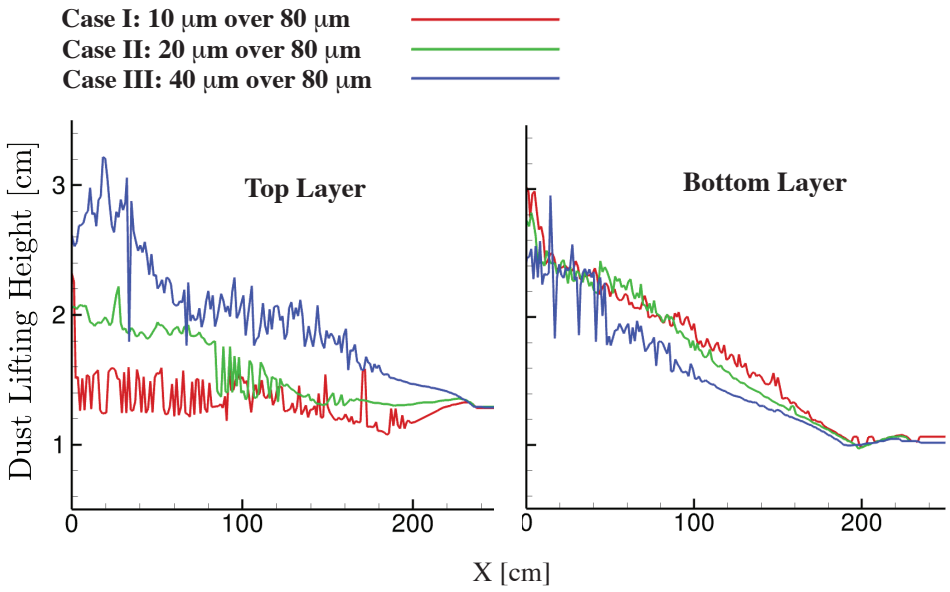

Figure 5.27: Computed dust-lifting height for the top layer (left), and the bottom layer (right) for the three test cases. The edge of the dust layer is defined as $\alpha_s = 0.005\%$

5.4.2.3 Dispersion of Very Thin Dust Layers

Table 5.7: Particle sizes in the first test series.

First Series	Particle Size (μm)	
	Top Layer	Bottom Layer
Case I	15	15
Case II	15	30
Case III	15	60

In the simulations shown above, the dust layers were relatively thick (10 mm for the bottom layer and 2.7 mm for the top layer) compared to those in a real coal mine. In such actual situations, experiments showed that a minimum of 0.12-mm thick layer of coal dust would propagate an explosion [88]. Therefore, at the request of OMSHR personnel, we proceed to study the particle size effect in a thinner case, where the bottom layer has a thickness of 3 mm, and the top layer has a thickness of 0.32 mm.

Table 5.8: Particle sizes in the second test series.

Second Series	Particle Size (μm)	
	Top Layer	Bottom Layer
Case I	15	15
Case II	30	15
Case III	60	15

Now two new series of tests were performed. In the first test series, the bottom layer has larger particles (Table 1). In the second test series, the top layer has larger particles (Table 2). The densities for all particles are fixed at 1330 kg/m^3.

Figure 5.28 shows the dust lifting heights for the three simulation cases in first test series, where the bottom particles are larger than the top particles. Solid lines represent the bottom layer, and dashed lines represent the top layer. In the first case (15 μm over 15 μm), the top layer is lifted higher than the bottom layer throughout the test domain (red curve). With an increase of particle size in the bottom layer (black and green curves), particles from both layers experience stronger dispersion behavior, and the bottom layer becomes more dispersed than the top layer at later stage. Nevertheless, there is always a region near the shock wave, where the top layer is lifted higher than the bottom layer in all three cases. Compared with our previous results, the larger particles from the bottom layer are dispersed more easily in these thinner cases, since less amount of dust from the top layer is now involved in suppressing the entrainment of the bottom particles.

Figure 5.29 shows the dust lifting heights for the three simulation cases in the second test series. Here, the top layer has a larger particle size than the bottom layer. In these cases, there are less interactions between the top and the bottom layer. Larger particles from the top layer are always lifted higher than the smaller particles from the bottom layer. With an increase of particle size in the top layer, the top dust becomes

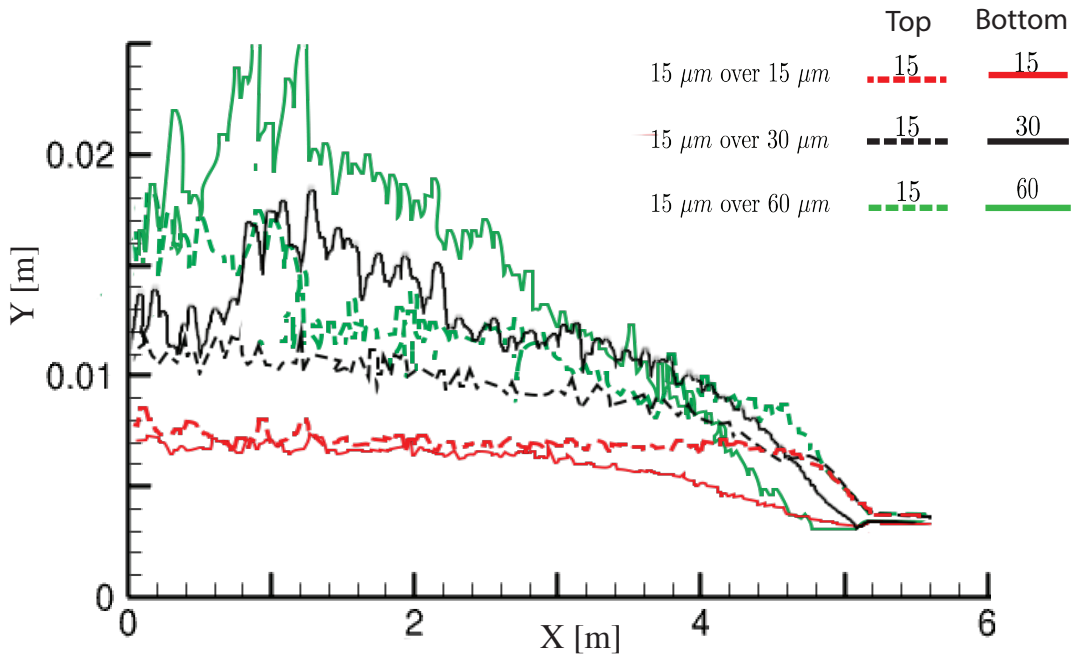

Figure 5.28: Dust lifting heights for the first test series. Dashed lines indicate top layer, and solid line indicate bottom layer.

more dispersed while the bottom dust remains at low level.

5.4.3 Rock Dusting in Coal Mines

In this section, the effect of rock dusting in preventing and reducing the coal-dust dispersion and explosion is explored. The rock dust is assumed to be 15 μm and 2680 kg/m^3, and the coal dust is assumed to be 30 μm and 1330 kg/m^3. (These parameters we provided courtesy of Marcia Harris and Michael Sapko of NIOSH).

5.4.3.1 Dispersion of 1 mm Rock Dust on 4 mm Coal Dust

The computed results of a shock passing over a layer of 1 mm rock dust placed on top of a layer of 4 mm coal dust is shown in Fig. 5.30. The top two images in Fig. 5.30 show the particle volume fractions for the coal and rock dust on a log scale. The bottom

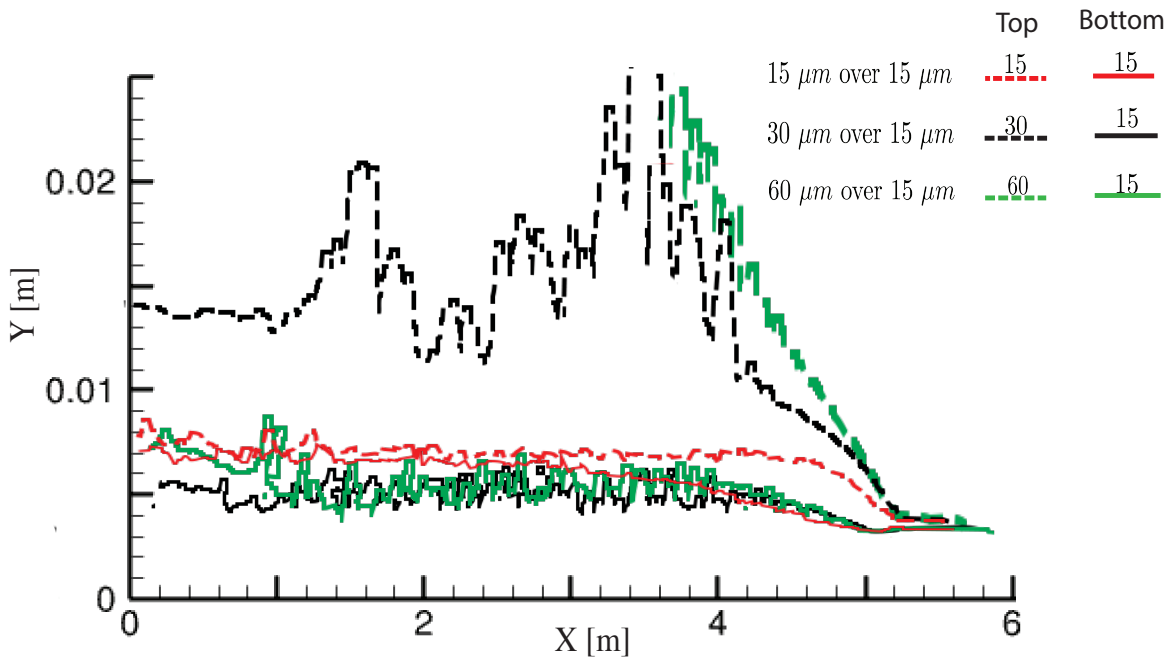

Figure 5.29: Dust lifting heights for the second test series. Dashed lines indicate top layer, and solid line indicate bottom layer.

image in Fig. 5.30 indicates the location of coal and rock particles. Here, particles with a volume fraction less than 0.005% are not shown. Figure 5.30 shows that the coal and rock particles are mixed with each other in most of the dispersed region, and there is no apparent separation between the two types of particles. In the area closer to the moving shock wave (400 $\sim$ 600 cm), however, the entrained dust is primarily rock dust (blue region). This is because dust lifting from the top layer begins immediately behind the propagating shock wave, and there is a delay in dust lifting from the bottom layer. In the rest of the region (0 $\sim$ 400 cm), the coal particles are lifted slightly higher than the rock particles, even though they were initially placed in the lower level. This result is consistent with earlier results that larger and lighter particles are lifted higher than smaller and heavier particles [2].

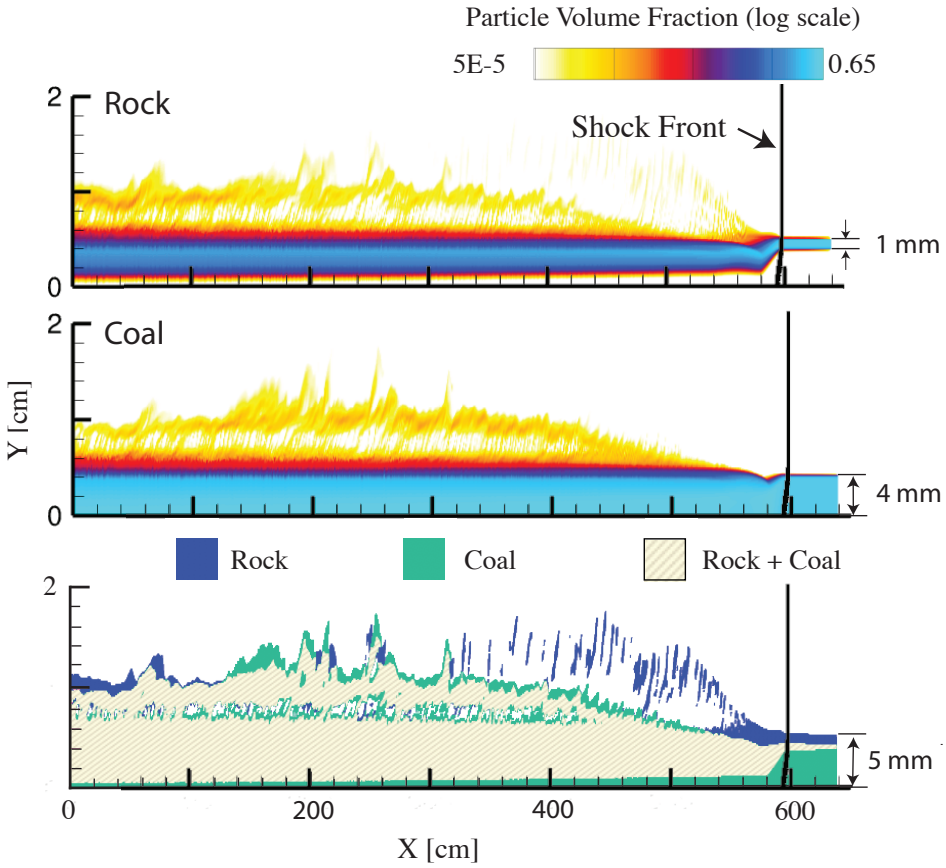

Figure 5.30: Simulation results of a Mach 1.4 shock passing over 1-mm rock layer on top of 4-mm coal layer. The top two image show the particle volume fraction contour of the rock and coal particles. The bottom image indicates the location of each type of particle.

5.4.3.2 *Effect of Rock-Layer Height*

Here, the effect of the rock-layer (upper layer) thickness on dispersion of a 4-mm coal layer (lower layer) is examined. Rock-layer heights of $h_2 = 1$, 2, and 3 mm are considered. The computed rock-dust concentrations for all the three cases are shown in Fig. 5.31 with the edge of the coal particles indicated. Here, blue indicates a coal-dominate region, while red indicates a rock-dominate region. The results show that the coal dust from the lower layer rises more slowly with increasing rock-layer thickness in the upper layer. In addition, the rock dust in the upper layer also becomes less dispersed with increasing rock-layer thickness. In the first case ($h_2 = 1$ mm), rock particles have a concentration close to or less than 50% in most of the dispersed region and coal particles are lifted to a similar level as the rock particles. In the second case ($h_2 = 2$ mm), the rock particles are more dispersed than the coal particles, and rock particles dominate in the dispersed region with a concentration ranging from 60% to 100%. In the last case ($h_2 = 3$ mm), the dispersed dust consists of primarily rock particles and the coal dust is hardly lifted. In this case, the 80% total incombustible content (TIC) requirement is achieved in most of the dispersed region.

5.4.3.3 *Dispersion of Three Dust Layers*

As the mining face advances, the coal particles generated fall on top of the applied rock dust, forming a system containing multiple stratified rock and coal layers. Here, the case of a Mach 1.4 shock passing over three dust layers is examined. The initial configuration is shown in Fig. 5.32, where the top and bottom layers contain coal particles and the middle layer contains rock particles. The three layers have thicknesses of $h_1 = 4$, $h_2 = 3,$ and $h_3 = 1$ mm. The other parameters remain the same as the previous calculations.

The computed particle volume fractions for the rock and coal particles and the

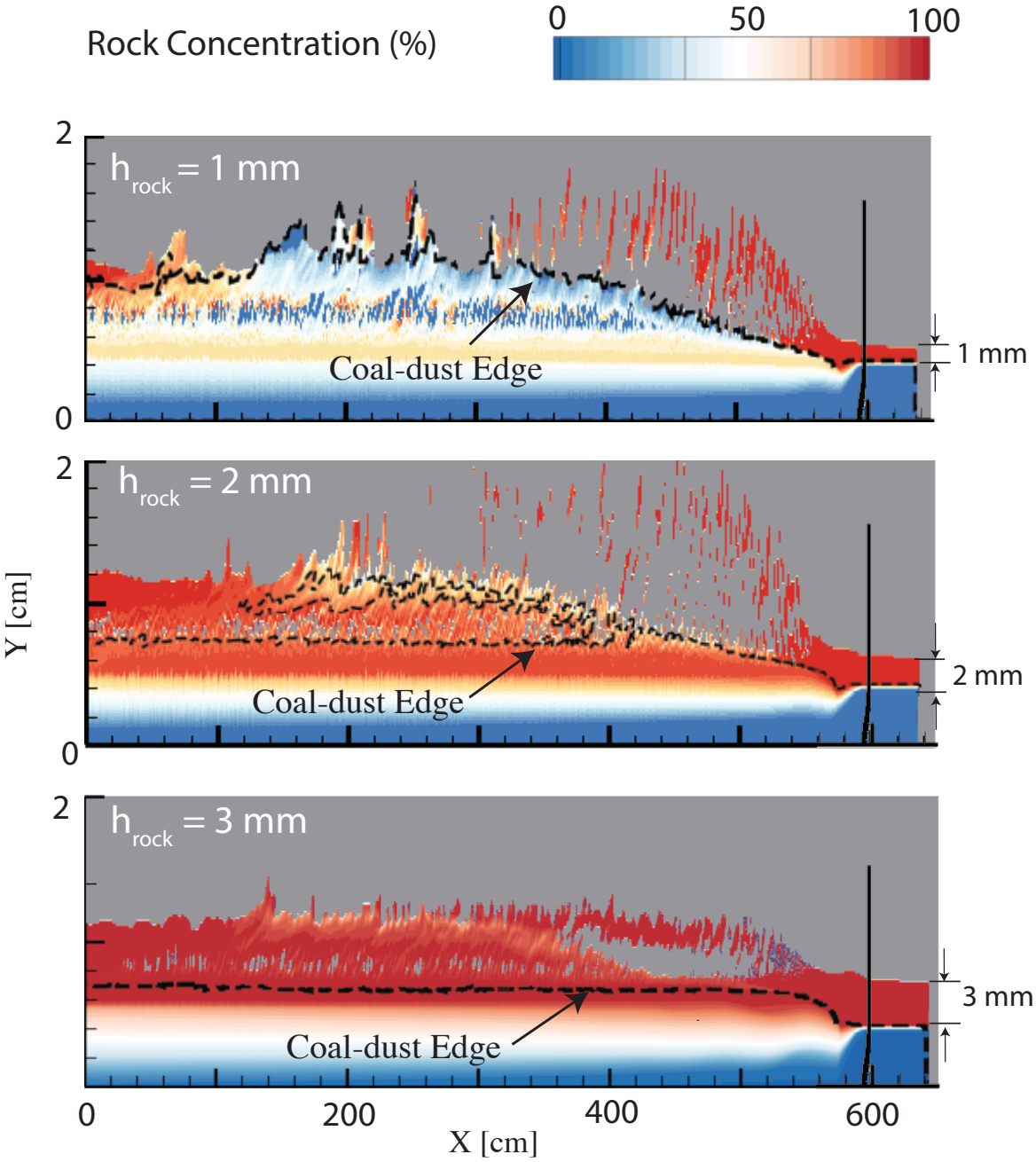

Figure 5.31: Computed rock concentrations for rock-layer thicknesses of $h_2 = 1$, 2, and 3 mm. The location of the dispersed coal dust edge and the propagating shock wave are indicated. The coal-dust layer remains at 4 mm for all cases.

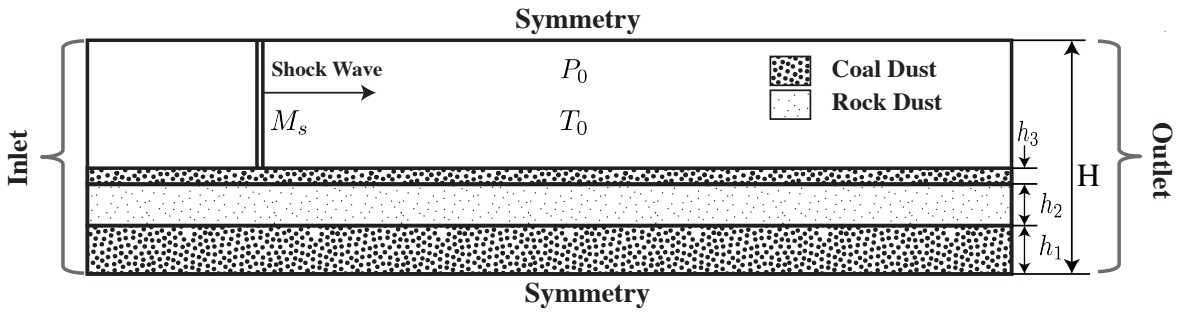

Figure 5.32: Schematic diagram of the initial conditions for the two-dimensional simulations where a shock of stregth M_s travels over three dust layers. The top and the bottom layers consist of coal particles, and the middle layer consists of rock particles.

rock concentration are shown in Fig. 5.33. These figures indicate that the coal dust rises more rapidly than the rock dust, and the rock particles underneath the thick layer do not suppress dispersion of the coal-dust layer on top. In fact, only particles from the top part of the dust layer are lifted. The coal particles from the bottom layer (0∼4 mm) are barely dispersed. The rock concentration suggests that coal particles dominate in the dispersed region.

5.4.4 Discussions

Thus the simulations have shown us that when there is a layer of large particles under a layer of small particles, the large particles may be lifted higher than the small particles. This interesting result is not always true, and can vary depending on the relative sizes of the particles and the thickness of the layers. Now we examine why this is happens.

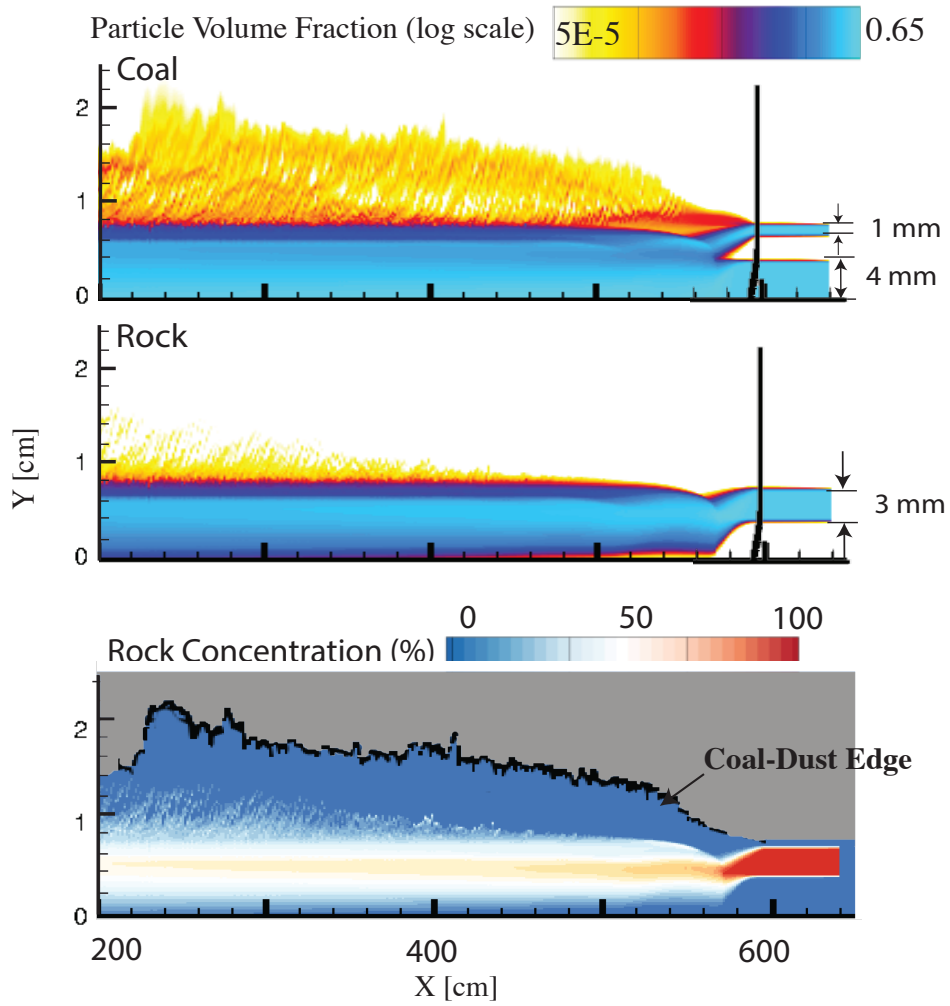

Figure 5.33: Computed particle volume fractions of coal and rock dust and rock concentration for the case of a shock passing over three dust layers. The location of the shock wave and the edge of the dispersed coal dust are indicated in the rock concentration contour.

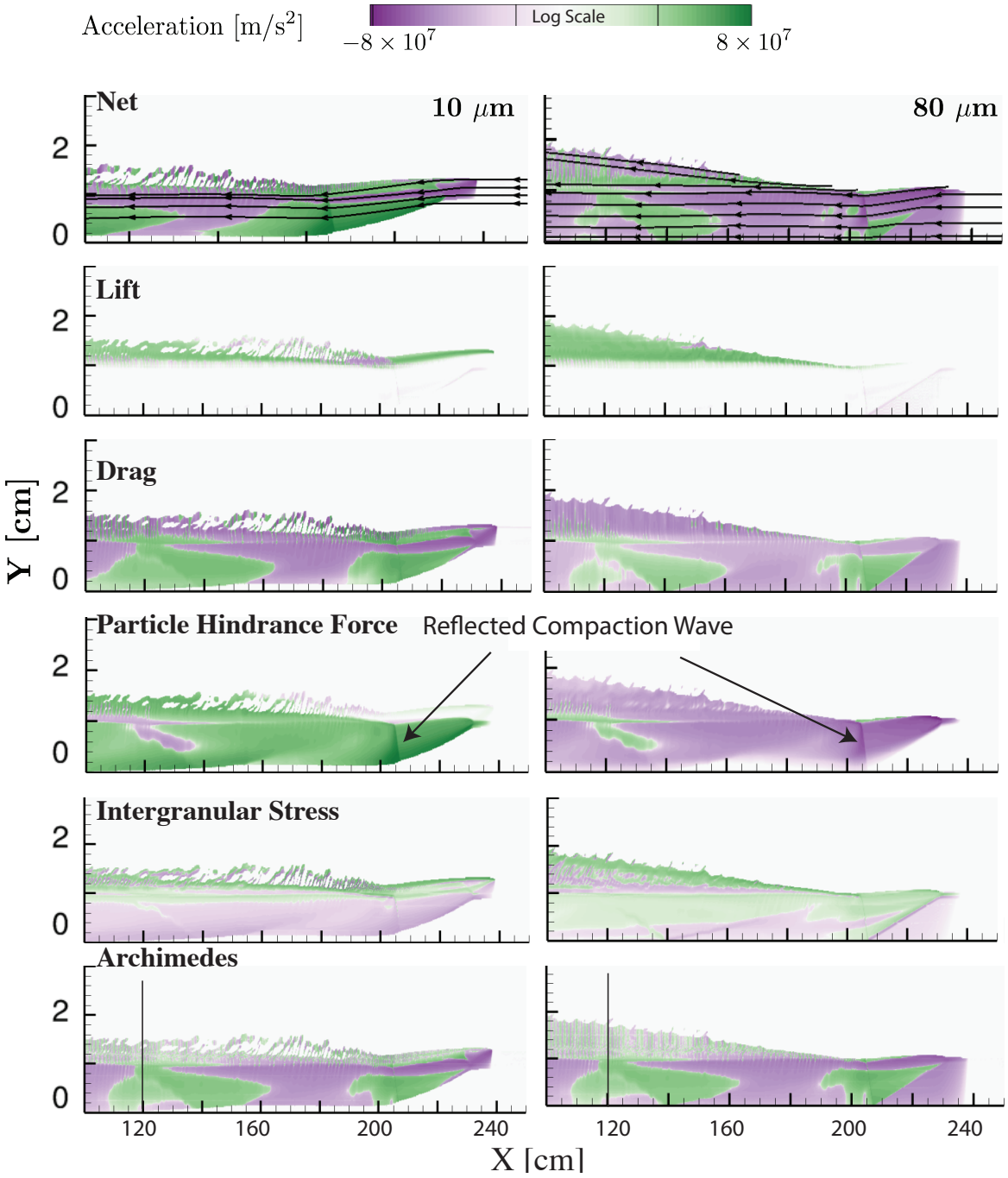

Figure 5.34: Vertical accelerations and accelerations due to drag, Archimedes force, lift, particle hindrance force, and intergranular stress for both types of particles. Forces have been normalized by $\alpha_s \rho_s$. The particle streamlines, and the location of the reflected compaction wave are indicated.

5.4.4.1 *Analysis of the Effect of Particle Size*

First, we examined the case where a 2.7-mm thick layer containing 10 μm particles is placed on top of a 10-mm layer containing 80 μm particles. The results indicated that the larger particles are much more dispersed than smaller particles, even though the larger particles were originally placed at a lower position. To help understand the mechanism, the governing forces (Table 5.1) acting on each particle type are evaluated. Figure 5.34 shows the net vertical acceleration and the accelerations due to lift, drag, particle-hindrance force, intergranular stress, and Archimedes force for the top and the bottom layer in the region between $X = 100$ to 240 cm. The particle streamlines in the shock reference frame are overlaid on the net acceleration for each layer.

Initially (just behind the shock), the surface of the top dust layer is lifted slightly due to the positive lift and intergranular stress forces. This minor lifting effect is soon overcome through the negative Archimedes and drag force from the gas flow acting on the top layer, and no apparent lifting is observed in the region just behind the shock ($200 \sim 240$ cm). These compression forces push the top layer into the bottom layer and form a mixed region (overlapping area in the third image in Fig. 5.25). During this compression and mixing process, particles from the top layer develop a larger downward vertical velocity (sharper slope for the particle streamlines) than particles in the bottom layer. Therefore, the particle hindrance force produces a negative force on the bottom layer while exerting positive force on the top layer. This effect reduces the velocity difference between the larger and the smaller particles, and this, in turn, slows down the mixing process.

At later stages, the dispersion of particles in the mixed region is enhanced by the interaction of the reflected compaction wave (marked in Fig. 5.34) and the surface of the compacted dust layer [68]. Dispersion of particles from both top and bottom layers are observed, with the 80-μm particles in the bottom layer lifted higher than the 10-

μm particles from top layer. During the lifting process, the bottom layer experiences a negative particle-hindrance force from the top layer. This effect, however, is not very significant in the dispersed region, since the top layer (10 μm) is hardly lifted.

The dust-lifting process in the mixed region is similar to what was seen in earlier studies [2], where a shock passed through a layer of dust containing two types of uniformly mixed particles. These prior results suggested that larger particles are lifted higher than smaller particles mainly due to the differences in lift force and drag forces. This is also true for the two-layer case simulated here, since the dispersion occurs after the two dust layers mix with each other. Figure 5.35 shows the accelerations due to lift and drag forces acting on the two particle types along a vertical line located at X = 120 cm. The 80 μm particles have a larger positive lift force that pushes them upwards and a smaller negative drag force pushing them downwards than those acting on the 10 μm particles. This explains why the 80 μm particles are lifted higher than the 10 μm particles.

Test cases with systematically increased particle size in the top layer (10, 20, and 40 μm) and fixed particle size in the bottom layer (80 μm) suggest that the top layer works more effectively in suppressing lifting in the bottom layer when the two types of particles are closer in size. The drag force, which is inversely proportional to the particle size, pushes on the top layer. This force is smaller for case III (40 μm) than for case I (10 μm) in Fig. 5.26. Therefore, the mixing and compression effects become weaker for cases where the top layer contains larger particles. In addition, a smaller size difference indicates a smaller solid packing limit ($\alpha_{s,max}$) and lower particle concentrations in the mixed region. As a result, the mixed particle region in case III in Fig. 5.26 contains fewer larger particles from the bottom layer than in case I, and the smaller particle on top of the larger particles now effectively suppress lifting of the larger particles. When the particle size in the top layer is further increased to approximately 80 μm, the bottom layer is

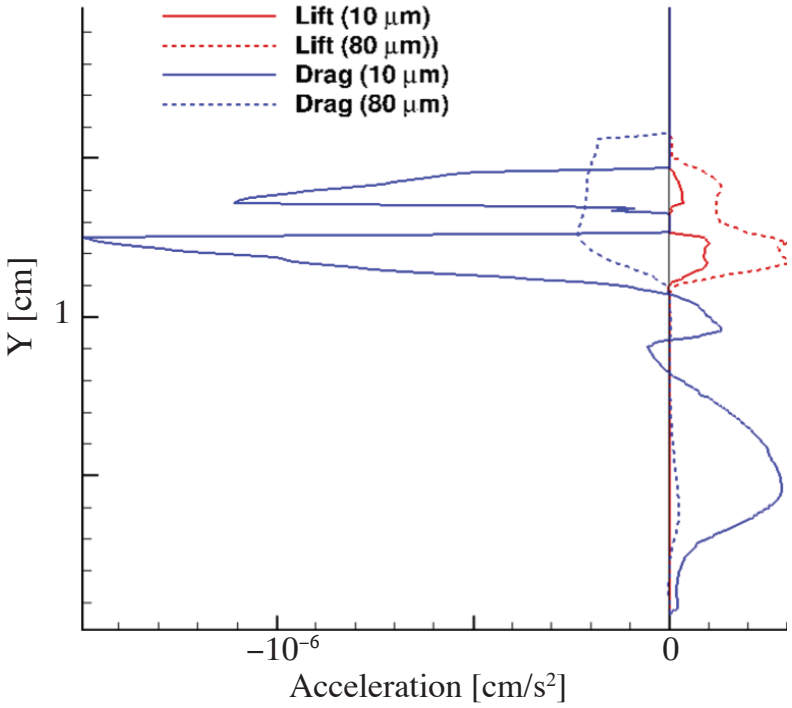

Figure 5.35: Accelerations due to lift and drag forces acting on the two types of particles along the vertical line at X = 120 cm.

even more suppressed. This trend is supported by prior simulations of a shock passing over a single dust layer containing particles with uniform size and density. According to Ugarte et al. [69], the particles inside of the dispersed region are mostly from the surface of the dust layer, and particles in the bottom part of the layer are hardly lifted.

5.4.4.2 Analysis of Rock- and Coal-Dust Dispersion

In Section 3.2, we explored dust dispersion behind a moving shock where a thin layer of rock dust is applied on top of a thicker layer of coal dust. Here, the rock particles are smaller and denser than coal particles. According to our previous conclusions, coal particles are lifted higher by a shock than rock particles. Ideally, to keep the coal dust from rising and igniting, we need two conditions to be fulfilled: rock particles from

the upper layer should suppress the coal particles from the bottom layer, and the rock concentration in the dispersed region should be greater than 80% [9].

The results shown in Fig. 5.30 and 5.31 suggests that a relatively thick (3 mm) rock-dust layer is required to suppress lifting of the underlying coal-dust layer. The coal particles begin to rise after the reflecting compaction wave interacts with the surface of the dust layer through positive intergranular stress and lift forces. This lifting behavior is then opposed by the negative particle hindrance effect. When an increasing amount of rock dust is applied, the positive intergranular stress (pressure-like effect on the granular particles) within the coal dust layer decreases, since the coal dust now has a lower granular energy due to interparticle collisions and friction. In addition, with more rock dust applied to the top layer, the dispersed coal particles experience a larger negative particle hindrance force, which suppresses the lifting. This explains why coal particles are more suppressed with a thicker rock-dust layer on top. The particle hindrance force also causes the coal-dust layer to rise more rapidly with decreasing rock-dust thickness. For the first case in Fig. 5.31, the coal particles underneath exert a large positive particle hindrance force on the rock particles above them during the dispersion process. For the case where $h_2 = 3$ mm, the positive particle-hindrance effect is less important, since the coal particles are now dispersed to a much lower height than the rock particles.

During the mining operation, more coal particles are generated and form another coal-dust layer on top of the applied rock-dust layer. Thus there are three layers: coal on top of dust on top of coal. Similarly, the coal particles from the top layer are pushed into the rock and coal layer underneath. In fact, the two coal-dust layers mix with each other after the compression and mixing stage. The coal dust from the upper layer, which is larger in size and smaller in density, rises quickly just behind the moving shock wave and before the mixing stage begins. This rapid dispersion of coal dust suggests the need to simultaneously or regularly applying rock dust during the mining operation.

5.4.4.3 Effect of Grid Resolution

The above simulations are performed with 5 levels of refinement, which gives a 156 μm for minimum cell size. For most of the cases shown above, this provides adequate grid resolution to capture the dust-lifting motion. For simulation cases where the dust layer is very thin (Section 5.4.2.3), however, the 0.32-mm top layer is resolved by only two computational cells along the vertical direction, and this coarse mesh could bring errors to our results.

To resolve this issue, we have considered increasing the level of refinement. With 6 levels of refinement, the dust layer can be better resolved with more computational cells. Nevertheless, there usually are grid limitations for Eulerian KTGF granular models. In such models, there needs to be an adequate number of particles within a computational cell so that we can treat the particle phase as a continuum. Here, with 6 levels of refinement, the finest grid considered is close to the particle size, and the assumption of granular continuity is challenged. This is a well-known quandary for any typical Eulerian-Eulerian models.

The simulation results of Case II in the first test series (15 μm over 30 μm) and Case III in the second test series (60 μm over 15 μm) discussed in Section 5.4.2.3 (cases of very small layer thickness) with 5 and 6 levels of refinement are shown in Fig. 5.36 and Fig. 5.37. In general, 5 levels of refinement works well for cases where the top layer is slightly dispersed (e.g., 15 μm over 30 μm in Fig. 5.36). For the cases where the top layer has a strong dispersion behavior in early stage (e.g., 60 μm over 15 μm in Fig. 5.37), 6 levels of refinement needs to be considered. Studies on the appropriate grid resolutions to capture the features of dust layers under the granular continuum assumption for thin dust layers are recommended as future work.

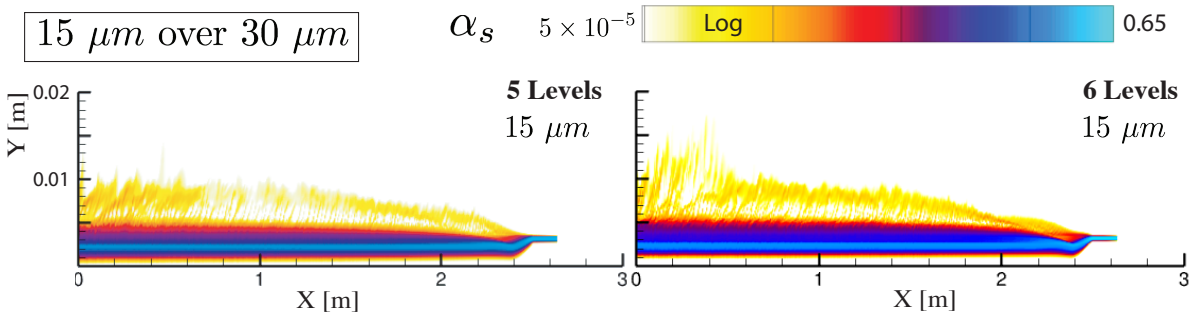

Figure 5.36: Particle volume fraction of the top layer (15 μm) for the 15/30 μm case with both 5 and 6 levels of refinement.

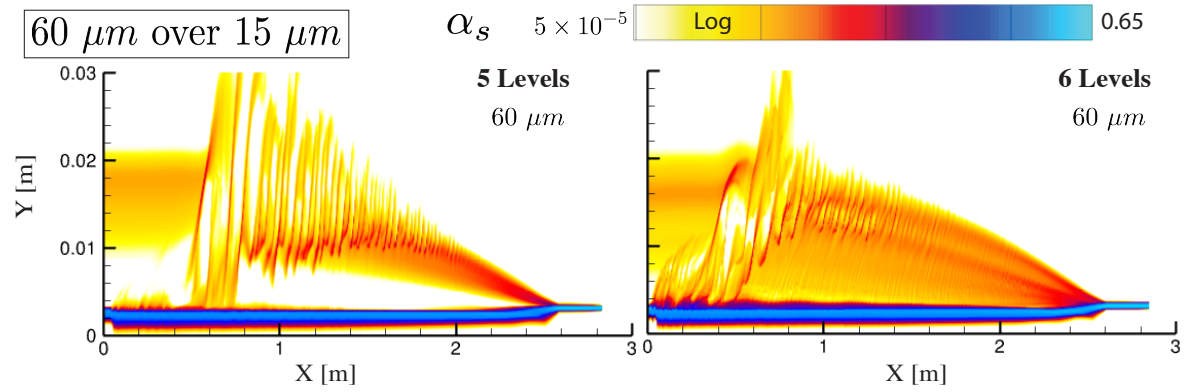

Figure 5.37: Particle volume fraction of the top layer (60 μm) for the 60/15 μm case with both 5 and 6 levels of refinement.

5.5 Summaries and Conclusions

Simulations to explore the dispersion of dust layers behind a moving shock wave were performed using a multi-fluid granular model based on KTGF. The model accounts for multiple particle types with a binning approach, where each bin of particles has its own characteristic uniform particle size and density. Solving the equations for a granular mixture containing one gas phase and M particle types involves solving (M+1) unsteady, multidimensional sets of conservation equations. Equations for each bin of particles are

coupled with the gas flow as well as all other particle types.

5.5.1 Shock Interacting with a Particle Cloud

One-dimensional simulations of a Mach 1.4 shock passing through a dilute particle curtain containing multiple particle types are performed to study how different types of particles behave with the interaction to a shock wave. The 1D results indicate that particles with different sizes or densities behave differently under the same background gas-flow conditions and they can separate into different clouds even though they were initially uniformly mixed with each other. Particles with larger inertia require a longer relaxation time to the post-shock condition and therefore are accelerated more slowly than particles with smaller inertia. Such separation phenomenon is not observed in cases with high initial particle volume fractions.

5.5.2 Shock Passing Over Single Dust Layer

The two-dimensional results of a shock passing over a dust layer containing two types of particles show that larger particles are lifted higher than smaller particles, while lighter particles are lifted higher than heavier particles. Larger particles near the shock experience a smaller drag force pushing the particles into the dust layer and a smaller lifting force pulling the particle out of the dust layer. Particle size plays a significant role on dust dispersion behind a moving shock, while particle density only has a minor effect.

5.5.3 Shock Passing Over Stratified Dust Layer

The two-dimensional results of a shock passing over two dust layers containing two different types of particles show that the larger particles comprising the lower layer can be lifted higher than the smaller particles from the upper layer when the two types of

particles have relatively large size difference. With an increased particle size in the top layer, the compaction and mixing between the two dust layers becomes less significant, and the top layer becomes more dispersed while the bottom layer becomes less dispersed.

Dust dispersion of stratified rock- and coal-dust layers was also investigated, where the coal particles are 30 μm and 1300 kg/m^3, and the rock particles are 15 μm and 2680 kg/m^3. Here, a thin rock layer was placed on top of a thicker coal-dust layer and rock-layer thicknesses of 1, 2, and 3 mm were considered. The results indicate that the coal dust rises more slowly with increasing rock-layer thickness placed on top of it, and a 3-mm thick of rock dust is needed to meet the 80% total incombustible content requirement. In addition, simulations of a case with three dust layers, coal on rock on coal, shows that coal particles from the top layer are much more dispersed than the rock particles underneath. This result shows the need to apply the rock dust continually during the mining operation.

Chapter 6

SUBSURFACE EXPLOSIONS IN COMET REGOLITH

6.1 Introduction and Background

Small bodies, such as comets or asteroids, which have been in existence from the era of planetary formation, are important for the study of the history and evolution of the solar system [89]. Now, they are reachable for observations. By studying their material compositions, more information can be obtained on the composition of the early solar system and the possible source of organic material brought to Earth.

One important aspect of the study of asteroids, comets, moons and planets is the physics of the granular media covering their surfaces. Exploration of these bodies often involves landing vehicles on the surface, excavating the surface regolith, or constructing structures on it, all of which require dealing with interactions between gaseous flows and dust particles. Here we define a granular medium as a collection of rigid, macroscopic particles with interstitial gas. This intermediate material phase has properties of both a solid and a fluid and exists everywhere in the universe. It covers a wide range of scenarios, from piles of sugar or nuts, to sand on a beach, to the collection of dust

particles in the asteroid belt [13]. For example, the compacted sand on the beach can behave as a solid, while the sand in an hourglass flows like a liquid. The ambiguous, transitional behavior of granular matter makes predictions fascinating and challenging.

In this chapter, we are interested in an excavation process that could be used to explore the regolith composition of an unknown asteroid or comet. One approach to obtaining regolith samples is from impact on the surface for the body. For example, the Deep Impact (DI) mission on 4 July 2005 delivered an impact of 19 GJ of kinetic energy and collided with the comet 9P/Tempel 1. The 366 kg impactor collided with the comet and produced a cratering event that ejected particles from the interior of the comet [90]. The composition differences between the interior and the surface of the comet were determined by measuring the spectra above the surface before and after the impact[91]. On 12 November 2014, the Philae lander ejected from the Rosetta spacecraft landed on comet 67P/ Churyumov-Gerasimenko (78P). The impact excavated about 0.4 m^3 of solid material from the regolith, and the ejecta from the impact were collected and analyzed [92].

Another approach to obtaining subsurface material is to create a subsurface explosion that drives material to the surface where it can be collected. Investigating this possible scenario is part of the motivation of the work done in this work. Although this has not yet been attempted, possibilities for using this approach in the future are now being investigated. Effecting this approach, however, requires knowledge of the behavior of explosions in embedded in granular material, and to date, there is relatively little work in this area relevant to asteroids and comets.

6.1.1 Comet Regolith

Currently, very little is known about the precise atmospheric or material conditions on any specific comet. We do, however, have some information about the range of

conditions. This range can be deduced from knowledge of the orbit, observations from flybys, and analyses of returned samples.

The temperature on a comet is largely dependent on its location in solar orbit and the size of the orbit around the sun, and therefore it varies from comet to comet. Halley's Comet is closer to the sun and has a relatively short period. Its surface temperature has been estimated as approximately 350 K when it is close to the sun [93]. Comets farther from the sun have much lower temperatures. Hale-Bopp, for example, is estimated to have an average temperature of around 25 – 45 K [94]. Comets in solar orbits beyond the average distance of Pluto have even lower temperatures, usually less than 30 K [95].

Previous flybys performed remote spectroscopic and polarimetric observations from Earth. These observations suggest that cometary nuclei (that is, the solid core of the comet) consist of particles of high porosity and low density [96]. The solid particles in these nuclei, ranging from microns to millimeters, are mostly composed of refractory materials, such as silicates, organics, and amorphous carbon [97, 98]. Typical values of the density of the nuclei range from 100 to 2000 kg/m^3 [99]. For example, data collected from Rosetta's OSIRIS cameras show that comet 67P/ Churyumov-Gerasimenko has a density of 533 kg/m^3 with a high porosity to up to 86% [96, 100]. Moreover, data returned from the comet 81P/Wild2 suggest that the particles are a mixture of cohesive grains with sizes ranging from 5 to 25 μm [97]. Nevertheless, the sizes of the collected particles are questionable due to particle aggregation that occurs during the collection process. Data collected by the Rosetta spacecraft from comet 67P/ Churyumov-Gerasimenko show that particles are aggregates of smaller grains, ranging from a few hundred nanometers to tens of micrometers [101]. The dust aggregates imply that particles on comets are cohesive and can stick to one another after collisions.

6.1.2 Granular Shocks

The properties of shock waves in granular fluids are not as well-known as those of shock waves in gases. In a manner similar to the behavior of gas flows, a granular shock forms when a wave moves faster than the compaction wave speed, i.e., the local speed of sound in a granular fluid. In granular media, however, the sound speed is generally low (typically a few cm/s) compared with the 340 m/s sound speed in air at standard conditions [102]. Therefore, shock waves form more easily in a granular medium than in a gas-phase flow [103][104].

The formation of a shock wave driven by a piston moving in granular media has been studied by Goldshtein et al. [104] and Kamenetsky et al. [105]. Inelastic particle collisions near the moving piston results in a loss in granular temperatures and the particles collapse into clusters. The particle clusters, which completely lost their kinetic energy from the densely packed region, reach the packing limit. Next to the densely packed region is the fluidized region, which has lower packing and higher granular temperature. This region separates the densely packed region from the granular-shock front[104, 105, 106]. In front of the granular shock is the undisturbed region, where the granular properties remain unchanged.

According to Khmel' & Fedorov [107], there are two types of granular shocks: a type I granular shock has a discontinuity in gas-phase properties and a smooth relaxation in particle properties; a type II granular shock has a discontinuity in particle-phase properties, and a weak discontinuity in gas-phase properties is driven along with the granular shock. In both cases, the granular motions are initiated by the gas-phase blast wave [107]. Houim and Oran [1] found that a type I granular shock forms when the granular mixture is dilute ($\alpha_s \sim 10^{-4}$). In these cases, the blast wave propagates through the particles and is slowed down slightly due to drag between gas and particles. The granular properties vary smoothly in a relaxation zone, where no sharp discontinuity

is found. A type II granular shock forms in cases with a higher initial α_s, and the intergranular stress ($p_{s,tot}$) can be substantial due to collisional and frictional effects. A type II shock is developed from a type I shock and it propagates with a higher velocity.

In this chapter, we would like to study the process of subsurface explosions in conditions similar to that on a comet using the proposed Eulerian-Eulerian multiphase granular model. Specifically, we are interested in the formation and propagation of shocks in granular media, and the effect of background temperature and granular packing on the explosion process.

6.2 RESULTS: One-Dimensional Spherical Calculations

The one-dimensional spherical shock-tube problem presented now is analogous to the case in which an explosive charge is buried infinitely deep in a granular mixture, ignited, and then expands. Presenting this simplified case helps explain the complex physics of the two-dimensional explosion in granular media that follows.

6.2.1 Physical Model

The initial setup is illustrated in Fig. 6.1 and input parameters for the model are summarized in Table 6.1.

$$p_g^L = 1.38 \text{ GPa}, \quad p_g^R = 10 \text{ Pa},$$
$$T^L = 4020 \text{ K}, \quad T^R = 100K,$$
$$\alpha_s^L = 0, \quad \alpha_s^R = 0.25.$$

The domain is 0.5 m in length and the diaphragm is placed at 0.02366 m. The

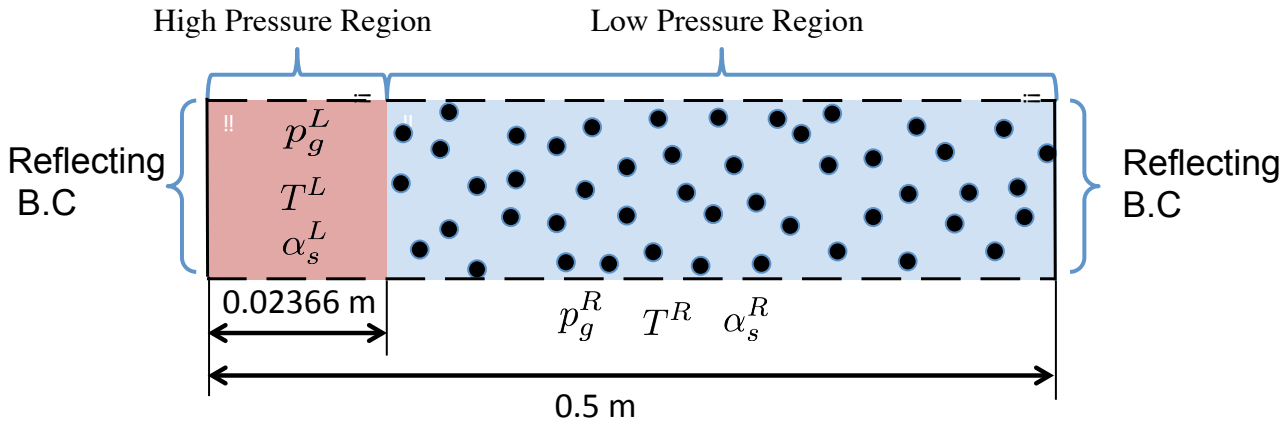

Figure 6.1: Initial setup for the 1D-spherical simulation.

Table 6.1: Initial parameters for particle and gas phases.

	Parameter	**Value**
Particle phase	Diameter (d)	1 μm
	Density (ρ_s)	2000 kg/m^3
	Volume fraction (α_s)	0.25 – 0.45
	COR (e)	0.01
	C$_{v,s}$	2000 J/K
Gas phase	Molecular weight	39.948 g/mol
	Ratio of specific heat (γ)	1.2

driving gas is on the left side of the diaphragm at 1.38 GPa and 4020 K. This size for the driving section corresponds to the amount of energy stored in 90 g of TNT, which is the amount that will be used in the two-dimensional simulations discussed below. The driven section of the tube consists of gas flow at 10 Pa and 100 K and a particle phase at a volume fraction of 0.25. The particle diameter, density, specific heat, and coefficient of restitution are 1 μm, 2000 kg/m^3, 2000 J/kg K, and 0.01 respectively. All of the gas in the test section is assumed to be Argon with a specific heat ratio of 1.2 and obeys the ideal gas law. The results described first were obtained using 800 computational cells and a second-order Godunov method, where the primitive variables are calculated using a parabolic reconstruction scheme with van Albada slope limiter. The solutions were advanced in time using a fourth-order Runge-Kutta algorithm with a CFL number of 0.5.

6.2.2 Granular Shock Formation and Propagation

Figure 6.2 summarizes the results of the computation by showing how the gas and granular-phase properties change in time. At each time shown, the front of the curve is the location of the granular shock and the back of the curve is the location of the contact surface, defined as the location where the gas flow first encounters the particles. Granular shocks are analogous to shocks in gas phase and are characterized by a discontinuity in pressure, temperature, and bulk density. The particles move radially and accumulate to form a region between the contact surface and the granular shock, where they approach the packing limit. The size of this densely packed region grows with time as the particles continue moving outwards. The maximum particle volume fraction decreases gradually due to spherical expansion.

As the granular shock moves through the system, it collects more and more particles and as a result, the gas-phase velocity decreases with time (Fig.6.2(c)). At the

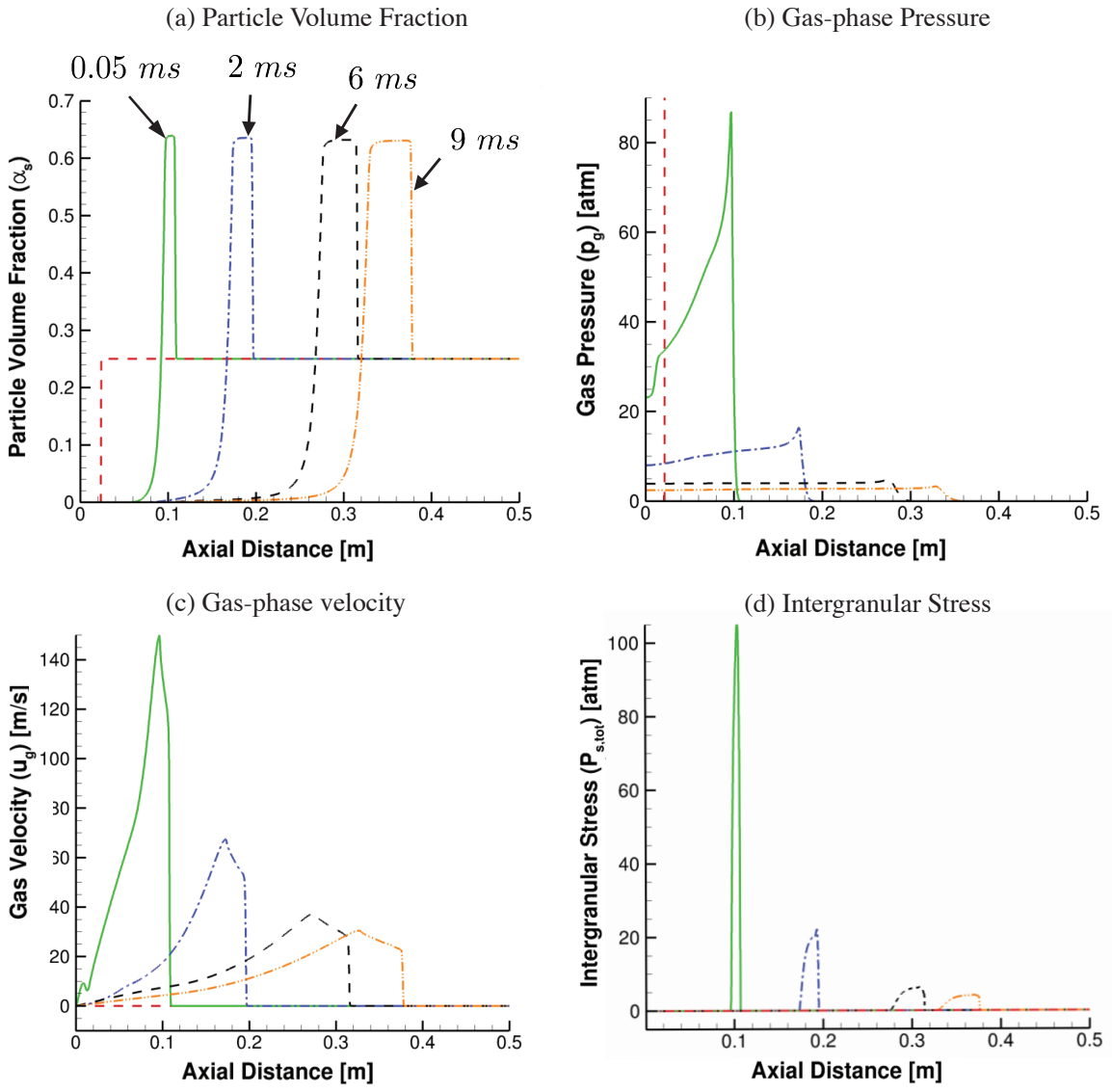

Figure 6.2: Computed (a) particle volume fraction, (b) gas-phase pressure, (c) gas-phase velocity, and (d) intergranular stress for an explosion in 1d spherical coordinate at 0 ms, 0.05 ms, 2 ms, 6 ms, and 9 ms.

contact surface, the gas-phase velocity increases due to a nozzling effect, characterized by a sudden increase of particle volume fraction and a reduction of gas-phase volume. This nozzling effect also increases the gas-phase pressure significantly near contact surface (Fig. 6.2(b)). Then the velocity is further decreased in the densely packed region. By comparing the profiles of the particle volume fraction with those of the gas-phase pressure and velocity, we find that the granular shock travels with the gas-phase shock. This implies that after the granular shock is formed, it is no longer driven by the gas-phase flow.

Figure 6.2(d) shows the intergranular stress ($p_{s,tot}$) as a function of position at various times. The intergranular stress in the particle-phase is analogous to pressure in gas-phase flow. It comprises solids pressures (p_s) and frictional-collisional pressures (p_{fric}), Eq. (3.12)$\sim$(3.22). In this case, the frictional-collisional pressure dominates the intergranular stress, since the particle collisions are highly inelastic (low coefficient of restitution $e = 0.01$). The frictional-collisional pressure is active only when α_s is greater than 0.5 and remains zero otherwise [1]. This explains why the intergranular stress decreases and approaches zero behind the granular shock. The frictional-collisional pressure is included as a part of the intergranular stress so that the packing does not go beyond a maximum limit, $\alpha_s = 0.65$.

6.2.3 Effect of Grid Refinement

Tests of the effects of varying the computational cell sizes are shown in Fig. 6.3. The computed granular-shock radius is shown as a function of time in a logarithm scale. According to the Taylor blast wave theory and the two-dimensional simulations that will be shown below, the radius of the granular shock grows logarithmically in time with a slope of 0.4 (see Section 6.3 below). Figure 6.3 shows that the computed results converge to this value of the slope as the resolution is increased.

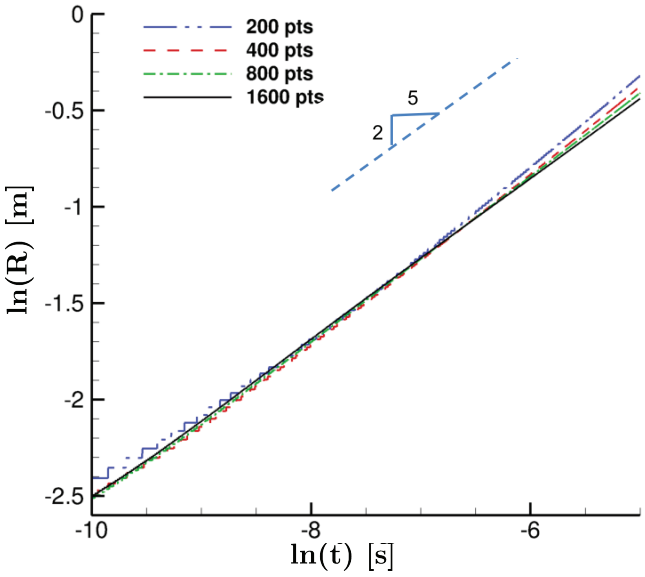

Figure 6.3: Computed results of granular-shock radius as a function of explosion time in logarithm scale. The explosion charge is equivalent of 90 g TNT. Simulations are performed with 200, 400, 800, and 1600 computation cells.

6.3 RESULTS: Two-Dimensional Axial-Symmetrical Calculations

6.3.1 Physical Model

The general initial conditions in the computations are based on the information about comets summarized above. Input parameters for the model are summarized in Table 6.1, and the initial setup is illustrated in Fig. 6.4. The material below the comet surface is assumed to be a granular fluid, which consists of a mixture of gas and particles. The particles are modeled as spherical solid particles with a density of 2000 kg/m^3, a diameter of 1 μm, and a specific heat capacity ($C_{v,s}$) of 2000 J/K. The specific heat capacity is assumed to be a constant value throughout the simulations. The coefficient of restitution (COR) of the particle phase, e, determines the elasticity of the collision,

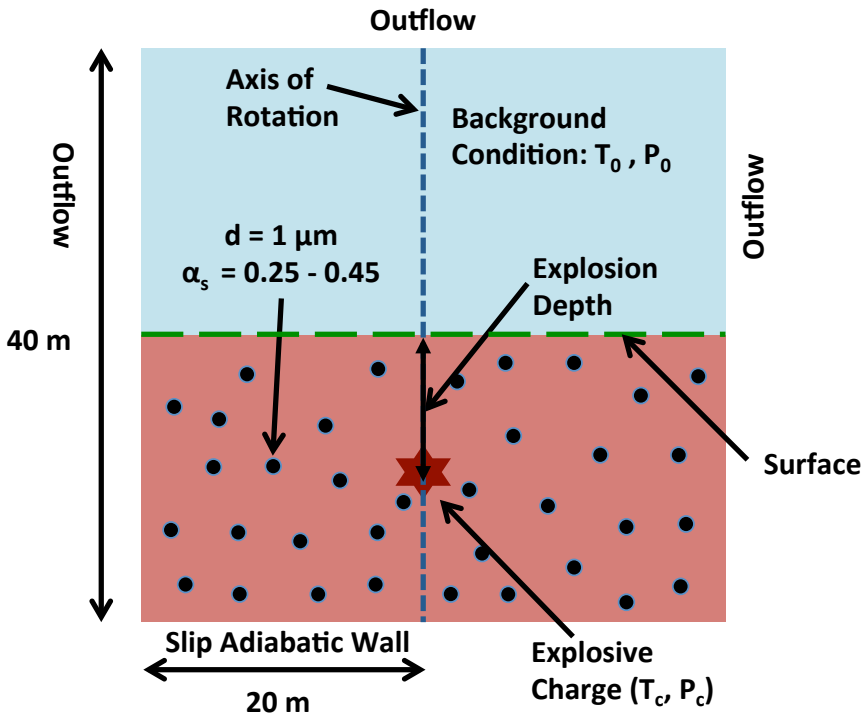

Figure 6.4: Initial conditions for the two-dimensional simulations.

and is unity for fully elastic and zero for plastic collisions. At the comet surface, we assume $e = 0.01$, which means that the material on the surface is cohesive and tends to stick together after collisions. The material above the comet surface is assumed to be pure gas at 10 Pa and a temperature ranging from 10 – 100 K. The explosion is initiated by placing a charge under the surface. The charge, which is equivalent to 90g of TNT, is marked by the star in Fig. 6.4 and modeled by a pocket of gas at 1.38 GPa and 4020 K. The gas-phase flow in the simulation is assumed to follow the ideal gas law and has a molecular weight equivalent to Argon, which simulates high molecular weight explosive products. The gas-phase specific heat ratio is 1.2. The computational domain is 20 m wide, 40 m high, and rotationally symmetric about the dashed line. The bottom side of the domain is assumed to be a symmetry plane, where slip wall, adiabatic boundary conditions (B.C) are applied.

In the simulations presented here, the explosion depth, the particle volume fraction, and the background temperature are varied in order to understand the effect of shocks and explosions originating at different locations under the comet surface.

6.3.2 Cavity Formation and Venting in an Explosion

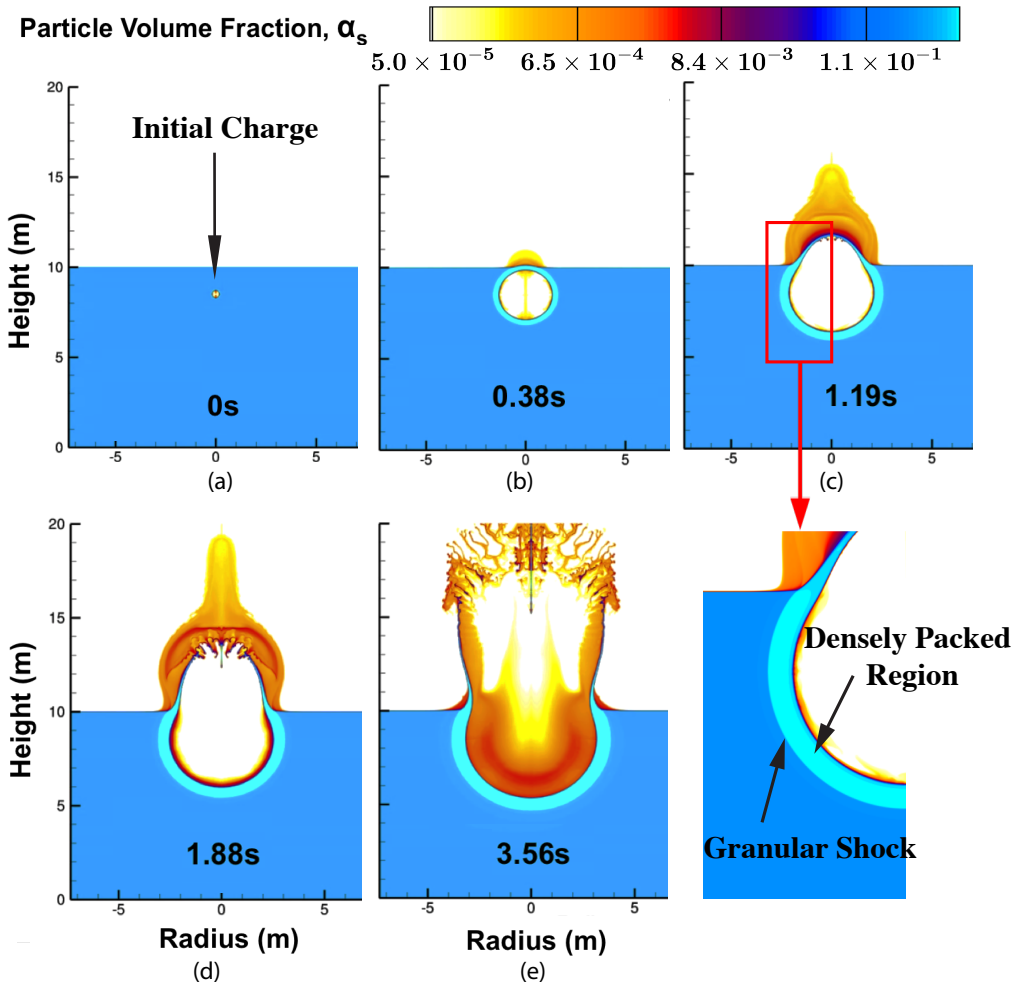

Figure 6.5: Time sequense of particle volume fraction contours showing the evolution of cavity formation during an explosion initiated 1.5 m below the regolith surface.

Figure 6.5 shows a series of particle volume fraction contours at selected times for an explosion initiated 1.5 m below the comet regolith surface. The initial particle volume fraction below the surface is 0.25 and the background condition is 100 K and

10 Pa. The initial location of the explosive charge is marked on the 0 s contour. The explosive material, modeled by high-temperature and high-pressure gas, expands radially and creates a spherical cavity. The particles near the expanding gas begin to move as a result of the interaction with the shock wave generated by the explosion [103]. The moving particles form a cavity, which expands radially with time. Similar to the 1D spherical simulation, a densely packed region is formed while the particles are moving and accumulating. At the front edge of the dense region, there is a granular shock. In addition, some of the particles are entrained and ejected from the surface before the granular shock has reached the surface (Fig. 6.5b). The cavity expands due to the high pressure produced by the energy released [108]. As this cavity expands, the outside particles are compressed and a granular shock forms in the regolith. A cap-like structure forms when the volume fraction of the particles approaches the packing limit (Fig. 6.5c). At 1.88 s, the cap breaks as a result of the gases expanding and venting into the atmosphere. The high-pressure gas and some particle ejecta fly upwards (Fig. 6.5d). Some of the ejecta escape because their velocity exceeds the escape velocity of the comet, and others fall back into the crater.

6.3.3 Structures of Granular Shocks

Figure 6.6, which shows the volume fraction of the particle phase and the flow properties along a radial line, illustrates the structure of a granular shock and how the flow properties change in the vicinity of a granular shock. The results are shown at 0.52 s for a case in which the initial explosion depth is 3 m. The granular shock, the contact surface, and a radial line are marked in Fig. 6.6a. The particle volume fraction, gas velocity, particle velocity, and the intergranular stress along the radius are shown in Fig. 6.6b. The granular shock is located at around 1.85 m, where there is a sharp discontinuity in particle volume fraction. The contact surface is located at 1.5 m.

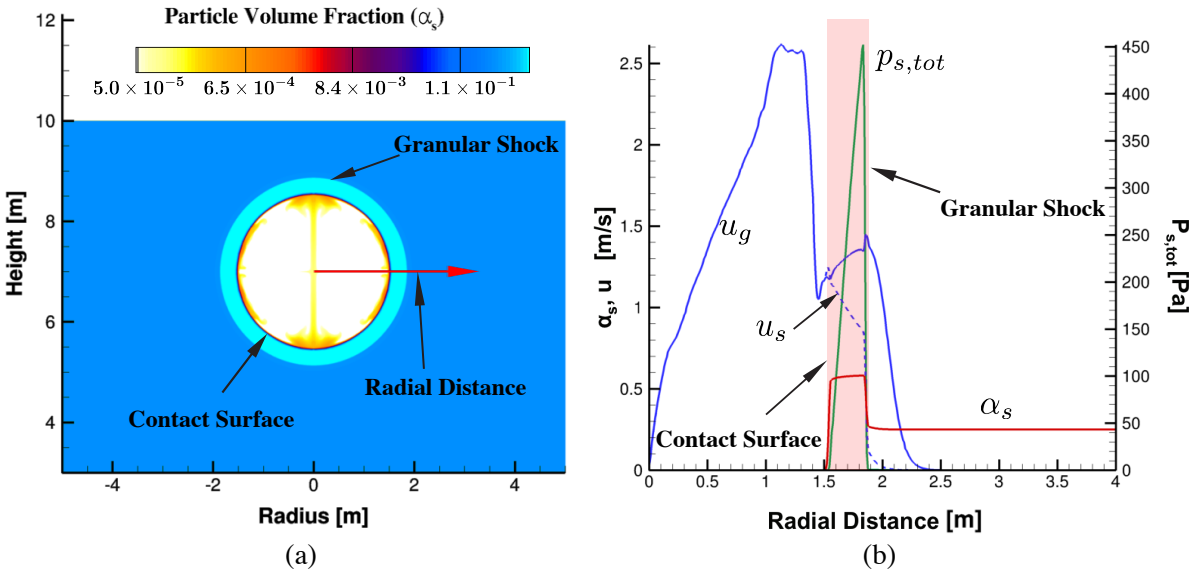

Figure 6.6: Computed results of an explosion initiated 3 m below the surface at 0.52 s: (a) Particle volume fraction contour, and (b) particle volume fraction (α_s), gas velocity (u_g), particle velocity (u_s), and intergranular stress ($P_{s,tot}$) along the radial line. The granular shock and the contact surface are indicated.

The results in Fig. 6.6b show similar trends as those in Fig. 6.2 for the 1D spherical simulation. There is a region where the particles accumulate and approach the packing limit (shaded area in Fig. 6.6b). This region, which is located between the granular shock front and the contact surface, corresponds to the light blue ring in Fig. 6.2a. The gas-phase velocity decreases notably near the contact surface and then increases in the granular mixture. There is also a small increase in gas velocity at the granular shock. The particle velocity is the greatest near the contact surface and is decreasing across the densely packed region. Similar to a gas-phase shock, there is a sharp discontinuity in particle velocity across the granular shock. By comparing the gas-phase and the particle-phase velocities, we find that the gas motion leads the granular motion in this case. The intergranular stress, which is the sum of the solids and friction pressures, given in Eq. (11–13), reaches 450 Pa near the granular shock. The intergranular stress is active only between the contact surface and the granular shock and approaches zero everywhere else.

6.3.4 Propagation of Granular Shocks

Now we examine the affect of the particle volume fraction on the propagation of a granular shock. Figure. 6.7(a), shows the radius of the shock as a function of time for an explosion initiated 3 m below the surface with three different initial particle volume fractions, $\alpha_s = 0.25$, 0.35, and 0.45. The radius of the cavity, i.e., the contact-surface radius, is shown in Fig. 6.7(b) for comparison.

The radius of both the granular shock and the contact surface grow logarithmically. At a higher particle volume fraction, the granular shock propagates faster, which is opposite of what is expected in a gas. The slopes of all of the profiles in Fig. 6.7a, however, remain the same. The granular-shock radii as a function of time for all three cases are given by:

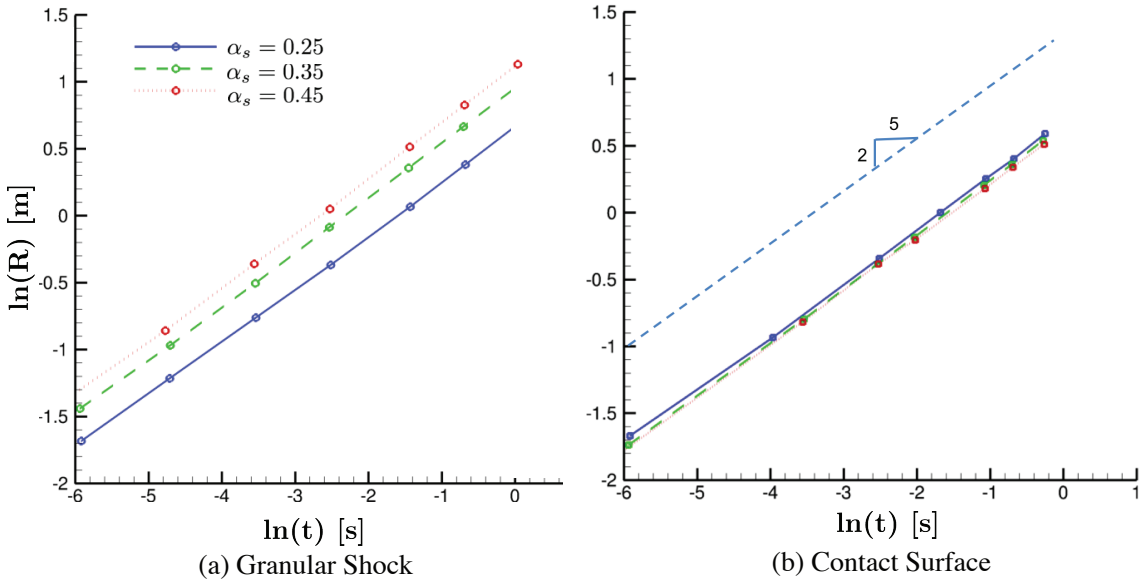

Figure 6.7: Computed results of (a) granular-shock radius, and (b) contact-surface radius as a function of time in logarithm scale of an explosion initiated 3 m below the regolith surface. Three different initial particle volume fractions ($\alpha_s = 0.25$, 0.35, and 0.45) are tested and the results are shown in logarithm scale.

$$\ln(R_{\text{shock}}) = \begin{cases} 0.3995\ln(\text{t}) + 0.6612, & \alpha_s = 0.25 \\ 0.4053\ln(\text{t}) + 0.9459, & \alpha_s = 0.35 \\ 0.4074\ln(\text{t}) + 1.1006, & \alpha_s = 0.45. \end{cases} \tag{6.1}$$

The contact surface radii for $\alpha_s = 0.25$, 0.35, and 0.45 almost overlap with each other and is given by:

$$\ln(R_{\text{contact}}) = 0.4004\ln(\text{t}) + 1.9065 \tag{6.2}$$

These expressions indicate a R $\sim t^{0.4}$ power law for both the granular shock and the cavity radius. This is consistent with the work done by Taylor [109] to describe the spherical shock wave propagating outwards as a function of time.

6.3.5 Effect of Background Temperatures

Figure 6.8 compares contours of particle volume fraction at 4.0 s for an explosion initiated 1.5 m below the comet surface at three different background temperatures, 10 K, 50 K, and 100 K. The temperature dependence of the granular explosion is especially important since there is significant variation in comet surface temperature depending on the where the comet is in its orbit. In addition, the temperature varies wildly depending on locations where the explosion occurs on a comet. The night-side temperatures can be much lower than the day-side temperatures on a comet.

At a lower background temperature, the explosion time is increased and fewer particles are entrained by the gas flow. In Fig. 6.8(a), the cap of the cavity breaks, and particles and high-pressure gas are ejected while in Fig. 6.8(c), the cap structure remains intact.

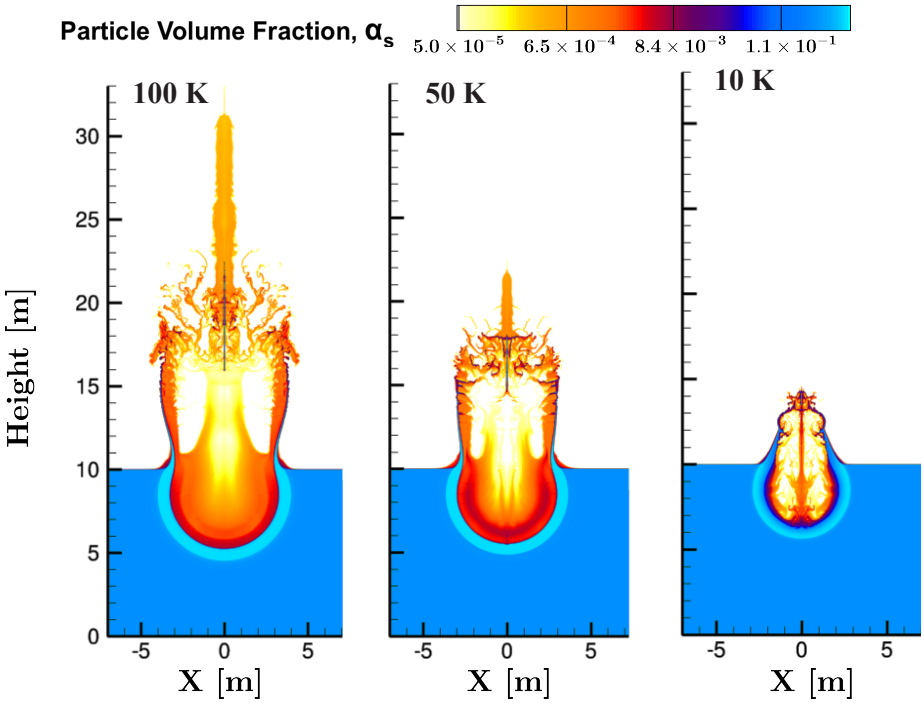

(a) 100K (b) 50K (c) 10K

Figure 6.8: Computed particle volume fraction contour of an explosion initiated 1.5 m below the surface at 4.00 s with a background temperature of (a) 100 K, (b) 50 K, and (c) 10 K.

6.3.6 Effect of Grid Refinement

Numerical resolution tests have been performed with 7, 8, and 9 levels of refinement, corresponding to the minimum cell size of 17.36 mm, 8.68 mm, and 4.34 mm. The computed results for particle volume fraction contours of an explosion initiated 3 m below the surface are shown in Fig. 6.9 for all three grid resolutions at 0.31 s. For these resolution tests, the amount of the explosive charge was increased from 90 g TNT to 1688 g TNT, since the grid at 7 levels of refinement is too coarse to represent the original charge. For 1688 g TNT, the initial charge can be represented by 4x4, 8x8, and 16x16 cells for the 7, 8, and 9 levels of refinement. At a higher level of refinement, more detailed structures inside of the cavity can be seen. For a finer grid, the cavity radius

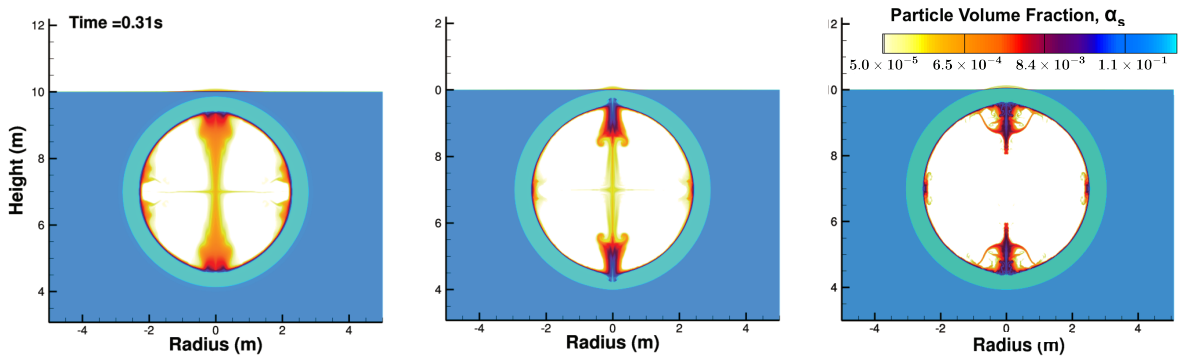

(a) (b) (c)

Figure 6.9: Computed results of an explosion initiated 3 m below the surface at 0.31s. The explosion charge is equivalent to 1688 g TNT. Simulations are performed with a (a) 7, (b) 8, and (c) 9 levels of refinement.

is slightly larger than that of a coarser grid. The overall motions of the granular media, however, converge with increasing grid resolution.

6.4 Discussions

6.4.1 Granular Shock Formation

In both the 1D and the 2D simulations presented above, we found type II granular shocks, where there is a sharp discontinuity in particle-phase properties, such as particle volume fraction (α_s) and particle velocity (u_s). The gas-phase shock formed by the high-pressure gas enters the granular mixture and initiates the particle motion. The gas-phase velocity (u_g) is increased due to the nozzling effect at the contact surface (Fig. 6.2(c) & Fig. 6.6(b)). Similarly, the granular shock compresses the gas as it propagates outwards and produces an increase in gas pressure and velocity. This weak gas-phase discontinuity is driven by the granular shock and propagates along with it [1, 107].

The gas-phase velocity (u_g) leads the particle-phase velocity (u_s) in Fig. 6.6(b).

This implies that by the time the granular shock reaches the regolith surface, some gas-phase flow has already passed through the surface. Particles are entrained and ejected above the regolith surface in Fig. 6.5(b) due to the resultant gas flow and not the granular shock.

For cases with higher particle volume fractions, more momentum is needed for the gas phase to initiate and accelerate particles [110]. Therefore, it takes longer for an initial granular shock to form. This process, however, is completed within a very small time scale and is not captured in Fig. 6.7. For a higher α_s, more energy is transferred from the gas phase to the particle phase, and a larger intergranular stress pushes the particles with a higher velocity.

6.4.2 Granular Shock Propagation

Both the granular-shock radius and the contact-surface radius exhibit a power law relation with explosion time (Fig. 6.7(a)(b)), which can be written as:

$$R = At^{\beta}, \tag{6.3}$$

or

$$\ln(R) = \ln(A) + \beta \ln(t). \tag{6.4}$$

where R is the radius, t is the simulation time, A and β both are constants. From Fig. 6.7, the slope of the curve is 0.4, indicating a constant value of $\beta = 0.4$.

This power law is consistent with the work done by Taylor [109] in order to describe the spherical shock wave propagating outwards as a function of explosion time. According to Taylor, the formation of a blast wave by an explosion in air with $\gamma = 1.4$ can be written as [109]

$$t = \frac{2}{5} R^{\frac{5}{2}} (B\rho_0)^{\frac{1}{2}} E^{-\frac{1}{2}} = 0.926 R^{\frac{5}{2}} \rho_0^{\frac{1}{2}} E^{-\frac{1}{2}}. \tag{6.5}$$

Rewriting the equation in logarithmic form:

$$\ln(R) = 0.4\ln(t) + 0.2\ln(E) - 0.2\ln(\rho_0) - 0.4\ln(0.926), \tag{6.6}$$

where E is the energy of the explosion and ρ_0 is the atmospheric density.

The exponent in Taylor's equation is 0.4, which is very close to the results of our simulations for both the granular shock and the contact surface radius. This exponent is independent of particle compaction, but is a function of dimension of the calculation. For an explosion in a purely gas-phase flow, the shock propagation speed is faster when the density is lower. For a purely particle-phase system, the shock propagation speed behaves differently. The Rankine-Hugoniot conditions for a purely granular system can be expressed as:

$$\begin{cases} \alpha_{s,1}\rho_s u_{shock} = \alpha_{s,2}\rho_s(u_{shock} - u_{s,2}) \\ p_{s,2} - p_{s,1} = \alpha_{s,2}\rho_s u_{s,2}(u_{shock} - u_{s,2}) = \alpha_{s,1}\rho_s u_{shock} u_{s,2} \\ p_{s,2}u_{s,2} = \alpha_{s,1}\rho_s u_{shock}(\frac{1}{2}u_{s,2}^2 + e_{s,2} - e_{s,1}), \end{cases} \tag{33}$$

where state 1 and 2 refer to the upstream and downstream conditions of the shock. Assuming the particle velocity is zero upstream of the shock, and the intergranular stress is $p_{s,tot} = p_{fric}$ downstream and zero in upstream condition. The shock velocity for the system is [20]:

$$u_{shock} = \sqrt{\frac{\alpha_{s,2}}{\alpha_{s,2} - \alpha_{s,1}} \frac{p_{fric}(\alpha_{s,2})}{\alpha_{s,1}\rho_s}} = \sqrt{\frac{p_{fric}(\alpha_{s,2})\alpha_{s,2}}{-\rho_s(\alpha_{s,1} - \frac{\alpha_{s,2}}{2})^2 + \frac{1}{4}\alpha_{s,2}^2\rho_s}}. \tag{34}$$

For a fixed downstream condition (constant $\alpha_{s,2}$), the granular shock velocity has a minimum value at $\alpha_{s,1} = \frac{\alpha_{s,2}}{2}$ and will increase with a lower or higher surrounding density ($\alpha_{s,1}$).

The expression for the shock velocity in purely particle-phase system provides insights into why the granular shock in the two-phase mixtures travels faster with higher surrounding densities (α_s =0.25, 0.35, and 0.45). Based on eqn (34), for dense granular

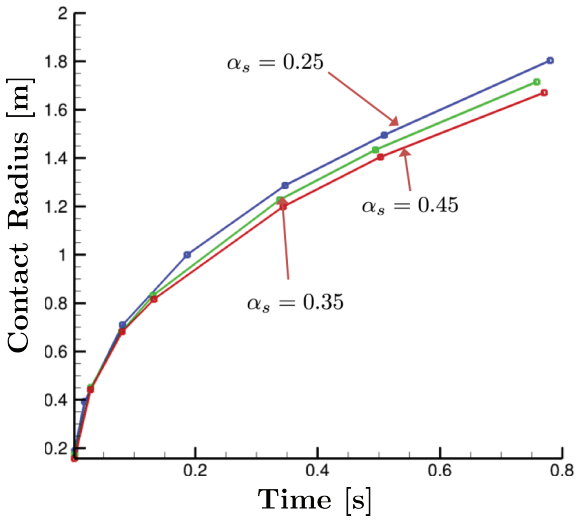

Figure 6.10: Computed results of contact surface radius as a function of time of an explosion initiated 3 m below the regolith surface. The results are shown in linear scale.

regions where the particle volume fraction α_s is greater than $\frac{\alpha_{s,2}}{2} = 0.29$ ($\alpha_{s,2} \sim 0.58$ is the post-shock particle volume fraction in 2D simulations), the granular shock velocity becomes greater with increasing compaction. The granular shock velocity for $\alpha_s = 0.25$ should be close to the shock velocity for $\alpha_s = 0.35$. In our simulations, however, the granular shock velocity for $\alpha_s = 0.25$ is notably smaller than that for $\alpha_s = 0.35$. This can be due to the particle-gas interaction that was not taken into account in the purely particle-phase system. For granular mixtures with a higher particle volume fraction, more energy from the gas-phase flow can be transferred to the particle-phase pseudo thermal energy. This results into a larger intergranular stress, which accelerates the particles faster.

The contact-surface radius as a function of time is essentially independent of particle volume fraction, as shown in Fig. 6.7. This is because the particle motion near the contact surface is dominated by Archimedes Force ($-\alpha_s \nabla p_g$) and drag from the high-pressure flow. The acceleration rate of particles due to Archimedes force and drag force is less dependent on the initial compaction than it is due to the intergranular stress.

It should be noted, however, there are slight differences among these cavity expansion rates. Fig. 6.10 shows the contact-surface radius as a function of time on linear scale for the same case. The results suggest that the granular-gas mixtures with a higher compaction expand somewhat more slowly.

6.4.3 Effect of background temperatures

The influence of background temperatures on a granular explosion comes from the temperature dependence of the speed of the pressure wave. There are two sound speeds in the calculation, one for the gas phase and one for the granular phase. The wave speed c_g for an ideal gas is determined by

$$c_g^2 = \gamma \frac{p_g}{\rho_g} = \gamma R T_g, \tag{6.7}$$

where γ is the specific heat ratio. Therefore, the acoustic wave speed in the gas phase is temperature dependent and slower at lower background temperatures.

The compaction wave speed for a granular medium, c_s, analogous to the acoustic wave speed for a real gas, is calculated assuming the particles are in vacuum. It only depends on the particle volume fraction (α_s), and the granular temperature (θ_s), assuming constant particle density (ρ_s) and critical particle volume fraction ($\alpha_{s,crit}$) [1]. Therefore, the granular sound speed has no dependence on the temperature.

As a result, the gas-phase flow in Fig. 6.8(a) is travelling with a higher speed due to the higher acoustic wave speed. The results show that the gas-phase flow is faster than particle-phase flow at 100K. The gas flow in this case entrains particles ahead of the granular shock and the explosion range is enlarged. At lower temperatures, the acoustic wave speed is reduced while the granular compaction wave speed remains almost the same. In Fig. 6.8(c), the gas-phase flow travels slower than the granular shock. Fewer particles are entrained by the gas flow and we see a much more compact structure.

6.5 Summaries and Conclusions

This chapter presents one- and two-dimensional numerical simulations of subsurface explosions in granular material typical of the surface of comets and asteroids. The numerical model solved multiphase problem of surface gas and subsurface granular material consisting of a particle-gas mixture. Two unsteady, multidimensional sets of conservations equations, one for the compressible gas and one of the granular material are coupled through appropriate source and sink terms [1]. This formulation has been shown to be valid for a wide range of particle volume fractions.

The explosive charge, buried in the granular medium, was modeled by high-pressure and high-temperature gas. The initial conditions were based on an estimate of subsurface conditions on a comet. An initial 1D spherical calculation in which an explosive charge was buried infinitely deep in a granular mixture shows the properties of a granular shock. Then a series of 2D simulations examined the effect of background temperature and showed the properties of the shock breaking the surface. In the 2D simulations, the charge was buried 3 m and 1.5 m below the surface, and the background temperatures and the particle volume fractions varied in the ranges of 10 K to 100 K and 0.25 to 0.45.

The simulations showed the process of a granular shock formation and propagation as a blast wave is created during an explosion. The blast wave initiates the particle motion and the particles accumulate to form a granular shock. The granular shock, in turn, produces a weak gas shock following it. As the granular shock expands, it compresses the granular material and forms a cap-like structure and finally the cap breaks with particles and gas ejected outwards. There is a power law that relates the granular-shock radius and the contact-surface radius with the explosion time: $R \propto t^{0.4}$, which is consistent with the results found by Taylor for 3-D spherical shock waves.

For denser granular flows, the intergranular stress becomes stronger and it propagates the granular shock with a higher velocity. The contact-surface radius profile, however, remains almost unchanged regardless of the particle concentrations. In addition, the exponent of the power law for both the granular-shock radius and the contact-surface radius remains constant for various compactions. At a lower background temperature, the explosion time scale is increased and the particles move in a slower and more compact motion.

Chapter 7

CONCLUSIONS, DISCUSSIONS, AND RECOMMENDATIONS

In the last chapter, we will first give an overview of this dissertation. Then we will summarize the technical results, discuss the major findings and contributions, and make suggestions for future study.

7.1 Overview

In this dissertation, efforts have been devoted to developing a multidimensional, multi-fluid model that can accurately describe the granular motions under high-speed compressible flow, and is valid for a wide range of granular packing. In addition, the model needs to account for multiple particle types to study particle segregation phenomenon within a granular mixture. We apply this model to two very different problems: dust dispersion in underground coal mines, and subsurface explosions in a comet regolith. By solving real-world problems, we have explored some interesting phenomena of granular flows, such as particle segregation, effects of particle size and density on dust entrainments, and formation and propagation of granular shocks. Understanding these

characteristics of granular flows helps us to develop more efficient methods to control the particle behaviors during an explosion.

7.2 Technical Summary and Major Contributions

7.2.1 Model Development

The KTGF granular model proposed in this dissertation is developed based on the prior work of Houim and Oran [1], and is generalized from a two-fluid model to a multifluid model. It solves the fundamental governing equations of fluid dynamics for a multidimensional gas flow coupled to a granular flow that consists of different particle types. Here, a binning approach has been adopted, so that particles in each bin have their own uniform particle type and diameter, and particles in different bins can have different velocities, temperatures, pressures, etc. The model is valid for granular mixture under high-speed flow over a wide range of granular packing and background flow conditions. Adaptive mesh refinement is implemented through either the Paramesh or Boxlib libraries, both of which handle parallel communications.

Increasing the number of particle types (# of bins) in the granular model increases the realism of the computations, but it also increases the computational expenses. Adding an additional type of particles brings a new set of governing equations for that particle phase. For a two-dimensional calculation of a shock passing over a dust layer containing two types of particles in a 10-m channel, 400 processors and 70 hours of computer time is needed on the University of Maryland deepthought2 supercomputer. This can be more expensive when a larger number of particle types are involved. There is, therefore, a tradeoff between the accuracy of the simulation and the computational cost.

7.2.2 Dispersion of Dust Layer Induced by Shock Waves

7.2.2.1 Shock Interacting With a Cloud of Particle Mixtures

We start to investigate the problem of shock-particle interactions with a simple one-dimensional calculation where a shock passes over a cloud of particle mixtures containing two or more types of particles. The question addressed in this section is: ***How do different types of particles behave with the interaction to a shock wave?***

Our results show that different types of particles can separate into different dust clouds even though they were initially mixed with each other. Particles with lower inertia (smaller Stokes number) are accelerated faster than particles with higher inertia, and this results in the particle segregation phenomenon. The separation is less significant in a dense particle cloud, where the particle hindrance effect and intergranular stress move the densely compacted particles as a group.

The separation process found in the 1D results indicates the necessity of modelling multiple particle types, since this effect cannot be captured using a single-sized particle model. Dividing the particles into different particle bins leads to more accurate results when the particle size or density in the dust varies greatly.

7.2.2.2 Size and Density Effects on Dust Lifting

Next, we studied the two-dimensional cases of a shock passing over a single dust layer containing different types of particles that were uniformly mixed. The fundamental question addressed in this section is: ***How do particle size and density affect dust lifting and particle segregation?***

The results show that larger and lighter particles tend to be dispersed to a greater height than smaller and heavier particles. The effect of particle density is less significant in comparison to the size effect.

Dust-lifting mechanism are also studied by evaluating the six governing forces acting on each type of particles. We find that drag and lift forces are the main reasons for the particle segregation phenomenon. Larger particles near the shock experience a smaller drag force pushing the particles into the dust layer and a smaller lifting force pulling the particles out of the dust layer. In real underground coal mines, the "unmix" of the inert particles from the reactive particles due to an initial blast wave could lead to secondary explosions.

7.2.2.3 Dust Lifting in Stratified Layers

In this section, we focus on a more realistic configuration: a shock passing over stratified dust layers containing different types of particles. We have shown in the previous section that particle size is the major factor influencing the level of particle entrainments, and larger particles are lifted much higher than smaller particles. Here, we ask: ***What will happen if we place a layer containing smaller particles on top of a layer containing larger particles?***

The evaluation of forces indicates that there are two stages in the lifting process, namely: a) the compressing and mixing stage, and b) the dispersion stage. During the first stage, the gas-phase pressure force and drag force push onto the top layer into the bottom layer, thereby compressing and mixing the two types of particles. In the second stage, the particles in the mixed region are dispersed, and the mechanism here is similar to that of the dispersion of two types of particles mixed in a single dust layer. The dust dispersion is enhanced by the interaction between the reflected shock wave and the surface of the dust layer.

(a) Effect of Particle Size

Our computed results show that larger particles in the bottom layer can be lifted

higher than smaller particles in the top layer if the two types of particles have relatively large size difference. With an increased particle size in the top layer, the compaction and mixing process becomes less significant, and the top layer becomes more dispersed while the bottom layer is less dispersed.

(b) Effect of Layer Thickness

The simulation results with varied thicknesses of the top layer show that the bottom layer becomes less dispersed with increasing top-layer thickness. If the top layer is very thick compared to the layers of dust underneath, only the top layer of dust is dispersed and the bottom layer is barely lifted. This is found to occur regardless of the densities or sizes of the dust particles from the upper and lower layers of dust.

7.2.2.4 Dispersion of Stratified Rock- and Dust-Layers

Here, we continue our study in real coal mine conditions, where stratified coal and rock dust layers are formed. Here, coal particles are assumed to be larger in size and smaller in density than rock particles. This study provides important information that can be used to determine how much inert dust is required to mitigate a dust explosion in coal mines.

(a) Rock Dust on top of Coal Dust

The simulation results show that placing a thin layer of rock particles on top of a thicker layer of coal particles fails to suppress the coal particles underneath from lifting. The coal dust underneath rises more slowly with increasing rock-layer thickness placed on top of it. Analyzing the inert particle concentration in the dispersed region suggests that a relatively thick rock dust (3 mm) is needed to meet the 80% total incombustible content requirement.

(b) Coal Dust on top of Rock Dust

We find that even a very thin layer of coal dust on top of an inert dust layer is

sufficient to produce a reactive particle cloud when dispersed by a shock wave. The inert rock dust underneath fails to suppress the coal particles on top of it from being dispersed. Simulations of a case with three dust layers, coal on rock on coal, shows that coal particles from the top layer are much more dispersed than the rock particles underneath. This indicates the need to apply the rock dust continually during the mining operations.

7.2.2.5 Effect of Grid Refinement

We are aware of some convergence issues in regions near the edge of the dispersed dust, where "particle streamers" (i.e. string-like clusters of high-concentration particles) are formed. In these dilute regions, there is usually insufficient number of particles within each computational cell and the assumption of granular continuity is challenged. As a result, these particle streamers are known to not converge under grid refinement using Eulerian-Eulerian methods.

By increasing the computational cell size, the particle phase can be better represented as a fluid. Nevertheless, this increased cell size may be too coarse to capture the features of gas flow or dust layer. This is especially obvious for cases with very thin dust layers (0.32 mm). In those cases, the 0.32-mm layer is resolved by only two computational cells along the vertical direction with 5 levels of refinement, and this coarse mesh fails to capture the entire dust-lifting behavior. Resolving this issue will likely require extending methods to include more advanced models of particle interactions, such as a quadrature-based moment technique, which allows particle trajectories to cross.

7.2.3 Subsurface Explosions in Granular Media

Next, subsurface explosions in granular media is studied with the proposed multi-fluid model. In this study, only one particle type is considered. The main purpose of this

work is to develop a better understanding of the explosion mechanism, the formation and propagation of granular shocks.

7.2.3.1 Cavity Formation and Venting

During an explosion, the explosive material, modeled by high-temperature and high-pressure gas, expands radially and creates a spherical cavity. As this cavity expands, the outside particles are compressed and a granular shock forms in the regolith. A cap-like structure is observed when the volume fraction of the particles approaches the packing limit. Finally, the cap breaks as a result of the gases expanding and venting into the atmosphere. The high-pressure gas and some particle ejecta fly upwards. Some of the ejecta escape because their velocity exceeds the escape velocity of the comet, and others fall back into the crater.

7.2.3.2 Formation of Granular Shocks

Granular shocks are analogous to shocks in gas phase and are characterized by a discontinuity in pressure, temperature, and bulk density. In this study, the formation of a granular shock is driven by the blast waves generated by the sudden release of the explosive charge. As the granular shock moves through the system, it collects more and more particles and as a result, the particle velocity decreases with time. After the granular shock is formed, the particles are no longer driven by the gas-phase flow but travels spontaneously instead.

7.2.3.3 Propagation of Granular Shocks

There is a power law that relates the granular-shock radius with the explosion time: $R \propto t^{0.4}$, which is consistent with the results found by Taylor for 3-D spherical shock waves. For denser granular flows, the intergranular stress becomes stronger and

it propagates the granular shock with a higher velocity. In addition, the exponent of the power law for the granular-shock radius remains constant at different particle compactions. At a lower background temperature, the explosion time scale is increased and the particles move in a slower and more compact motion.

The granular shock velocity for a pure granular system can be determined by performing a Rankine-Hugoniot analysis for the particle phase. The results suggest that the granular shock velocity reaches a minimum value when the initial packing is 0.29 for the simulations discussed in Chapter 6.

7.3 Recommendations for Future Work

The KTGF model described in this work neglects several terms (e.g. viscous stresses, granular energy exchange between different types of particles, dissipation of PTE due to collisions between different types of particles, phase changes). We have shown that these terms do not produce significant effects on the dust dispersion height , which is our major concern in this work. Nevertheless, incorporating these terms results in a more accurate representation of the granular motion, and can be important to our future study.

We are aware of some differences between our simulation results and the experiments. For example, we find that larger particles are dispersed to a greater height than smaller particles. As an apparent contradiction, the experiments done by Chowdhury *et al.* [71] show that smaller particles are lifted higher than larger particles. Understanding the reasons for this contradictory is our future work. Here, we provide a list of possible reasons for this inconsistency:

- The particle size in the simulations are not comparable with the actual particle sizes in the experiments. The dust sample used in an experiment has a size distribution while all particles in our simulations are assumed to have identical size.

- Agglomerations of particles in experiments have substantially increased the size of the dust sample during the lifting process. In our simulations, however, the agglomeration effect is neglected.

- There is inconsistency in time and length scales (i.e. where measurements are made with respect to the distance behind the shock) between simulations and experiments. In addition, the edge of the dispersed dust is defined differently in simulations and experiments.

- The representation of lift force (now modelled as the Magnus force) in our model may not accurately simulate the dust-lifting process. The effect of other lift forces such as Saffman force may needs to be evaluated.

In addition, the sensitivity of the solution to some of the parameters that describe the contributing forces can be evaluated. (For example, in a prior work, we looked at the effects of frictional pressure ($P_{fric,l}$), the collisional pressure ($P_{c,lm}$), and the solid-solid exchange coefficient (S_{coef}) on the simulation results [2].) Exploring all or some of these affects are topics of future work.

Another issue that arises is the validation of the Eulerian-Eulerian model in very dilute particle regimes. In principle, the Eulerian granular model is only valid when the granular continuity assumption holds. In dilute regimes (or for particle streamers, i.e. string-like clusters of high-concentration particles), this assumption is often challenged since there are insufficient number of particles within each computational cell. We have noticed some convergence issues near the edge of the dispersed dust particles. It would be useful to resolve this issue by extending methods to include more advanced models of particle interactions, such as a quadrature-based moment technique, which allows particle trajectories to cross.

The dispersion of multiple dust layers are complex processes that depend on many factors. In this work, we focused the effect of particle size and dust-layer thickness.

Other parameters, such as the shock wave Mach number, coefficient of restitution, and initial packing could also be very important. More importantly, developing a general correlation that could be used to predict the dust dispersal height as a function of these parameters (particle size, dust-layer thickness, Mach number, etc.) would be extremely useful to optimize the selection of rock-dust properties applied in a coal mine to prevent explosions.

Finally, there are relatively few laboratory scale experiments that can be used to validate these dust explosion calculations. Most experiments for the dust-lifting problem is very old and does not involve particle polydispersity or consider the segregation effect. No experiment has been documented on the dispersion of stratified dust layers. Therefore, there is a need for experiments to help understand the basic physics of dust dispersion and validate simulations. Moreover, some of the models used in this work contain empirical coefficients (such as C_{lift}, $\alpha_{s,crit}$), which needs to be determined and calibrated by experimental data.

Bibliography

[1] Ryan W Houim and Elaine S Oran. A multiphase model for compressible granular–gaseous flows: formulation and initial tests. *Journal of Fluid Mechanics*, 789: 166–220, 2016.

[2] Shuyue Lai, Ryan W Houim, and Elaine S Oran. Effects of particle size and density on dust dispersion behind a moving shock. *Physical Review Fluids*, 3(6):064306, 2018.

[3] U.S. Chemical Safety Board. West pharmaceutical services dust explosion and fire, 2004. URL `https://www.csb.gov/west-pharmaceutical-services-dust-explosion-and-fire/`. [Online; accessed February 9, 2019].

[4] Wikipedia. 2015 new taipei water park explosion, 2018. URL `https://en.wikipedia.org/wiki/2015_New_Taipei_water_park_explosion`. [Online; accessed February 9, 2019].

[5] Mining Awarness. Upper big branch mine disaster, 2010: 29 died on easter monday, 2013. URL `https://miningawareness.wordpress.com/2013/12/12/upper-big-branch-mine-disaster-2010-29-died-on-easter-monday/`. [Online; accessed February 9, 2019].

[6] Wikipedia. 2008 georgia sugar refinery explosion, 2018. URL `https://en.wikipedia.org/wiki/2008_Georgia_sugar_refinery_explosion`. [Online; accessed February 9, 2019].

[7] B Fletcher. The interaction of a shock with a dust deposit. *Journal of Physics D: Applied Physics*, 9(2):197, 1976.

[8] CC Hwang. Initial stages of the interaction of a shock wave with a dust deposit. *International journal of multiphase flow*, 12(4):655–666, 1986.

[9] Yi Luo, Deming Wang, and Jianwei Cheng. Effects of rock dusting in preventing and reducing intensity of coal mine explosions. *International Journal of Coal Science & Technology*, 4(2):102–109, 2017.

[10] CK Man and KA Teacoach. How does limestone rock dust prevent coal dust explosions in coal mines? *Mining Engineering*, 61(9):69, 2009.

[11] Heinrich M Jaeger, Sidney R Nagel, and Robert P Behringer. Granular solids, liquids, and gases. *Reviews of modern physics*, 68(4):1259, 1996.

[12] David L Henann and Ken Kamrin. A predictive, size-dependent continuum model for dense granular flows. *Proceedings of the National Academy of Sciences*, 110 (17):6730–6735, 2013.

[13] Bruno Andreotti, Yoël Forterre, and Olivier Pouliquen. *Granular media: between fluid and solid*. Cambridge University Press, 2013.

[14] Anthony Rosato, Katherine J Strandburg, Friedrich Prinz, and Robert H Swendsen. Why the brazil nuts are on top: Size segregation of particulate matter by shaking. *Physical Review Letters*, 58(10):1038, 1987.

[15] Igor Aranson and Lev Tsimring. *Granular patterns*. Oxford University Press, 2009.

[16] Jin Sun. Multiscale modeling of segregation in granular flows. 2007.

[17] Ansys Fluent. 12.0 theory guide. *Ansys Inc*, 5(5), 2009.

[18] Rahul Garg, Janine Galvin, Tingwen Li, and Sreekanth Pannala. Documentation of open-source mfix–dem software for gas–solids flows. *From URL https://mfix. netl. doe. gov/documentation/dem_doc_2012-1. pdf.(Accessed: 31 March 2014)*, 2010.

[19] Christopher J Greenshields. Openfoam user guide. *OpenFOAM Foundation Ltd, version*, 3(1), 2015.

[20] Peter A Cundall and Otto DL Strack. A discrete numerical model for granular assemblies. *geotechnique*, 29(1):47–65, 1979.

[21] A Lisjak and G Grasselli. A review of discrete modeling techniques for fracturing processes in discontinuous rock masses. *Journal of Rock Mechanics and Geotechnical Engineering*, 6(4):301–314, 2014.

[22] Paul W Cleary and Mark L Sawley. Dem modelling of industrial granular flows: 3d case studies and the effect of particle shape on hopper discharge. *Applied Mathematical Modelling*, 26(2):89–111, 2002.

[23] WK Hiromi Ariyaratne, EVPJ Manjula, Chandana Ratnayake, and Morten C Melaaen. Cfd approaches for modeling gas-solids multiphase flows–a review. In *Proceedings of The 9th EUROSIM Congress on Modelling and Simulation, EUROSIM 2016, The 57th SIMS Conference on Simulation and Modelling SIMS 2016*, number 142, pages 680–686. Linköping University Electronic Press, 2018.

[24] Madhava Syamlal, William Rogers, and Thomas J O?Brien. Mfix documentation: Theory guide. *National Energy Technology Laboratory, Department of Energy, Technical Note DOE/METC-95/1013 and NTIS/DE95000031*, 1993.

[25] JP Collins, RE Ferguson, K Chien, AL Kuhl, J Krispin, and HM Glaz. Simulation of shock-induced dusty gas flows using various models. In *AIAA, Fluid Dynamics Conference, 25 th, Colorado Springs, CO*, 1994.

[26] Wang Xiaofang, Jin Baosheng, Yuanquan Xiong, and Wenqi Zhong. Flow behaviors of gas-solid injector by 3d simulation with kinetic theory of granular flow. *Chinese Journal of Chemical Engineering*, 16(6):823–831, 2008.

[27] CKK Lun, S Br Savage, DJ Jeffrey, and N Chepurniy. Kinetic theories for granular flow: inelastic particles in couette flow and slightly inelastic particles in a general flowfield. *Journal of fluid mechanics*, 140:223–256, 1984.

[28] G Ahmadi and M Shahinpoor. Towards a turbulent modeling of rapid flow of granular materials. *Powder Technology*, 35(2):241–248, 1983.

[29] Paul C Johnson and Roy Jackson. Frictional–collisional constitutive relations for granular materials, with application to plane shearing. *Journal of Fluid Mechanics*, 176:67–93, 1987.

[30] Jianmin Ding and Dimitri Gidaspow. A bubbling fluidization model using kinetic theory of granular flow. *AIChE journal*, 36(4):523–538, 1990.

[31] Dimitri Gidaspow. *Multiphase flow and fluidization: continuum and kinetic theory descriptions*. Academic press, 1994.

[32] Vidar Mathiesen, Tron Solberg, and Bjørn H Hjertager. Predictions of gas/particle flow with an eulerian model including a realistic particle size distribution. *Powder Technology*, 112(1-2):34–45, 2000.

[33] Shuyue Lai, Ryan W Houim, and Elaine S Oran. Mechanism and structure of subsurface explosions in granular media. *Physical Review Fluids*, 2(9):094301, 2017.

[34] SB Savage and DJ Jeffrey. The stress tensor in a granular flow at high shear rates. *Journal of Fluid Mechanics*, 110:255–272, 1981.

[35] James T Jenkins and Stuart B Savage. A theory for the rapid flow of identical, smooth, nearly elastic, spherical particles. *Journal of fluid mechanics*, 130:187–202, 1983.

[36] JT Jenkins and F Mancini. Balance laws and constitutive relations for plane flows of a dense, binary mixture of smooth, nearly elastic, circular disks. *Journal of Applied Mechanics*, 54(1):27–34, 1987.

[37] D Gidaspow. Kinetic theory of multiphase flow and fluidization: validation and extension to binaries. In *Proceedings of the XIXth International Congress on Theory and Mechanics, Japan, 1996*, 1996.

[38] Eirik Manger. Modelling and simulation of gas/solids flow in curvilinear coordinates. 1998.

[39] Lu Huilin, Liu Wenti, Bie Rushan, Yang Lidan, and Dimitri Gidaspow. Kinetic theory of fluidized binary granular mixtures with unequal granular temperature. *Physica A: Statistical Mechanics and its Applications*, 284(1-4):265–276, 2000.

[40] Vidar Mathiesen, Tron Solberg, and BH Hjertager. An experimental and computational study of multiphase flow behavior in a circulating fluidized bed. *International Journal of Multiphase Flow*, 26(3):387–419, 2000.

[41] MR Baer and JW Nunziato. A two-phase mixture theory for the deflagration-to-detonation transition (ddt) in reactive granular materials. *International journal of multiphase flow*, 12(6):861–889, 1986.

[42] Annalisa Ambroso, Christophe Chalons, and P-A Raviart. A godunov-type method for the seven-equation model of compressible two-phase flow. *Computers & Fluids*, 54:67–91, 2012.

[43] Lu Huilin, He Yurong, and Dimitri Gidaspow. Hydrodynamic modelling of binary mixture in a gas bubbling fluidized bed using the kinetic theory of granular flow. *Chemical Engineering Science*, 58(7):1197–1205, 2003.

[44] S Benyahia, M Syamlal, and TJ O?Brien. Summary of mfix equations 2012-1. *From URL https://mfix. netl. doe. gov/documentation/MFIXEquations2012-1. pdf*, 2012.

[45] AB Yu and N Standish. Porosity calculations of multi-component mixtures of spherical particles. *Powder Technology*, 52(3):233–241, 1987.

[46] Y.H. Yu C.-Y. Wen. Mechanics of fluidization. *Chemical Engineering Progress Symposium Series*, 62:100–111, 1966.

[47] Sabri Ergun. Fluid flow through packed columns. *Chem. Eng. Prog.*, 48:89–94, 1952.

[48] DA Drew and RT Lahey. The virtual mass and lift force on a sphere in rotating and straining inviscid flow. *International Journal of Multiphase Flow*, 13(1):113–121, 1987.

[49] Mo Syamlal. The particle-particle drag term in a multiparticle model of fluidization. Technical report, EG and G Washington Analytical Services Center, Inc., Morgantown, WV (USA), 1987.

[50] Donald L Koch and Ashok S Sangani. Particle pressure and marginal stability limits for a homogeneous monodisperse gas-fluidized bed: kinetic theory and numerical simulations. *Journal of Fluid Mechanics*, 400:229–263, 1999.

[51] R Byron Bird. Transport phenomena. *Applied Mechanics Reviews*, 55(1):R1–R4, 2002.

[52] DJ Gunn. Transfer of heat or mass to particles in fixed and fluidised beds. *International Journal of Heat and Mass Transfer*, 21(4):467–476, 1978.

[53] Ryan W Houim and Kenneth K Kuo. A low-dissipation and time-accurate method for compressible multi-component flow with variable specific heat ratios. *Journal of Computational Physics*, 230(23):8527–8553, 2011.

[54] Marica Pelanti and Randall J LeVeque. High-resolution finite volume methods for dusty gas jets and plumes. *SIAM Journal on Scientific Computing*, 28(4): 1335–1360, 2006.

[55] Raymond J Spiteri and Steven J Ruuth. A new class of optimal high-order strong-stability-preserving time discretization methods. *SIAM Journal on Numerical Analysis*, 40(2):469–491, 2002.

[56] J Bell, A Almgren, V Beckner, M Day, M Lijewski, A Nonaka, and W Zhang. Boxlib user's guide. *github. com/BoxLib-Codes/BoxLib*, 2012.

[57] Peter MacNeice, Kevin M Olson, Clark Mobarry, Rosalinda De Fainchtein, and Charles Packer. Paramesh: A parallel adaptive mesh refinement community toolkit. *Computer physics communications*, 126(3):330–354, 2000.

[58] Bernd Einfeldt, Claus-Dieter Munz, Philip L Roe, and Björn Sjögreen. On godunov-type methods near low densities. *Journal of computational physics*, 92 (2):273–295, 1991.

[59] Meng-Sing Liou. A sequel to ausm, part ii: Ausm+-up for all speeds. *Journal of computational physics*, 214(1):137–170, 2006.

[60] Marsha J Berger and Phillip Colella. Local adaptive mesh refinement for shock hydrodynamics. *Journal of computational Physics*, 82(1):64–84, 1989.

[61] Marsha J Berger and Joseph Oliger. Adaptive mesh refinement for hyperbolic partial differential equations. *Journal of computational Physics*, 53(3):484–512, 1984.

[62] MJ Berger and R LeVeque. Adaptive mesh refinement for two-dimensional hyperbolic systems and the amrclaw software. *SIAM J. Numer. Anal*, 35:2298–2316, 1998.

[63] S Kohn. Samrai: Structured adaptive mesh refinement applications infrastructure. *Technical report*, 1999.

[64] Alan R Pinkus and Vincent M Parisi. Helicopter brown-out landing, January 5 2010. US Patent 7,642,929.

[65] Christopher John Cawthorn. *Several applications of a model for dense granular flows*. PhD thesis, University of Cambridge, 2011.

[66] JH Gerrard. An experimental investigation of the initial stages of the dispersion of dust by shock waves. *British Journal of Applied Physics*, 14(4):186, 1963.

[67] AA Borisov, AV Lyubimov, SM Kogarko, and VP Kozenko. Instability of the surface of a granular medium behind sliding shock and detonation waves. *Combustion, Explosion and Shock Waves*, 3(1):95–97, 1967.

[68] RW Houim, OJ Ugarte, S Lai, and ES Oran. Mechanisms of dust scouring behind shock waves. In *Proceedings of the 11th International Symposium on Hazards, Prevention, and Mitigation of Industrial Explosions*, pages 188–202, 2016.

[69] OJ Ugarte, RW Houim, and ES Oran. Examination of the forces controlling dust dispersion by shock waves. *Physical Review Fluids*, 2(7):074304, 2017.

[70] T Suzuki and T Adachi. The effects of particle size on shock wave-dust deposit interaction. In *14th Space Technology and Science Symposium*, pages 483–490, 1984.

[71] Amira Chowdhury, H Greg Johnston, Chad V Mashuga, M Sam Mannan, and Eric L Petersen. Effect of particle size and polydispersity on dust entrainment behind a moving shock wave. *Experimental Thermal and Fluid Science*, 93:1–10, 2018.

[72] CJ Zhu, BQ Lin, BY Jiang, Qian Liu, and Yi-Du Hong. Dust lifting behind a shock wave: Analysis based on the ee method. *Journal of China University of Mining & Technology*, 5:008, 2012.

[73] Wang Boyi, Xiong Yi, Chen Qian, and AN Osiptsov. Dust-cloud structures behind a shock wave moving over a deposited layer of fine particles. *Progress in Natural Science*, 15(11):972–981, 2005.

[74] Amira Yousuf Chowdhury. *Shock interaction with dust layers*. PhD thesis, 2015.

[75] Beckman Coulter. Ls 13 320 laser diffraction particle size analyzer: Instructions for use. *URI: https://www. beckmancoulter. com/wsrportal/techdocs*, 2011.

[76] Amira Y Chowdhury, H Greg Johnston, Brandon Marks, M Sam Mannan, and Eric L Petersen. Effect of shock strength on dust entrainment behind a moving shock wave. *Journal of Loss Prevention in the Process Industries*, 36:203–213, 2015.

[77] Eivind Helland, René Occelli, and Lounes Tadrist. Numerical study of cluster formation in a gas–particle circulating fluidized bed. *Powder Technology*, 110(3): 210–221, 2000.

[78] Olivier Desjardins, Rodney O Fox, and Philippe Villedieu. A quadrature-based moment method for dilute fluid-particle flows. *Journal of Computational Physics*, 227(4):2514–2539, 2008.

[79] JL Lebowitz. Exact solution of generalized percus-yevick equation for a mixture of hard spheres. *Physical Review*, 133(4A):A895, 1964.

[80] Norman F Carnahan and Kenneth E Starling. Equation of state for nonattracting rigid spheres. *The Journal of Chemical Physics*, 51(2):635–636, 1969.

[81] Hadjira Iddir and Hamid Arastoopour. Modeling of multitype particle flow using the kinetic theory approach. *AIChE Journal*, 51(6):1620–1632, 2005.

[82] JH Koo and KK Kuo. Transient combustion in granular propellant beds. part i. theoretical modeling and numerical solution of transient combustion processes in mobile granular propellant beds. Technical report, PENNSYLVANIA STATE UNIV UNIVERSITY PARK DEPT OF MECHANICAL ENGINEERING, 1977.

[83] NC Markatos and D Kirkcaldy. Analysis and computation of three-dimensional, transient flow and combustion through granulated propellants. *International Journal of Heat and Mass Transfer*, 26(7):1037–1053, 1983.

[84] Julien Nussbaum, Philippe Helluy, Jean-Marc Hérard, and Alain Carriere. Numerical simulations of gas-particle flows with combustion. *Flow, turbulence and combustion*, 76(4):403–417, 2006.

[85] Jin Sun and Francine Battaglia. Hydrodynamic modeling of particle rotation for segregation in bubbling gas-fluidized beds. *Chemical Engineering Science*, 61(5): 1470–1479, 2006.

[86] Scott Cooper and Charles J Coronella. Cfd simulations of particle mixing in a binary fluidized bed. *Powder Technology*, 151(1-3):27–36, 2005.

[87] Dinesh Gera, Madhava Syamlal, and Thomas J O'Brien. Hydrodynamics of particle segregation in fluidized beds. *International Journal of Multiphase Flow*, 30 (4):419–428, 2004.

[88] Michael J Sapko, Eric S Weiss, and Richard W Watson. Explosibility of float coal dust distributed over a coal-rock dust substratum. In *Proceedings of the 22 nd International Conference of Safety in Mines Research Institutes*, volume 20, 1987.

[89] Karen Meech, Michael F A'Hearn, Lucy McFadden, Michael JS Belton, Alan Delamere, Jochen Kissel, Ken Klassen, Don Yeomans, Jay Melosh, Pete Schultz, Jessica Sunshine, and Joseph Veverka. Deep impact-exploring the interior of a comet. In *Bioastronomy 99: A New Era in the Search for Life*, volume 213, pages 235–242, 2000.

[90] James E Richardson, H Jay Melosh, Carey M Lisse, and Brian Carcich. A ballistics analysis of the deep impact ejecta plume: Determining comet tempel 1's gravity, mass, and density. *Icarus*, 191(2):176–209, 2007.

[91] Michael F A'Hearn, MJS Belton, WA Delamere, J Kissel, KP Klaasen, LA McFadden, KJ Meech, HJ Melosh, PH Schultz, JM Sunshine, et al. Deep impact: excavating comet tempel 1. *science*, 310(5746):258–264, 2005.

[92] Jens Biele, Stephan Ulamec, Michael Maibaum, Reinhard Roll, Lars Witte, Eric Jurado, Pablo Muñoz, Walter Arnold, Hans-Ulrich Auster, Carlos Casas, et al. The landing (s) of philae and inferences about comet surface mechanical properties. *Science*, 349(6247):aaa9816, 2015.

[93] Eric Chaisson and Stephen McMillan. *Astronomy today*. Prentice Hall Upper Saddle River, NJ, 2002.

[94] Roland Meier and Tobias C Owen. Cometary deuterium. *Space science reviews*, 90(1-2):33–43, 1999.

[95] Tobias Owen and Akiva Bar-Nun. Comets, impacts, and atmospheres. *Icarus*, 116 (2):215–226, 1995.

[96] M Pätzold, T Andert, M Hahn, SW Asmar, J-P Barriot, MK Bird, B Häusler, K Peter, S Tellmann, E Grün, et al. A homogeneous nucleus for comet 67p/churyumov–gerasimenko from its gravity field. *Nature*, 530(7588):63–65, 2016.

[97] Anita L Cochran, Anny-Chantal Levasseur-Regourd, Martin Cordiner, Edith Hadamcik, Jérémie Lasue, Adeline Gicquel, David G Schleicher, Steven B Charnley, Michael J Mumma, Lucas Paganini, et al. The composition of comets. *Space Science Reviews*, 197(1-4):9–46, 2015.

[98] Bernard Marty, Guillaume Avice, Yuji Sano, Kathrin Altwegg, Hans Balsiger, Myrtha Hässig, Alessandro Morbidelli, Olivier Mousis, and Martin Rubin. Origins of volatile elements (h, c, n, noble gases) on earth and mars in light of recent results from the rosetta cometary mission. *Earth and Planetary Science Letters*, 441:91–102, 2016.

[99] I Toth and CM Lisse. On the rotational breakup of cometary nuclei and centaurs. *Icarus*, 181(1):162–177, 2006.

[100] Clément Feller, Sonia Fornasier, Pedro Henrique Hasselmann, Maria Antonieta Barucci, Frank Preusker, Frank Scholten, Laurent Jorda, Nicolas Thomas, Antoine Pommerol, Bernhard Jost, et al. Osiris'decimeter observations of comet 67p/churyumov-gerasimenko. In *AAS/Division for Planetary Sciences Meeting Abstracts*, volume 48, 2016.

[101] Mark S Bentley, Roland Schmied, Thurid Mannel, Klaus Torkar, Harald Jeszenszky, Jens Romstedt, Anny-Chantal Levasseur-Regourd, Iris Weber, Elmar K

Jessberger, Pascale Ehrenfreund, et al. Aggregate dust particles at comet 67p/churyumov–gerasimenko. *Nature*, 537(7618):73–75, 2016.

[102] Harry L Swinney and EC Rericha. Pattern formation and shocks in granular gases. *arXiv preprint cond-mat/0408252*, 2004.

[103] Victor Golub and Olga Mirova. Shock waves in granular media. In *Shock Wave Science and Technology Reference Library*, pages 325–351. Springer, 2007.

[104] Alexander Goldshtein, Alexander Alexeev, and Michael Shapiro. Shock waves in granular gases. In *Granular Gas Dynamics*, pages 187–225. Springer, 2003.

[105] V Kamenetsky, A Goldshtein, M Shapiro, and D Degani. Evolution of a shock wave in a granular gas. *Physics of Fluids*, 12(11):3036–3049, 2000.

[106] A Goldshtein, M Shapiro, and C Gutfinger. Mechanics of collisional motion of granular materials. part 3. self-similar shock wave propagation. *Journal of Fluid Mechanics*, 316:29–51, 1996.

[107] AV Fedorov et al. Modeling of propagation of shock and detonation waves in dusty media with allowance for particle collisions. *Combustion, Explosion, and Shock Waves*, 50(5):547–555, 2014.

[108] Edward Teller, Wilson K. Talley, Gary H. Higgins, and Gerald W. Johnson. Constructive uses of nuclear explosives. 1968.

[109] Geoffrey Taylor. The formation of a blast wave by a very intense explosion. I. Theoretical discussion. *Proceedings of the Royal Society of London. Series A, Mathematical and Physical Sciences*, 201(1065):159–174, 1950.

[110] F Zhang, DL Frost, PA Thibault, and SB Murray. Explosive dispersal of solid particles. *Shock Waves*, 10(6):431–443, 2001.